UR-895
ER1 3065-398
October 1984

A Search for Neutrino Oscillations

with Large Values of Delta-m-Squared

by

Ian E. Stockdale

Submitted in Partial Fulfillment

of the

Requirements for the Degree

Doctor of Philosophy

Supervised by Arie Bodek
Department of Physics and Astronomy
College of Arts and Sciences

University of Rochester

Rochester, New York

1984

Curriculum Vitae

Ian E. Stockdale was born in Ottawa, Ontario, Canada. He graduated from Ann Arbor Huron High School in June 1975. He graduated from the University of Michigan in December 1979 with the degrees Bachelor of Science in Physics (College of Literature, Science and the Arts) and Bachelor of Science in Engineering (Nuclear Engineering; College of Engineering). Since then, he has been a graduate student at the University of Rochester, where he received the degree Master of Arts in Physics in February 1982.

Acknowledgements

The successful completion of any particle physics experiment is the result of the efforts of many people. I am grateful to the other members of the CCFR collaboration (listed in Appendix B). The hard work of each person enabled us to construct, run, and analyse the experiment rapidly and effectively.

I have been especially fortunate in have Arie Bodek as an advisor. He has been at once hardworking, enthusiastic, and insightful. It has been a real pleasure to be associated with him. I would also like to thank my fellow graduate students - Carl Haber, Karol Lang, Patrick Reutens, Priscilla Auchincloss, Martin Ruiz, David Garfinkle, and Katie Freese - for the privilege of working with them.

Particular credit should be given to those members of the collaboration, aside from the students, who contributed to the data analysis; they were David Levinthal, Frank Merritt, Mark Oreglia, Mike Shaevitz, and Wesley Smith. Each of them worked very hard and deserves recognition for it. Fred Borcherding, Rick Coleman, Stephen Pordes, Petros

Rapidis, and Herman White played major roles in the beam monitor instrumentation and analysis (the perennial bane of neutrino physics).

It is for particle physics graduate students to leave the warmth and comfort of the universities and spend years on the Illinois prairie. Those years have been made more bearable for me by the emergence of an active musical group at Fermilab, largely due to Dick Gustafson. Tokio Ohska, Herman White, and Carol Wilkinson. The cooking of Tita Jensen, and the good company enjoyed at her restaurant have been an inspiration for me to survive the most difficult of weeks.

Finally, I would like to acknowledge the support of my parents and family throughout my entire academic career. They have always been supportive and encouraging, and I am very thankful.

Abstract

A search for inclusive muon-neutrino (ν_μ) and muon-antineutrino ($\bar{\nu}_\mu$) oscillations has been performed in the Fermilab narrow band neutrino beam using two detectors running simultanously at two distances from the neutrino source. The data show no evidence for either neutrino or antineutrino oscillations and rule out oscillations of ν_μ or $\bar{\nu}_\mu$ into any other single type of neutrino for $15 < \Delta m^2 < 1000\ eV^2/c^4$ and $\sin^2(2\theta) > 0.02 - 0.40$.

Table of Contents

	page
Chapter I: Neutrino Mass: Theory and Experiment	1
I.1: Introduction to Neutrino Masses	3
I.2: Neutrino Mass Measurements	7
I.2.1: Tritium β Decay	7
I.2.2: Muon Decay at Rest	10
I.2.3: Tau Decay at e^+e^- Colliders	11
I.2.4: Searches for Neutrino-less Double Beta Decay	12
I.2.5: Searches for Neutrino Oscillations	15
I.3: Cosmology and Astrophysics	16
Chapter II: Neutrino Oscillations	24
II.1: Formalism	24
II.2: Exclusive Searches	32
II.3: Inclusive Searches	35
Chapter III: Experimental Apparatus	44
III.1: The Neutrino Detectors	44
III.1.1: The Wonder Bldg. Detector	45
III.1.1.a: Trigger Counters	49
III.1.1.b: Calorimetry Counters	64
III.1.1.c: CAMAC Modules	70
III.1.1.d: Event Triggers	76
III.1.1.e: Spark Chambers	79
III.1.1.f: Toroidal Magnets	81
III.1.1.g: On-line Software	81
III.1.2: The Lab E Detector	84
III.2.1: The Neutrino Beam	91
III.2.2: The Beam Simulations	101
Chapter IV: Event Reconstruction	112
IV.1: Determination of Muon Momentum	112
IV.1.1: Wonder Bldg.	113
IV.1.2: Lab E	122
IV.2: Determination of Hadron Energy	125
IV.2.1: Wonder Bldg.	125
IV.2.2: Lab E	139

Chapter V: The Oscillation Analysis 145
V.1: Merging 145
V.2: Good Running Requirements 147
V.3: Event Selection 150
V.3.1: Quality of Data Cuts 151
V.3.2: Projection Cuts 164
V.4: Reconstruction In-efficiency Correction 170
V.5: Monte Carlo Event Simulation 172
V.6: Energy Binning 174
V.7: Calculation of Event Ratios 182

Chapter VI: Results and Conclusions 203
VI.1: Calculation of the Limit 206
VI.1.1: Calculation of χ^2 206
VI.1.2: Likelihood Ratio Test 211
VI.1.3: Pearson's χ^2 Test 226
VI.2: Summary of Neutrino Oscillation Measurements 228

References 235

Appendix A: Momentum Reconstruction Formulae 240

Appendix B: CCFR Collaboration 245

List of Tables

page

Table I.1: Mass-to-Light ratios of astrophysical objects 19

Table II.1: Sensitivities of 2 inclusive searches 41

Table III.1: Types of scintillators used 50

Table III.2: Map of superlow ADCs 73

Table III.3: Comparison of Lab E and Wonder Bldg. detectors 90

Table III.4: Total protons delivered to the experiment during good running 92

Table III.5: Total live protons delivered after the quality of monitor cuts 92

Table IV.1: Guide to the ADCs 133

Table IV.2: Wonder Bldg. E_{had} calibration 137

Table V.1: Event totals after monitor record cuts 149

Table V.2: Events cut by individual cuts 167

Table V.3: Event totals after successive cuts 168

Table V.4: Summary of Wonder Bldg. scanning 171

Table V.5: Parameters for ν_π/ν_k separatrix 176

Table V.6: Event totals in energy bins (data and MC) 184

Table V.7: Detector livetimes 185

Table V.8: Veto-deadtimes 187

Table V.9: Event Ratios (corrected for normalization) 188

Table V.10: Mean meson decay angles 195

Table V.11: Event ratios divided by MC event ratios 197

Table V.12: Values of χ^2 (no oscillations) 201

Table VI.1: Values of χ^2_{min} 207

Table VI.2: Values of $\Delta\chi^2_c$ (ν data) 219

Table VI.3: Values of $\Delta\chi^2_c$ ($\bar{\nu}$ data) 220

Table VI.4: Values of $\Delta\chi^2_c$ ($\nu+\bar{\nu}$ data) 221

List of Figures

page

Figure I.1: Tritium beta decay spectrum 8

Figure I.2: Neutrinoless double β-decay diagram 13

Figure I.3: Rotation curves of spiral galaxies 17

Figure II.1: Ratio of ν fluxes in a 2 detector oscillation search 37

Figure II.2: Inclusive oscillation sensitivity vs. L/E 39

Figure III.1: Wonder Bldg. detector 46

Figure III.2: Wonder Bldg. calorimeter module 47

Figure III.3: Wonder Bldg. spectrometer 48

Figure III.4: Wonder Bldg. counters Veto and T1 51

Figure III.5: Plan views of WB Veto and Trigger Counters 52

Figure III.6: Wave-shifter bar readout 55

Figure III.7: Wonder Bldg. trigger counter logic 57

Figure III.8: Wonder Bldg. calorimetry counter 63

Figure III.9: Wonder Bldg. calorimetry counter map 65

Figure III.10: Wonder Bldg. Calorimetry counter logic 68

Figure III.11: Wonder Bldg. Trigger logic 74

Figure III.12: Lab E detector (side view) 85

Figure III.13: Lab E detector (expanded view) 86

Figure III.14: Lab E muon trigger 88

Figure III.15: N0 dichromatic train 94

Figure III.16: Layout of FNAL neutrino area 95

Figure III.17: Sample SWIC profiles 98

Figure III.18: Sample ν beam steering plots 100

Figure III.19: Predicted SWIC profiles (TURTLE) 104

Figure III.20: Beam angular distributions (from hole collimator) 105

Figure III.21: Predicted angular distributions (TURTLE) 106

Figure III.22: Predicted SWIC profiles (Ad Hoc) 108

Figure III.23: Predicted angular distributions (Ad Hoc) 109

Figure III.24: Predicted E vs. R at Lab E (TURTLE) 111

Figure IV.1: Wonder Bldg. p_μ distributions 121

Figure IV.2: Lab E p_μ distributions 124

Figure IV.3: ADC non-linearity 128

Figure IV.4: Short term counter gain drift 130

Figure IV.5: Long term counter gain drift 131

Figure IV.6: Wonder Bldg. muon peak 135

Figure IV.7: Wonder Bldg. E_{had} distributions 138

Figure IV.8: Lab E calorimetry counter map 143

Figure IV.9: Lab E E_{had} distributions 144

Figure V.1: Longitudinal vertex distributions 152

Figure V.2: Effect of longitudinal shower containment 154

Figure V.3: Transverse vertex distributions 157

Figure V.4: Event radius distributions (ν_π) 158

Figure V.5: Event radius distributions (ν_k) 159

Figure V.6: Muon trajectory cut illustration 161

Figure V.7: θ_μ distributions 163

Figure V.8: Illustration of projection cuts 169

Figure V.9: Lab E E_ν vs. r_ν (data) scatter plots 177

Figure V.10: Wonder Bldg. E_ν vs. r_ν (data) scatter plots 178

Figure V.11: Relative energy calibration (ν data) 180

Figure V.12: Relative energy calibration ($\bar{\nu}$ data) 181

Figure V.13: ν event ratios after normalization 190
correction 190

Figure V.14: $\bar{\nu}$ event ratios after normalization 191
correction 191

Figure V.15: ν event ratios (Monte Carlo) 192

Figure V.16: $\bar{\nu}$ event ratios (Monte Carlo) 193

Figure V.17: ν event ratios divided by MC event ratios 198

Figure V.18: $\bar{\nu}$ event ratios divided by MC event ratios 199

Figure V.19: ($\nu+\bar{\nu}$) Monte Carlo event ratios and data event ratios divided by MC ratios 200

Figure VI.1: ν event ratios (corrected for normalization) with χ^2_{min} solution superimposed 208

Figure VI.2: $\bar{\nu}$ event ratios (corrected for normalization) with χ^2_{min} solution superimposed 209

Figure VI.3: ($\nu+\bar{\nu}$) event ratios (corrected for normalization) with χ^2_{min} solution superimposed 210

Figure VI.4: ν Likelihood Ratio test Monte Carlo histograms 216

Figure VI.5: $\bar{\nu}$ Likelihood Ratio test Monte Carlo histograms 217

Figure VI.6: $(\nu+\bar{\nu})$ Likelihood Ratio test Monte Carlo histograms 218

Figure VI.7: Inclusive ν oscillation limits (CCFR) 223

Figure VI.8: Inclusive $\bar{\nu}$ oscillation limits (CCFR) 224

Figure VI.9: Inclusive $(\nu+\bar{\nu})$ oscillation limits (CCFR) 225

Figure VI.10: Inclusive ν_μ oscillation limits 239

Figure VI.11: Inclusive $\bar{\nu}_e$ oscillation limits (Gosgen) 231

Figure VI.12: Inclusive $\bar{\nu}_e$ oscillation limits (Bugey) 232

Figure VI.13: Exclusive ν_μ oscillation limits 233

CHAPTER I

Neutrino Mass: Theory and Experiment

The question of whether the neutrino (ν) has a mass has been an open one ever since the neutrino was predicted. Many experiments have been performed attempting to measure m_ν, and (until recently) all have obtained null results. This thesis describes a recent attempt to probe this problem via an indirect route - a search for neutrino oscillations. The organization is as follows.

Chapter I gives an account of the theoretical ideas concerning massive neutrinos, treating both the concepts and

the formalism. Therein may also be found a brief summary of the current data on m_ν both from direct searches (Section 2) and from astrophysical observations and calculations (Section 3). Chapter II describes the mathematics and phenomenology of ν oscillations. The particular ν oscillation search which is the subject of this dissertation is described in Chapters III (detectors and ν beam), IV (event reconstruction), V (event selection), and VI (physics analysis). Chapter VI also contains a summary of the world's current limits on ν oscillations.

Section I.1: Introduction to Neutrino Masses

Theoretical physicists have been working on the subject of ν masses and oscillations for many years. Two reviews of the subject, by Bilenky and Pontecorvo[1] (who first suggested the existence of ν oscillations), and by Frampton and Vogel[2] have been published. The discussion here and in Chapter II is based on these works, as well as the recent papers of Kayser[3] and Rosen[4].

Neutrino masses, should they exist, may fall into one (or both) of two classes. These are called Majorana and Dirac masses. The "conventional" particles, such as quarks and charged leptons, are Dirac particles which are described by a four component Dirac spinor (2 components each for the particle and the anti-particle). The anti-particle of a Dirac ν, obtained by applying CPT to the ν state, is not identical to the original ν. There are thus four independent components to the Dirac spinor.

In the Majorana case, the application of CPT to the ν yields the original state (up to a phase factor). This leaves only 2 independent elements in the spinor. It is instructive to consider a physical example of the difference between Majorana and Dirac neutrinos (this example may be found in its original form in Ref. 3).

Consider a ν_μ produced in the decay: $\pi^+ \to \mu^+ + \nu_\mu$. The ν_μ is a left-handed particle (having been emitted in a V-A process). If the ν_μ is massive, then it may be Lorentz boosted into a reference frame where it is right-handed. If the ν were a Dirac particle, then it would be sterile under the V-A interaction. If the ν_μ is a Majorana particle, then the right-handed ν_μ is the same as the right-handed $\bar{\nu}_\mu$. The charged current reaction: $\bar{\nu}_\mu + q \to \mu^+ + X$ could then occur.

Turning now to the mathematics, the masses of Majorana and Dirac neutrinos are generated by different types of mass terms. The mass term for a Dirac particle is given by:[4]

$$L_D = -\frac{1}{2}\bar{\nu} m_D \nu = -\frac{1}{4}(\bar{\nu} m_D \nu + \bar{\nu}_c m_D \nu_c) \qquad (1)$$

Here, ν is the neutrino spinor, $\bar{\nu}$ is the adjoint field, and $\bar{\nu}_c$ is the CPT conjugate (the anti-particle spinor). The Majorana mass term couples the neutrino with its anti-particle:[4]

$$L_M = -\frac{1}{4}(\bar{\nu} m_M \nu_c + \bar{\nu}_c m_M \nu) \qquad (2)$$

Using these mass terms, we may construct an equation of the form:[4]

$$L_{mass} = (\bar{\nu}^R, \bar{\nu}_c^R, \bar{\nu}^L, \bar{\nu}_c^L) \begin{pmatrix} 0 & M \\ M^+ & 0 \end{pmatrix} \begin{pmatrix} \nu^R \\ \nu_c^R \\ \nu^L \\ \nu_c^L \end{pmatrix} \qquad (3)$$

where, $\nu^R = (1 + \gamma_5)\,\nu$, and $\nu^L = (1 - \gamma_5)\,\nu$, etc. The 2 x 2 mass sub-matrix is given by:[4]

$$M = \begin{pmatrix} m_{RL} & m_{R,CL} \\ m_{CR,L} & m_{RL} \end{pmatrix} \qquad (4)$$

The co-efficient, m_{RL}, denotes the Dirac mass terms, and the remaining two co-efficients give the Majorana mass terms. This matrix may now be diagonalized to yield the mass eigenstates and their eigenvalues.

There have been many suggestions as to how the above ν mass terms may occur.[5] Majorana mass terms are predicted in left-right symmetric models.[6] In those models, there are 2 massive neutrinos for each generation, one of which is light and another which is heavy. These masses are related to the mass of the as yet unobserved right-handed weak vector boson (W_R). A similar combination of very heavy and very light

Majorana neutrinos may be obtained in the O(10) Grand Unified Theory (GUT) model.[7] Massive neutrinos may also be obtained in the SU(5) and SO(10) models.[8]

Section I.2: Neutrino Mass Measurements

Many experiments attempting to measure the mass of one of the three known or inferred neutrinos have been performed. Four such experiments shall be summarized in this section. They are (i) the measurement of the tritium β decay spectrum[9,10]; (ii) the measurement of the muon momentum in π decay at rest[11]; (iii) the study of invariant mass distributions in τ decay[12,13]; and (iv) the search for neutrino-less double beta decay.[14,15] No attempt will be made to discuss searches for extra peaks in decays into neutrinos (attributable to non-zero ν masses and mixings)[16,17], measurements of electron capture in nuclei,[18,19] or other techniques.

Section I.2.1: Tritium β Decay

The most precise attempts to obtain the mass of the electron anti-neutrino ($\bar{\nu}_e$), and thus that of ν_e (assuming CPT conservation), have been measurements of the β decay spectrum in tritium. The energy spectrum of electrons resulting from β decay is given by:[20]

$$N(E) = \text{constant} \times F(Z,E)\, p_e\, E \times \sum_i W_i\left(\left((\Delta_i - E)^2 - m_\nu^2\right)^{1/2}(\Delta_i - e)\right) \qquad (4)$$

where F(Z,E) takes account of nuclear effects, Z is the atomic number, E is the electron energy, p is the momentum of the electron, Δ_i is the endpoint of the spectrum, and e is the electric charge.

Figure I.1: Kurie plot (cf. p. 9) for β decay of tritium.

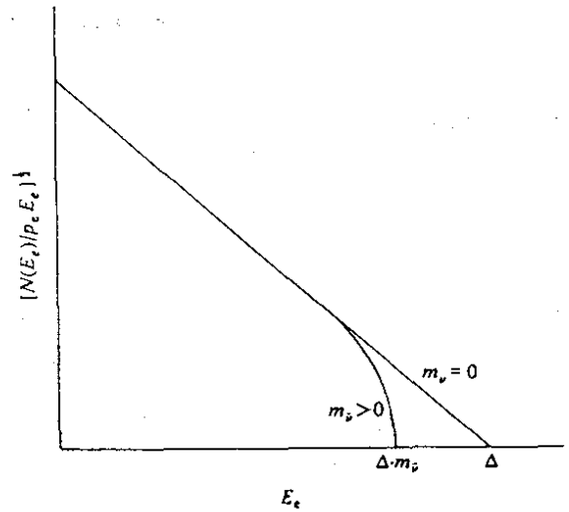

The behaviour of $\left(\frac{N(e)}{p_e E}\right)^{1/2}$ (the "Kurie plot") is shown in Fig. I.1 for the case in which the sum over final states of the decay process, i, is elliminated. The presence of a non-zero ν mass changes the function from a straight line to a curve which turns down before the endpoint. The goal of the β decay experiments is to accurately measure the Kurie plot near the end-point (Δ) and thus extract m_ν.

The largest sources of error in this measurement are: (i) the very low event rate near the end-point; (ii) the complicated calculation needed to take the presence of excited states of the final state molecule into account; and (iii) the possibility that several mass eigenstates mix and give several different superimposed end-points. The second point is particularly important for experiments (such as the ITEP measurements of Ref. 9) which use tritium embedded in complicated molecules (e.g. valine - $C_5H_{11}NO_2$). A detailed discussion of Tritium end-point measurements is given in Ref. 10.

The most recent β decay measurement,[9] carried out by a group at ITEP in Moscow, has found a value for $m(\bar{\nu}_e)$ of 33.0 ± 1.1 eV/c^2. This measurement uses an electro-magnetic spectrometer to obtain a precise measurement of the electron energy. The most serious systematic difficulty is the calculation of the effect of the valine-tritium molecule on

the Kurie plot. However, the experimenters believe that this problem does not weaken the result. For example, if the valine is neglected, a mass of 27.3 ± 1.2 eV/c^2 is obtained; indicating that a vastly over-simplified calculation does not cause a large deviation from the "correct" treatment. This calculation is discussed further in Ref. 21.

It should be stressed that the ITEP experiment has the only non-zero measurement for the mass of any neutrino. Other experiments are in progress[22] to verify this result. These experiments are expected to be sensitive to a mass of 5 eV/c^2, so that a clarification of this subject might be expected soon.

Section I.2.2: Muon Decay at Rest

A recent experiment at SIN in Villigen, Switzerland has produced the lowest upper bound on the ν_μ mass. The SIN group[11] used π^+ mesons from a high intensity source in measurments of the momentum of the μ^+ produced in two body decays at rest. The principle improvements resulting in the new results were an increase in statistics by a factor of five, and a more precise determination of the magnetic field used to momentum analyse the decay muon.

The experiment measured p_μ = (29.79139 ± .00077) MeV/c). This number was used together with the best measurements of the μ^- mass ((105.65932 ± .00029) MeV/c^2) and the π^- mass ((139.56761 ± .00077) MeV/c^2) to obtain:

$$(m(\nu_\mu))^2 = (-0.163 \pm .080)\ \mathrm{MeV}^2/c^4 \qquad (5)$$

This yields an upper limit of: $m(\nu_\mu) < 0.25$ MeV/c^2 (90 % C.L.). It is interesting to note that the error on m_π makes as large a contribution to the error in (5) as does the measurement error on p_μ. The result of the SIN group is a factor of two lower than the previous upper limit on $m(\nu_\mu)$, which was obtained by measuring π decay in flight.[23]

Section I.2.3: Tau Decay at e^+e^- Colliders

The third charged sequential lepton, τ, has only been observed at high energy e^+e^- colliding beam storage rings. A review of its properties may be found in Ref. 24. Two measurements done using the Mark II[12] and DELCO[13] detectors at PEP have produced the best available limits on the mass of the ν_τ. The Mark II measurement will be described below; the DELCO collaboration uses a somewhat different technique to obtain a similar number.

The analysis used by the Mark II selected events with one charged particle recoiling against three charged particles, this being a clean signature of $\tau^+\tau^-$ production. The presence of a π^0 in the same hemisphere as the 3 charged tracks was also required. The distribution of the invariant mass of the 3 charged and 1 neutral particle was compared to that predicted by hypotheses assuming different values of $m(\nu_\tau)$. An upper limit for $m(\nu_\tau)$ of 164 MeV/c^2 (90 % C.L.) was found.

Section I.2.4: Searches for Neutrino-less Double Beta Decay

The three sections above have described attempts to directly measure the mass of the neutrino, irregardless of whether the neutrino is a Dirac or Majorana particle. Searches for neutrino-less double beta (0ν-2β) decay probe the question of whether neutrinos have a Majorana mass.

Figure I.2: Feynman diagram for neutrino-less double beta decay ($0\nu-2\beta$).

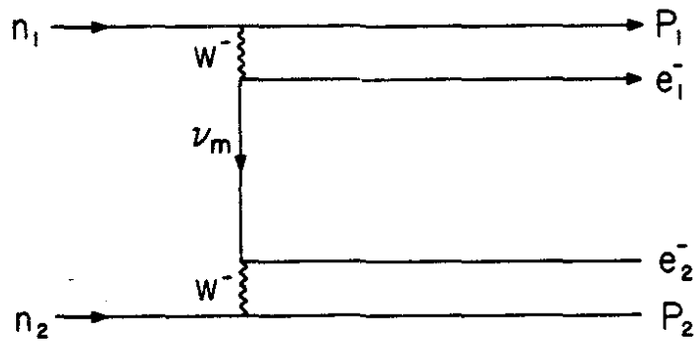

The diagram for $0\nu-2\beta$ decay is shown in Fig. I.2. The reaction may proceed only if the neutrino is a Majorana particle. This is because it must appear to be a neutrino when it is emitted, and to be an anti-neutrino when it is absorbed. In addition, it is necessary either that the ν be massive or that there exist right-handed currents. This process is further discussed in Ref. 25.

In the absence of CP effects, the amplitude for $0\nu-2\beta$ decay is given by:

$$A(0\nu-2\beta) \propto \sum_m U_{em}^2 M_m \qquad (6)$$

where U_{em} is the element of the neutrino mixing matrix linking the weak eigenstate ν_e to the mass eigenstate ν_m. The mass of ν_m is given by M_m. Several experiments[14,15] have reported limits on m_ν based on the non-observation of $0\nu-2\beta$ decay. The most restrictive of these is $m_\nu < 5.6$ eV/c^2 (95 % C.L.) from measurements in 10^9 year old Te ore.

Unfortunately, recent calculations indicate that these limits may not be taken to be absolute. It has been shown that interference between the amplitudes of different mass eigenstates, m, may result in the complete suppression of the overall $0\nu-2\beta$ rate. This may occur if CP is violated.[25] If different mass eigenstates have opposite CP phases, it may occur even when CP is conserved.[26,27] In these cases,

the limits can only be applied to an "effective" neutrino mass, which may be several orders of magnitude smaller than that of the least massive eigenstate.

Section I.2.5: Searches for Neutrino Oscillations

Neutrino oscillation searches are motivated in part by the difficulties of the measurements described above. If there are non-zero ν masses and mixings, then ν oscillation searches may observe large signals when more direct experiments see no effect. This topic is examined in detail in Chapter II, and a summary of the general experimental situation is given in Chapter VII. The details of a particular ν oscillation search comprise most of this thesis.

Section I.3: Cosmology and Astrophysics

The relationship between the mass of the neutrino and astrophysics has been a matter of great interest during the past several years. Many authors have reported on the constraints which cosmological measurements place on neutrino masses, and conversely, the implications a non-zero value of m_ν would have for astrophysics and cosmology.[28,29,30,31] Below are reviewed two topics pertaining to this subject: the dark matter which has been inferred to exist in galaxies and the limits on m_ν determined by calculations of the density of the universe.

One set of observations which has led to speculation concerning massive neutrinos is the data on galactic rotation curves. By observing spiral galaxies edge-on and measuring the blue- and red-shifts of spectral lines in stars versus their distance from the galactic centre, it is possible to extract the rotational velocity of objects in that galaxy as a function of radius.[32] This radial dependence is known as the "rotation curve". For a large number of galaxies, the rotation curve has been observed to be flat from distances as small as 10-20 kpc (1 kpc = 3×10^{16} km) to the edge of the visible matter in the galaxy (about 100 kpc). Several rotation curves are shown in Fig. I.3.[32]

Figure I.3: Rotation curves from spiral galaxies (Ref.32); illustrating the evidence for "dark" matter in astrophysical objects.

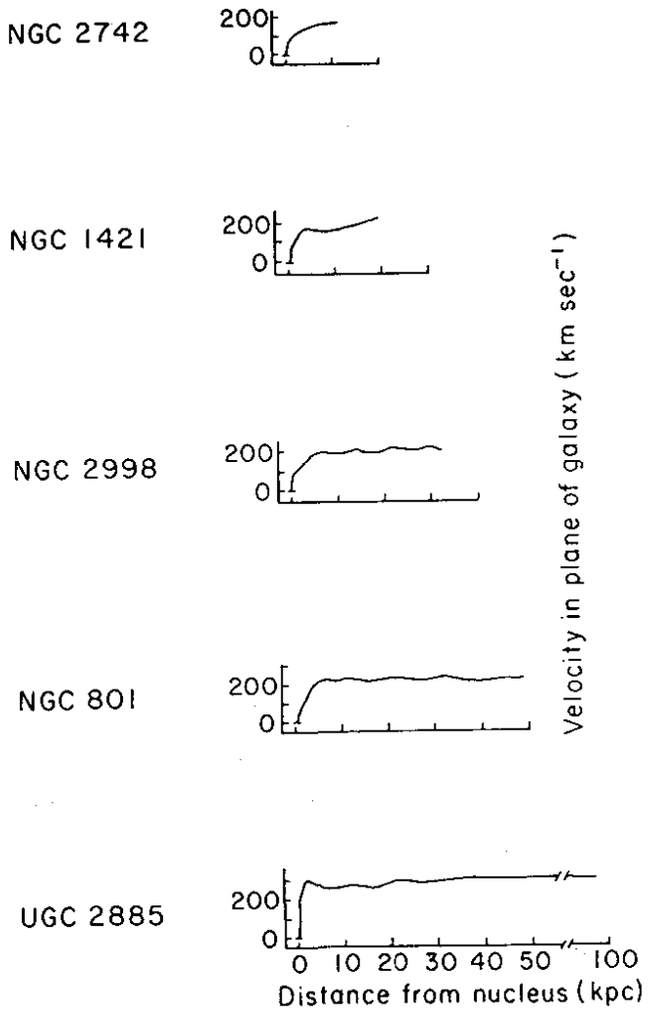

By using simple classical mechanics, it may be determined that these observations are consistent with a model of the galaxy in which M(r), the mass interior to radius r, increases linearly with r. The data are not consistent with, for example, a "central body" model, where the mass is concentrated in the centre, and then has a flat density out to the edge of the object. For such a model, the velocity should fall as $r^{-1/2}$.[32] A "mass-to-light" ratio may be calculated from these observations. Table I.1 shows this ratio for galaxies, as well as for other astronomical objects (cf. ref. 30).

Table I.1: Mass-to-light ratios of astrophysical systems in solar units (Mass of sun / Luminosity of sun). For details, cf. Ref. 30.

Scale	Mass/Light (Solar Units)
Solar neighbourhood	1.3 - 4.9
Spiral galaxies	8 - 12
Elliptical galaxies	10 - 20
Binaries and small groups	60 - 180
Galactic clusters	280 - 840

The rotation curve observations described above, as well as the other measurements summarized in Table I.1, have led some cosmologists to speculate that astronomical objects contain "dark matter" which may be massive neutrinos. The possibility of the matter being conventional particles, such as baryons, has been discounted because of arguments involving primordial nucleosynthesis and measurements of current abundances of ^{4}He, ^{7}Li, ^{3}He, and D.[31] Neutrinos with masses of O(eV) would be expected to dominate the rest of the matter in the universe (cf. p. 23 below) and could provide the necessary dark matter. The observations described above are not measurements of m_ν, or even compelling evidence for non-zero ν masses, but they do indicate the important repercussions which would result from experimental observations of neutrino masses or oscillations.

Calculations in the standard big bang picture of cosmology have been used to determine possible constraints on neutrino properties (e.g. m_ν, number of generations). The main factors in the mass limit calculation are the observed value of the Hubble parameter, calculations of the "critical density" of the universe, measurements of the hot big bang model's deceleration parameter, and a prediction of the current number density of neutrinos based on big bang calculations.

The Hubble parameter, H_0, is related to the rate of change of the scale factor, R(t), in cosmology.[33] The discussion below will use the number:

$$H_0 = 100 \text{ km}\cdot\text{s}^{-1}\cdot\text{Mpc}^{-1}$$

which is currently the largest measured value.[34] Other measurements are a factor of 2 below this value.[30,31] The larger number is more appropriate for this discussion, since it gives the least restrictive bound on m_ν.

The critical density, ρ_c, is the density required to slow down and halt the expansion of the universe (to "close the universe"). In the big bang model, ρ_c is given by:

$$\rho_c = \frac{3H_0^2}{8\pi G} = 1.88 \times 10^{-29} \text{ gm/cm}^3$$

The deceleration parameter,[33] q_0, is a function of R(t) and its first 2 derivatives. It estimated to have values ranging from 0. ± 0.5 to 1.5 ±0.5.[31] We will use an upper bound of 2. The variable, Ω, which is the ratio of the density of the universe to the critical density, is related to q_0 by :

$$q_0 = \frac{\Omega}{2} .$$

Thus we will use $\Omega = 4$. This is the highest upper bound for Ω obtained from any technique.

Finally, the number density of each neutrino species is given by:

$$n_\nu = \frac{600}{11} g_{\nu_i} \left(\frac{T_0}{2.7 \text{ K}}\right)^3$$

where g_{ν_i} is 2 for Majorana neutrinos and 4 for Dirac neutrinos. The present temperature of the universe is given by T_0. The ratio of the neutrino mass density to ρ_c may then be written as:

$$\Omega_{\nu_i} = \frac{m_{\nu_i}}{200} g_{\nu_i} \left(\frac{T_0}{2.7 \text{ K}}\right)^3$$

An upper bound to the sum of all neutrino masses is then obtained by requiring :

$$\sum_i \Omega_{\nu_i} < \Omega^{max} = 4.$$

This gives us: $\sum_i m_{\nu_i} \leq (100 \text{ eV/c}^2)\, g_\nu$. It is important to note that, assuming there are no serious problems with the theoretical calculations, this bound is the <u>least</u> restrictive one which may be derived. Estimates of all parameters (e.g. q_0, H_0) have been selected so as to obtain a conservative limit. Some authors[31] find a more restrictive limit of $\sum_i m_{\nu_i} \leq (25 \text{ eV/c}^2)\, g_\nu$ by using additional information and less extreme estimates of critical parameters.

It may also be shown that if $m_{\nu_i} \geq 1 \text{ eV/c}^2$, then

massive neutrinos dominate the matter in the universe. The upper bound for Ω_b (the ratio of the baryon mass density to ρ_c) is approximately 0.3[35]. Given the results of the previous paragraph, we have:

$$\frac{\Omega_\nu}{\Omega_b} \geq \frac{\sum_i m_{\nu_i}}{2.4\ \mathrm{eV}/c^2}$$

The observation of massive neutrinos would clearly be of great importance to cosmology.

CHAPTER II

Neutrino Oscillations

Section II.1: Formalism

We now turn from the question of the origins and general implications of neutrino masses to the particular consequence addressed by this dissertation; that is to say, neutrino oscillations. To see how neutrino oscillations arise, consider the equation:

$$|\nu_\alpha\rangle = \sum_i U_{\alpha i}|\nu_i\rangle \qquad (1)$$

Here, $|\nu_\alpha\rangle$ is a weak interaction eigenstate (e.g. $|\nu_\mu^L\rangle$), the $|\nu_i\rangle$ are the mass eigenstates, U is the unitary mixing

matrix, and i runs over all of the ν mass eigenstates which are mixed.

Using non-relativistic quantum mechanics, we may write the time-development of $|\nu_\alpha\rangle$ as:

$$|\nu_\alpha(t)\rangle = \sum_i U_{\alpha i} e^{-iE_i t} |\nu_i\rangle \qquad (2)$$

We will now assume that $|\nu_\alpha\rangle$ is a pure momentum eigenstate. While this assumption is not necessary[36], it simplifies the derivation of the oscillation formulae.

The amplitude for finding a neutrino of a flavour ν_β downstream of a pure source of ν_α is given by the matrix element:

$$\langle\nu_\beta|\nu_\alpha(t)\rangle = (\sum_j \langle\nu_j|U^*_{\beta j})(\sum_i e^{-iE_i t} U_{\alpha i}|\nu_i\rangle)$$

$$= \sum_i U^*_{\beta i} U_{\alpha i} e^{-iE_i t} \qquad (3)$$

The probability of observing ν_β is just:

$$P(\nu_\alpha \to \nu_\beta) = |\langle\nu_\beta|\nu_\alpha(t)\rangle|^2$$

$$= |\sum_i U^*_{\beta i} U_{\alpha i} e^{-iE_i t}|^2 \qquad (4)$$

The implications of this formula may best be

illustrated by considering the simplest possible mixing scheme, i.e. two neutrino mixing. Here, the matrix U is given by:

$$U = \begin{pmatrix} \cos\theta & \sin\theta \\ -\sin\theta & \cos\theta \end{pmatrix} \qquad (5)$$

The weak eigenstates (e.g. ν_e, ν_μ) are then related to the mass eigenstates (ν_1, ν_2) as:

$$|\nu_e\rangle = \cos\theta\ |\nu_1\rangle + \sin\theta\ |\nu_2\rangle$$

$$|\nu_\mu\rangle = \sin\theta\ |\nu_1\rangle - \cos\theta\ |\nu_2\rangle$$

and the probability of observing ν_e downstream of a pure ν_μ source is given by:

$$P(\nu_\mu \to \nu_e) = |\ (U_{1e}U_{1\mu})e^{-im_1^2 t/2p} + (U_{2e}U_{2\mu})e^{-im_2^2 t/2p}\ |^2$$

$$= |\cos\theta\ \sin\theta\ e^{-im_1^2 t/2p} - \sin\theta\ \cos\theta\ e^{-im_2^2 t/2p}|^2$$

$$= 0.5\ \sin^2 2\theta\ (1 - \cos\frac{\Delta m^2 \cdot t}{2p})$$

where, $\Delta m^2 = m_2^2 - m_1^2$.

Since $m_\nu << E_\nu$, and thus $\beta \simeq 1$, we have:

$$P(\nu_\mu \to \nu_e) = \sin^2 2\theta\ \sin^2(\Delta m^2\ L/4E_\nu) \qquad (6)$$

The above calculation has been done in natural units ($h = c = 1$). In order to be able to calculate P for

physical experiments, we must put the physical units back in. Equation (6) then becomes:

$$P(\nu_\mu \to \nu_e) = \sin^2 2\theta \ \sin^2 \frac{1.27\ \Delta m^2\ L}{E_\nu} \qquad (7)$$

where Δ is in eV^2, L is in metres, and E_ν is in GeV. We may define an "oscillation length", L_{osc}, as:

$$L_{osc} = \frac{2.5\ E_\nu}{\Delta m^2} \qquad (7a)$$

Equation 7 describes an "exclusive oscillation", and experiments which attempt to measure such reactions are known as "exclusive searches" or "appearance experiments". There exists another class of oscillation measurements; these are the "inclusive searches" or "disappearance experiments". For a two-neutrino mixing hypothesis, this is described by:

$$P(\nu_\mu \to \nu_\mu) = 1 - \sin^2 2\theta \ \sin^2 \frac{1.27\ \Delta m^2\ L}{E_\nu} \qquad (8)$$

This thesis describes such a measurement. A comparison and discussion of the merits and drawbacks of these two techniques follows in Section II.2.

While the simple hypothesis just noted is the standard one used in analysing the results of oscillation searches, it is useful to dwell on the more

general (and more complicated) case a little longer. It is very difficult to analyse data for the case of n-component mixing, where n > 2. For example, the 3 neutrino system could have 3 different mixing angles, 1 complex CP-violating phase (just as for the Kobayashi-Maskawa quark matrix), and 3 mass difference variables.[37,38] However, it is possible to make a simple approximation which allows one to obtain results for an arbitrary number of neutrinos. This "leading mass" approximation is given in Ref. 39, and summarized below.

We assume that, given n neutrino mass eigenstates, there is one (labelled "k") whose mass is sufficiently large compared to the others that:

$$\Delta m^2_{ik} >> \Delta m^2_{ij} \quad (i,j \neq k),$$

where $\Delta m^2_{ij} = m^2_i - m^2_j$. If this is true, then all oscillations between states i and j (both not equal to k) may be neglected. To see this, recall equation 3:

$$\langle \nu^0_\beta | \nu_\alpha(t) \rangle = \sum_i U^*_{\beta i}\ U_{\alpha i}\ e^{-iE_i t}$$

This may be re-written as:

$$\langle \nu^0_\beta | \nu_\alpha(t) \rangle = U^*_{\beta k} U_{\alpha k} + \sum_{i \neq k} U^*_{\beta i} U_{\alpha i} e^{-i\Delta m^2_{ik} L/2E_i}$$

(where we have neglected an overall phase). By using the fact that if U is a unitary matrix, then:

and we obtain: $\delta_{\alpha\beta} = \sum_i U^*_{\beta i} U_{\alpha i}$

$$\langle \nu^0_\beta | \nu_\alpha(t) \rangle = \delta_{\alpha\beta} + \sum_{i \neq k} U^*_{\beta i} U_{\alpha i} \left(e^{-i\Delta m^2_{ik} L/2E_i} - 1\right) \quad (9)$$

If Δm^2_{ik} is large for all i, then we may assume that $\Delta m^2_{ik} = \Delta$ for all i, so that:

$$\langle \nu^0_\beta | \nu_\alpha(t) \rangle = \delta_{\alpha\beta} + \sum_{i \neq k} U^*_{\beta i} U_{\alpha i} \left(e^{-i\Delta m^2 L/2E} - 1\right)$$

$$= \delta_{\alpha\beta} + \left(-U^*_{\beta k} U_{\alpha k} + \sum_i U^*_{\beta i} U_{\alpha i}\right) \left(e^{-i\Delta m^2 L/2E} - 1\right)$$

This reduces to:

$$\langle \nu^0_\beta | \nu_\alpha(t) \rangle = \delta_{\alpha\beta} + (\delta_{\alpha\beta} - U_{\alpha k} U^*_{\beta k}) \left(e^{-i\Delta m^2 L/2E} - 1\right) \quad (10)$$

For the inclusive oscillations, $\alpha = \beta$, the probability is given by:

$$P(\nu_\alpha | \nu_\alpha) = |\langle \nu^0_\alpha | \nu_\alpha(t) \rangle|^2$$

$$= 1 - 4\left(|U_{\alpha k}|^2 - |U_{\alpha k}|^4\right) \sin^2\left(\frac{\Delta m^2 L}{2E}\right) \quad (11)$$

Comparing this result to equation (8), we see that the form of the inclusive oscillation for the leading mass approximation (with <u>any</u> number of neutrinos) is identical to that for the simple 2 neutrino case, with the quantity: $4(|U_{\alpha k}|^2 - |U_{\alpha k}|^4)$ substituted for $\sin^2 2\theta$. This means that a

limit on inclusive two-component oscillations may trivially be converted into a limit on $U_{\alpha k}$ by using equation 11 instead of equation 8:

$$|U_{\alpha k}|^2 \leq \frac{1 - \sqrt{1 - \sin^2 2\alpha}}{2} \quad (12a)$$

or

$$|U_{\alpha k}|^2 \geq \frac{1 + \sqrt{1 - \sin^2 2\alpha}}{2} \quad (12b)$$

For example, if one has obtained the limit $\sin^2 2\theta \leq .05$, then it may also be concluded in the leading mass limit that:

$$0 \leq |U_{\alpha k}|^2 \leq .013 \text{ or } .987 \leq |U_{\alpha k}|^2 \leq 1.00$$

for an arbitrary number of neutrinos in the leading mass approximation.

Before moving on to the description of experimental techniques for neutrino oscillation searches, it is interesting to discuss the implications of CPT and CP invariance (or non-invariance).[39] Consider the oscillation:

$$|\nu^L_\alpha\rangle \rightarrow |\nu^L_\beta\rangle \quad (13)$$

Here, α and β indicate weak eigenstates (e.g. e, μ, τ), and the superscript L (R) means that the state is left- (right-) handed. If CPT is conserved, then we may apply it to equation 13 and obtain:

$$CPT(|\nu_\alpha^L\rangle \to |\nu_\beta^L\rangle) = CP(|\nu_\beta^L\rangle \to |\nu_\alpha^L\rangle)$$

$$= C(|\nu_\beta^R\rangle \to |\nu_\alpha^R\rangle)$$

$$= |\bar{\nu}_\beta^R\rangle \to |\bar{\nu}_\alpha^R\rangle$$

For example, this means that:

$$\text{Prob.}(|\nu_\mu^L\rangle \to |\nu_e^L\rangle) = \text{Prob.}(|\bar{\nu}_e^R\rangle \to |\bar{\nu}_\mu^R\rangle) \qquad (14a)$$

$$\text{Prob.}(|\nu_\mu^L\rangle \to |\nu_\mu^L\rangle) = \text{Prob.}(|\bar{\nu}_\mu^R\rangle \to |\bar{\nu}_\mu^R\rangle) \qquad (14b)$$

Equation 14b gives the two reactions studied by the experiment described herein.

If CP is conserved then we have:

$$CP(|\nu_\alpha^L\rangle \to |\nu_\beta^L\rangle) = C(|\nu_\alpha^R\rangle \to |\nu_\beta^R\rangle) = |\bar{\nu}_\alpha^R\rangle \to |\nu_\beta^R\rangle.$$

For example, this indicates that:

$$\text{Prob.}(|\nu_\mu^L\rangle \to |\nu_e^L\rangle) = \text{Prob.}(|\bar{\nu}_\mu^R\rangle \to |\bar{\nu}_e^R\rangle) \qquad (15a)$$

$$\text{Prob.}(|\nu_\mu^L\rangle \to |\nu_\mu^L\rangle) = \text{Prob.}(|\bar{\nu}_\mu^R\rangle \to |\bar{\nu}_\mu^R\rangle) \qquad (15b)$$

If neutrino oscillations were observed, it would thus be interesting to compare exclusive channels involving neutrinos and anti-neutrinos of the same flavour to determine their CP properties. On the other hand, comparison of inclusive channels gives information on the CPT properties of the neutrino states.

Section II.2: Exclusive Searches

In the discussion to follow, we will restrict ourselves to working within the two-component mixing hypothesis. This is the model which is used by most experimental groups in analysing their data. Recalling equation (7), we may write the probability of an oscillation as a function of distance as:

$$P(\nu_\alpha \to \nu_\beta) = \sin^2 2_\alpha \, \sin^2\left(\frac{1.27\ \Delta m^2\ L_{det}}{E_\nu}\right) \qquad (7)$$

$$(\alpha \neq \beta)$$

In an ideal experiment, one would start with a pure beam of ν_α (i.e. no ν_β contamination in the beam), and measure the ν_α and ν_β event rate at a detector downstream of the neutrino source. The ratio given by[40]:

$$R_{ab} = R(\nu_\alpha \to \nu_\beta) = \frac{N_\beta}{N_\alpha}$$

$$= \frac{\int\int P(\nu_\alpha \to \nu_\beta)\cdot\phi_\alpha\ \sigma_\beta\ dE\cdot dl}{\int\int \phi_\alpha(E)\cdot\sigma_\alpha(E)\ dE\cdot dl}$$

is then used to extract $P(\nu_\alpha \to \nu_\beta)$ and thus $\sin^2 2_\alpha$ and Δm^2. Here, $\phi_\alpha(E)$ is the flux of ν_α (assuming no oscillations), $\sigma_\alpha(E)$ ($\sigma_\beta(E)$) is the cross-section for ν_α (ν_β) interacting in the detector, E is the neutrino energy, and l is the

distance from the neutrino source to the detector. In practise, neutrino beams are not mono-energetic and do not originate from a point source.

Unfortunately, it is not possible to do an ideal experiment. In particular, there is always a fraction of ν_β in the neutrino beam which must be subtracted from the observed rate in order to determine $R_{\alpha\beta}$. The criteria for carrying out a sensitive search are[40]: (i) minimizing the ν_β contamination in the beam; (ii) maximizing the ν_α event rate; and (iii) maximizing the value of L_{det}/E_ν. Point (i) is important since the systematic uncertainty in the ν_β subtraction will provide a lower limit to the sensitivity of an experiment to small values of $R_{\alpha\beta}$. Point (ii) is also obvious; by increasing N_α, one may seek to measure smaller values of $R_{\alpha\beta}$.

Point (iii) is a little more subtle. For very small values of the argument of the second sine function in equation (7), the probability of an oscillation may be approximated as:

$$P(\nu_\alpha \rightarrow \nu_\beta) \longrightarrow \left(\frac{1.27 \cdot \Delta m^2 \cdot L}{E_\nu}\right) \sin^2 2\alpha \qquad (17)$$

For fixed values of $\sin^2 2\alpha$ and Δm^2, $R_{\alpha\beta}$ increases as $\frac{L}{E}$ increases. It should be noted that it is difficult to optimize points (i), (ii), and (iii) simultaneously. For

example, in a wide band neutrino beam the number of neutrinos drops as L^{-2},[40] where L is the distance from the neutrino source. Thus, if a detector is placed at large L to maximize $\frac{L}{E}$, the rate of ν_α goes down. Another problem is that σ_ν rises with energy,[41] so that decreasing E_ν to increase $\frac{L}{E}$ reduces N_a.

The sensitivity of an exclusive search is either presented graphically (as in Ch. VI) or by giving the limits at the following extremes:

$$P(\nu_\alpha \rightarrow \nu_\beta) \xrightarrow[\Delta m^2 \rightarrow \infty]{} 0.5 \cdot \sin^2 2\alpha \qquad (18a)$$

$$P(\nu_\alpha \rightarrow \nu_\beta) \xrightarrow[\substack{\Delta m^2 \rightarrow 0 \\ \sin^2 2\alpha \rightarrow 1}]{} \frac{1.27 \cdot \Delta m^2 \cdot L}{E} \qquad (18b)$$

The best current results are given in Chapter VI.

Section II.3: Inclusive Searches

In the two-neutrino mixing model, the probability of an oscillation is given by equation (8):

$$P(\nu_\mu \rightarrow \nu_\mu) = 1 - \sin^2 2\alpha \ \sin^2 \frac{1.27\ \Delta m^2\ L}{E_\nu} \qquad (8)$$

An inclusive search has a clear advantage over exclusive searches in that it is sensitive to any type of oscillation, whereas exclusive searches are only sensitive to specific channels. For example, if a new charged sequential lepton existed which was too heavy to be observed at current e^+e^- colliders[42] (i.e. $m_L \gtrsim 18$ GeV/c^2), then the charge-current interaction of the associated neutrino, ν_L, would be kinematically impossible in current neutrino beams ($E_\nu <$ 300 GeV or $\sqrt{s} <$ 11.9 GeV). The only way to observe the oscillation $\nu_\mu \rightarrow \nu_L$ would be through the inclusive measurement (i.e. $\nu_\mu \rightarrow \nu_x$). Similarly, an oscillation of the standard left-handed neutrino (ν_μ^L) into a "sterile" right-handed neutrino (ν_μ^R) could only be detected inclusively, since ν_μ^R would not interact with the standard V-A coupling.

There are two ways to do an inclusive search for neutrino oscillations. They are called "one detector" and "two detector" measurements. The two detector measurement is done by measuring the neutrino flux at two different

distances from the neutrino source. Given a point source of mono-energetic neutrinos, the quantity which such an experiment measures is:

$$R = \frac{1 - \sin^2 2\alpha \left(\frac{1.27 \cdot \Delta m^2 \cdot L_1}{E_\nu}\right)}{1 - \sin^2 2\alpha \left(\frac{1.27 \cdot \Delta m^2 \cdot L_2}{E_\nu}\right)} \qquad (19)$$

where L_1 and L_2 are the distances from the source to detectors 1 and 2, respectively. Such an ideal oscillation is shown in Fig. II.1.

Figure II.1: Shown is the predicted ratio of fluxes at two different detectors (723 m and 1080 m downstream of the source) in a mono-energetic neutrino beam (of energy E_ν) as a function of the oscillation parameters Δm^2 and $\sin^2 2\theta$.

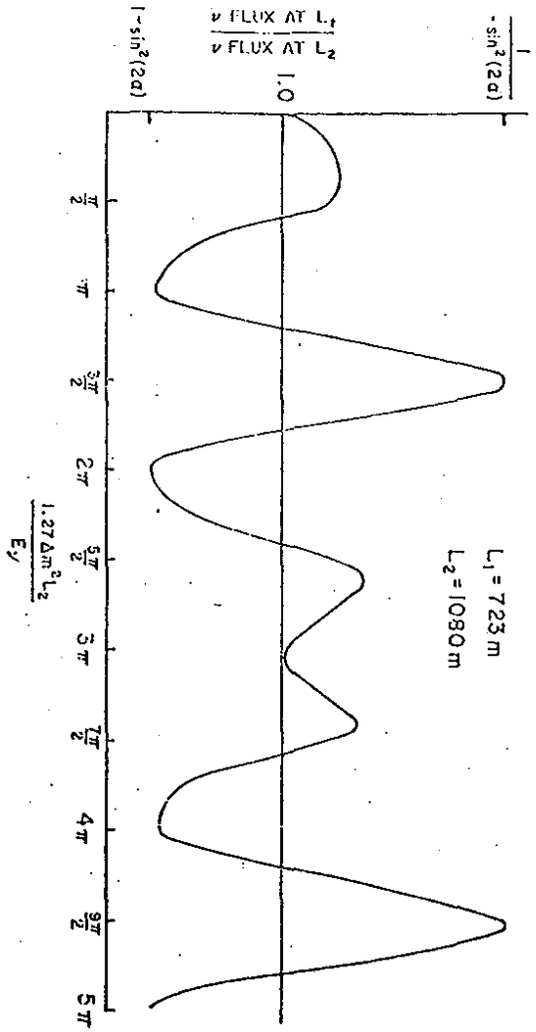

The one detector measurement may be thought of as a special case of the two detector experiment, where one detector is placed exactly at the neutrino source. A calculation of the "exact" neutrino flux at the source serves as that detector; a precise knowledge of the neutrino cross-section is also needed. Fig. II.2 illustrates the 2 types of oscillation measurement's dependence on L_{osc}.

The systematic limitations of the two types of measurements are somewhat different. There are three different effects which limit the two-detector experiment. These are the finite physical size of the neutrino source, the energy resolution of the neutrino detectors, and the counting rate at the detectors.

Figure II.2: The effect of the finite energy resolution and source size is illustrated by showing detectors located at two values of L/E_ν. For large values of Δm^2, both detectors are in the region of rapid oscillations; the signal is thus obscured. If the first detector were located at the ν source, then the experiment would be sensitive to oscillations even at the high values of Δm^2. This is also the case if the neutrino flux may be calculated "exactly".

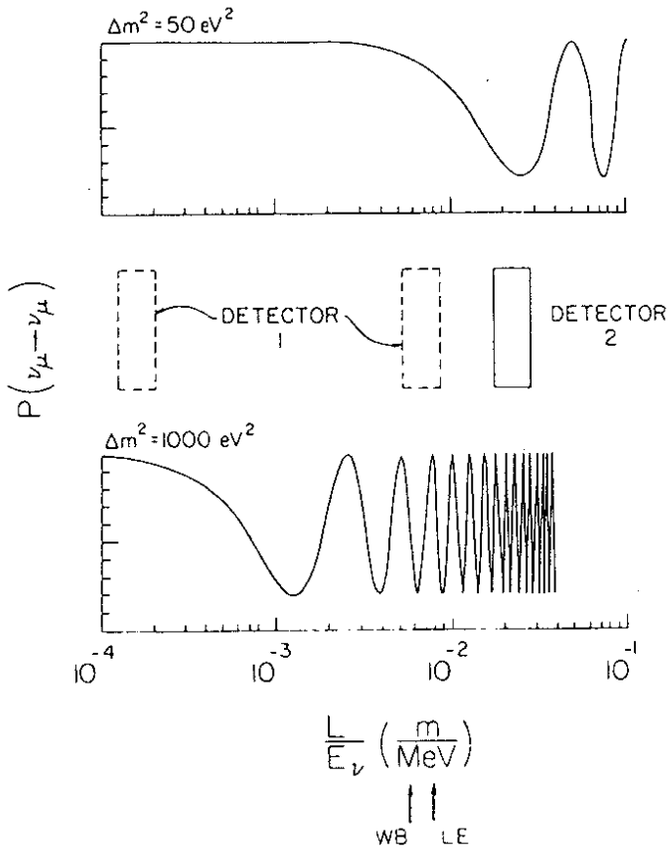

The finite size of the neutrino source creates a problem because of the L dependence in equation (19). Any uncertainty in the knowledge of where the neutrino originated leads to an uncertainty in the expected value of R. An estimate of this effect may be obtained by taking the limiting case: $L_{osc} < L_{source}$. Recalling equation (7a), we have:

$$\frac{2.5 \cdot E_\nu}{\Delta m^2} < L_{source}$$

or

$$(\Delta m^2)^L_{max} = \frac{2.5 \cdot E_\nu^{max}}{L_{source}} \qquad (20a)$$

where $(\Delta m^2)^L_{max}$ is the point where the experiment is insensitive due to the source size. This quantity is given in Table II.1 for two different experiments.

Table II.1: Limits on the sensitivity of two detector inclusive ν oscillation searches. Indicated are the cut-offs due to the finite source size, finite energy resolution, and counting rate for two different experiments (cf. equations 20a,b,c). The CDHS experiment did not directly measure E_ν, and thus that limit in sensitivity is not given.

	CCFR	CDHS
E_ν	30-230 GeV	1.0-1.5 GeV
L_{source}	352 m	52 m
$\Delta E_\nu/E_\nu$	0.10	----
L_{near}	715 m	130 m
L_{far}	1116 m	885 m
δR	0.05	0.10
$(\Delta m^2)^L_{max}$	1630 eV^2	70 eV^2
$(\Delta m^2)^E_{max}$	1600 eV^2	----
$(\Delta m^2)_{min}$	5 eV^2	0.1 eV^2

The energy resolution of the experiment gives a similar cut-off in sensitivity for large values of Δm^2. This is because the energy resolution is directly related to the resolution in L_{osc}. This effect may be estimated by demanding that the L_{osc} resolution be less than 20 %. We then have (using equation (7a)):

$$\frac{\Delta E_\nu}{E_\nu} < \frac{0.2}{N_{osc}}$$

or

$$\frac{\Delta E_\nu}{E_\nu} < \frac{0.2 \cdot L_{osc}}{L_{det}}$$

where L_{det} is the distance to the neutrino detector from the source. We then obtain the maximum Δm^2 which can be measured:

$$(\Delta m^2)^E_{max} = \frac{0.5\ E_\nu^{max}}{\left(\frac{\Delta E_\nu}{E_\nu}\right) L} \qquad (20b)$$

It is given in Table II.1 for the same two examples as were used for $(\Delta m^2)^L_{max}$.

At low values of Δm^2, the counting rate leads to a limit in sensitivity. Here, we may approximate equation (19) as:

$$R \simeq 1 + \sin^2 2\theta\ (L_{near} - L_{far})\ \frac{1.27 \cdot \Delta m^2}{E_\nu^{min}}$$

where L_{near} and L_{far} are the distances to the near and far detectors, respectively. An experiment has no sensitivity when:

$$\delta R \simeq |R - 1|$$

δR being the error on the ratio R. Thus we obtain (for full mixing):

$$(\Delta m^2)_{min} = \frac{(\delta R) \cdot E^{min}}{1.27 \cdot (L_{near} - L_{far})} \qquad (20c)$$

This is also given in Table II.1 for the same two experiments as above.

In Table II.1, the limits on the sensitivity for the experiment described herein are shown under the label "CCFR". These limits mean that the CCFR experiment is sensitive to relatively high values of Δm^2. This region is very interesting when the ITEP neutrino mass measurement,[9,43] and the cosmological considerations[32] are recalled. These suggest neutrino masses of approximately 30 eV/c^2. Several neutrinos with mass in this range could lead to oscillations in the CCFR sensitive region (e.g. $m_1 = 30\ eV/c^2$, $m2 = 20\ eV/c^2$ give $\Delta m^2 = 500\ eV^2/c^4$). Inclusive oscillation experiments have been reviewed in Refs. 43 and 44; they are also summarized in Chapter VI.

CHAPTER III

The Experimental Apparatus

Section III.1 The Neutrino Detectors

The neutrino event rate was measured by detectors in the Wonder Building and Lab E. The Wonder Building (WB) detector, which was centred 715 m from the middle of the decay pipe, was especially constructed for the oscillation measurement. It is described in Section I.1.1. The Lab E detector, which was centred 1116m from the middle of the decay pipe, had been used previously in measurements of neutrino total cross-sections[41,45,46], charged current nucleon structure functions[47,48,49], and neutral current

interactions.[50] A brief description of this apparatus is given in Section I.1.2; the detector has been described in more detail elsewhere.[45,46,48,49]

Section I.1.1: The Wonder Building Detector

The Wonder Bldg. detector (cf. Fig. III.1) consisted of an iron target calorimeter and a toroidal muon spectrometer. The calorimeter was composed of 108 metric tons of 1.5-m x 1.5-m x 5.1-cm steel plates (type SAE1020), 56 1.5-m x 1.5-m x 2.54-cm acrylic scintillation counters, and 17 1.5-m x 3-m spark chambers. These detector components were arranged in a pattern (cf. Fig. III.2) which was repeated 18 times to form the calorimeter. The muon spectrometer is shown in detail in Fig. III.3. Pairs of 1.5-m x 3-m chambers were used to form 3-m x 3-m planes both in front of and in back of the 15-m radius iron toroidal magnet. Information obtained from four additional planes of scintillation counters (labelled Veto, T1, T2, and T3 in Fig. III.1) was used, together with information from the calorimeter, to trigger the detector.

The aforementioned detector components, their read-outs, and the fast triggering logic are described below in more detail.

Figure III.1: Plan view of the Wonder Building detector. Shown (in the y-view) are the calorimeter and the spectrometer. The trigger counters are labelled Veto, T1, T2, and T3.

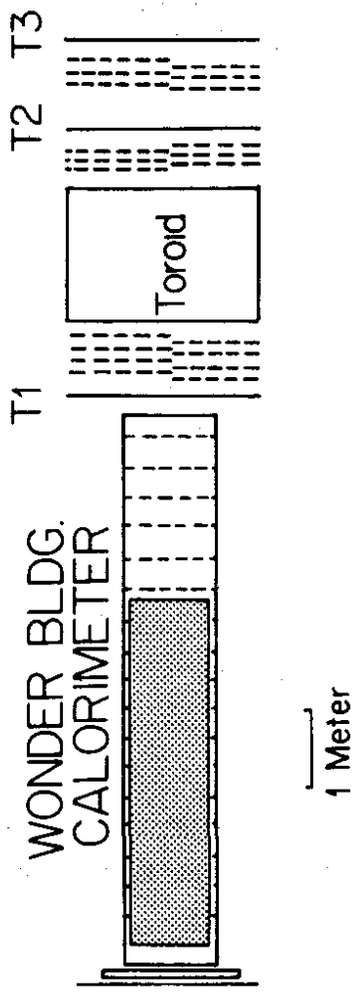

Figure III.2: The calorimeter "module" is shown in detail in both (a) x- and (b) y-views. This pattern is repeated 18 times to form the complete calorimeter.

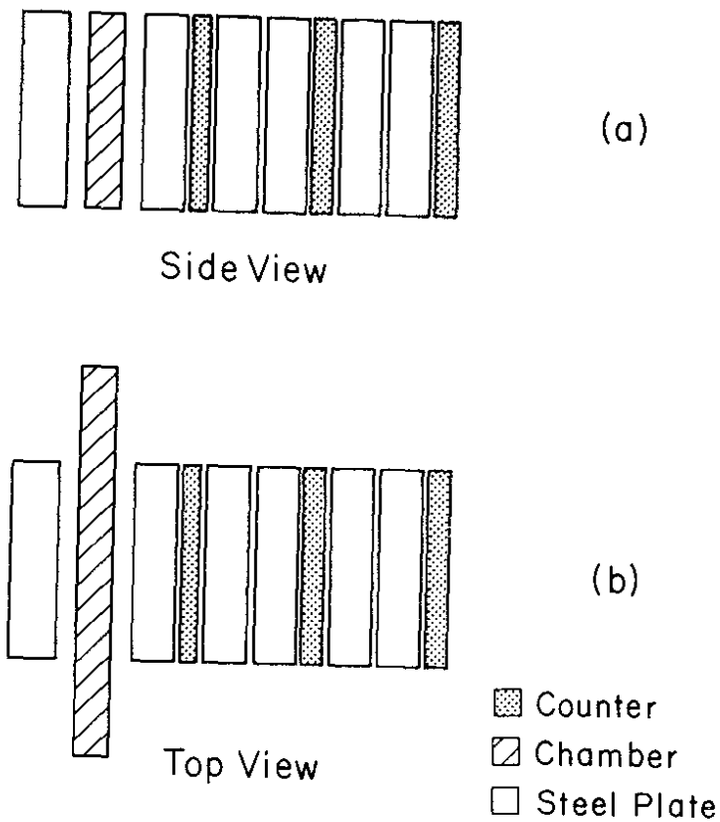

Figure III.3: The Wonder Bldg. spectrometer is shown in the y-view. The locations of the trigger counters T2 and T3, and of the steel plates are given with respect to the 96" long magnet. The spark chambers are not shown.

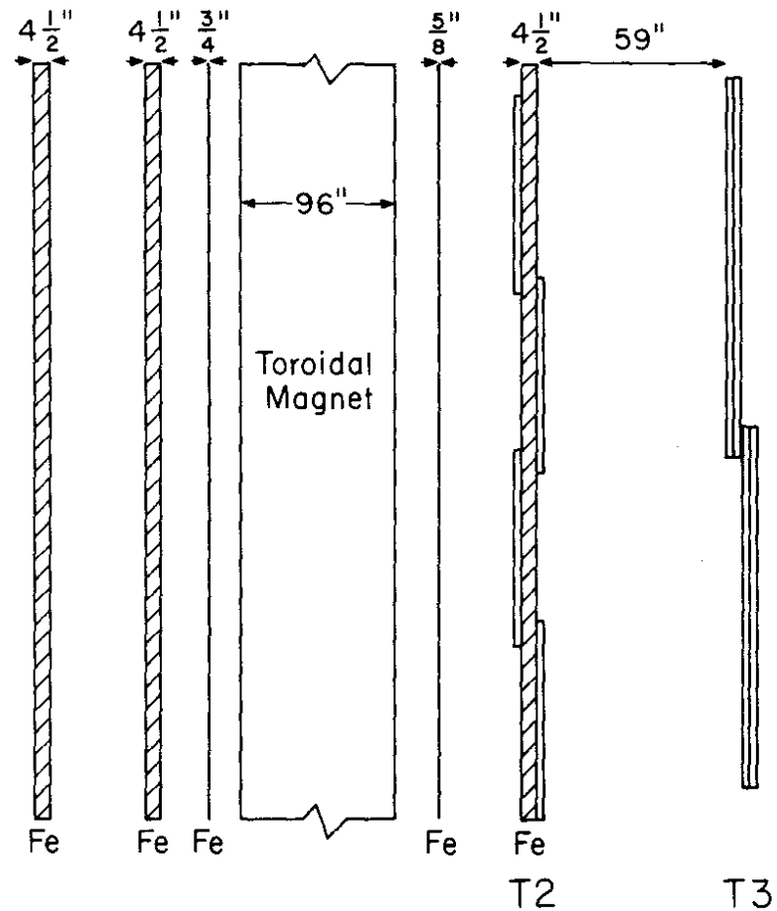

(a) Trigger Counters

There were four planes of scintillation counters which were used for trigger purposes only. Most of these trigger counters were constructed of plastic scintillator, although a few components of T3 were acrylic. The scintillator which was used in each counter is given in Table III.1, and the arrangement of the components of each counter is shown in Fig. III.3, 4, and 5. These counters were read out using the wave-shifter bar technique[51], as were the calorimetry counters.

Table III.1: The type of scintillator in each of the counter or counter segments in both detectors are shown.

Detector	Counter	Scintillator Type
Wonder Bldg.	Veto	NE110
	T1	NE110
	T2	NE114
	T3	NE110 (1 segment) Acrylic (3 segments)
	Calorimetry	Acrylic
Lab E	Veto	NE114
	T1	NE110
	T2	NE110
	T3	NE110
	Calorimetry	Liquid

Figure III.4: Counter T1 and the Veto are shown in a side view, indicating the overlap between the different trigger counter segments.

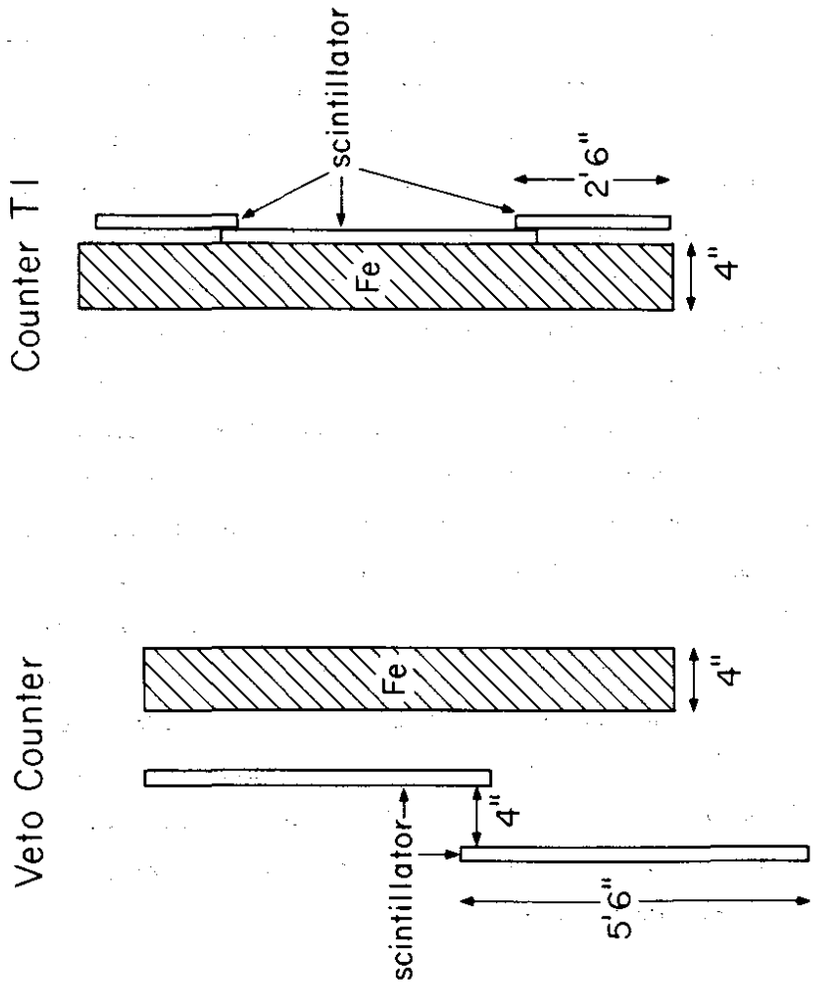

Figure III.5: Plan views (looking downstream) of the trigger counter segments. Shown are (a) the Veto counter, (b) Counter T1, (c) Counter T2, and (d) Counter T3.

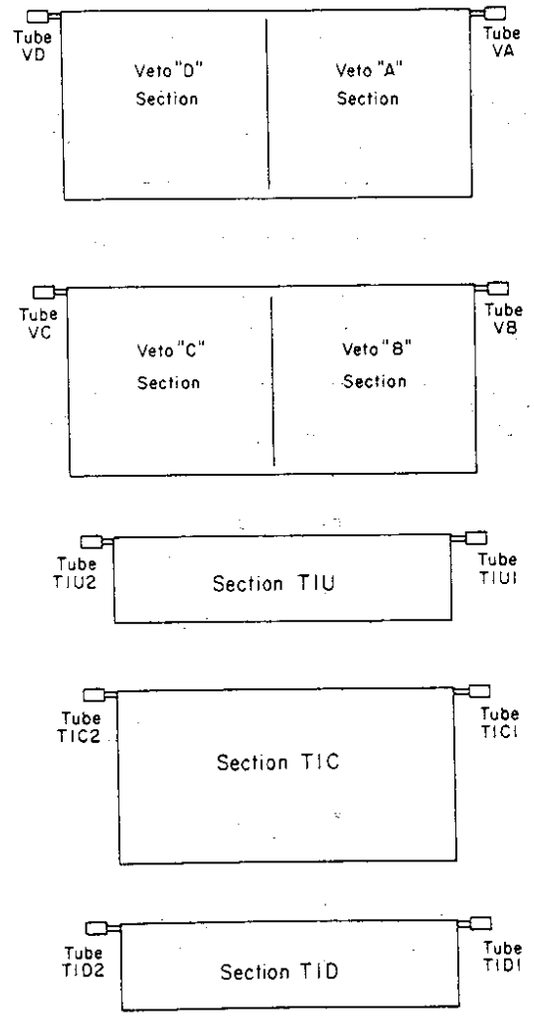

Figure III.5 (cont.):

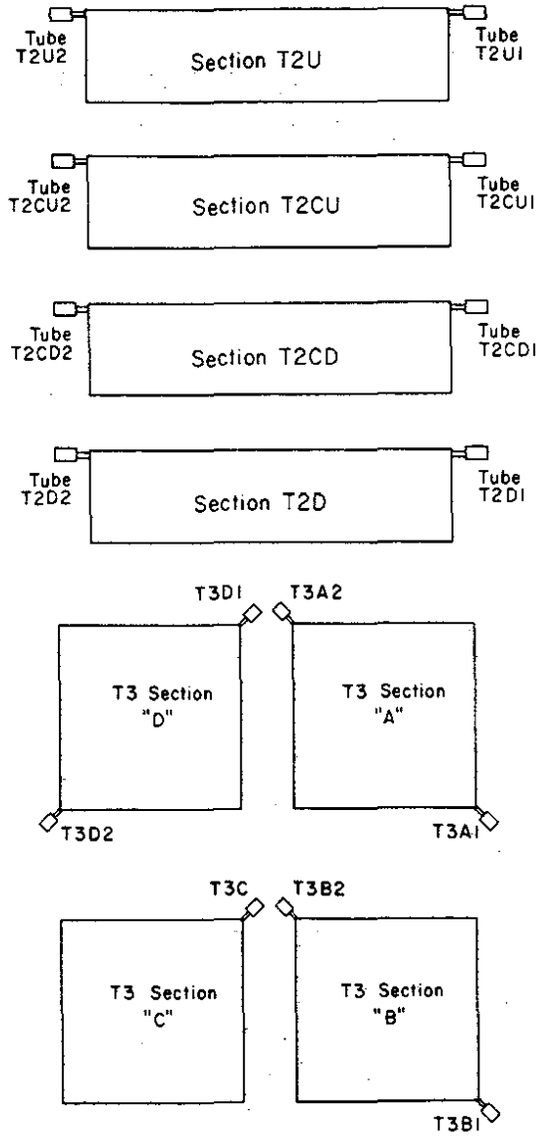

The wave-shifter bar technique is shown schematically in Fig. III.6. When a charged particle passes through the scintillator, it may raise an organic molecule (fluor) into an excited state. This state decays, emitting an ultra-violet photon ($\lambda \sim 370$ nm). The scintillator is doped with a second fluor which almost immediately absorbs the U.V. light and emits blue light ($\lambda \sim 420$ nm). This fluor is necessary because U.V. light has a small attenuation length. The blue light travels through the counter, a fraction of it being contained by total internal reflection, and is absorbed by a third fluor (BBQ) in the wave-shifter bar. This fluor is chosen to absorb blue light and emit green light ($\lambda \sim 520$ nm). The green light travels along the shifter bar to the phototube. A small air gap between the shifter bar and the scintillator prevents the green light from escaping back into the counter. The shifter bar is wrapped with Al foil to reflect back any unshifted blue light into the bar and thus increase the light collection efficiency. The light is observed by a RCA 56AVP phototube.[52] Using this technique, approximately 15 % of the scintillation light reaches the phototubes. The counters were wrapped in a double layer of Marvel Guard,[53] and mounted in aluminum frames.

Figure III.6: The wave-shifter bar read-out technique is illustrated (cf. p. 54).

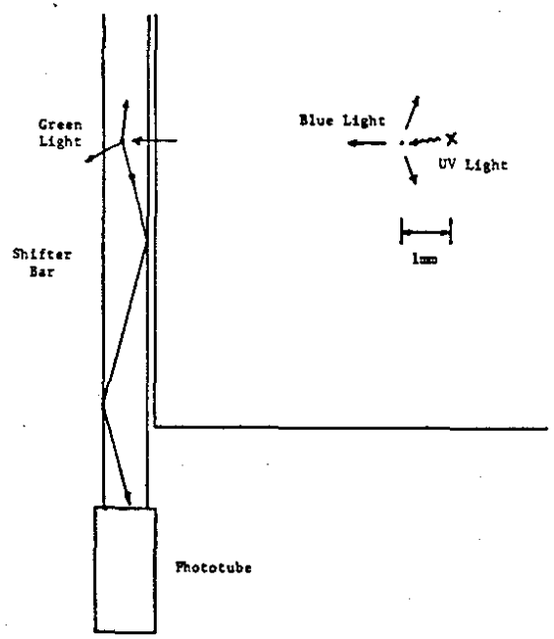

The trigger counters were operated between 2100v and 2500v. For each type of scintillator used, the efficiency plateau of at least one counter was measured. The operating voltage was then chosen to be sufficiently high that the tube was operating on the plateau, but not so high that the singles rates were unacceptable. The singles rates for the trigger counters ranged from 2 to 20 KHz during the run. Most trigger counter voltages were not determined by actually measuring an efficiency plateau. Instead, a 0.30 mCi γ-ray ^{137}Cs source was used to set the voltage of any given counter by referring to a counter whose plateau had been measured. The response of such a "reference" counter to a source placed at its centre was determined using a digital volt meter (DVM), measuring voltage across a 10k resistor to ground and thus determining the phototube current. The voltages on all other counters with the same type of scintillator and the same dimensions were then set to have the same phototube current with the source. For those counters with two phototubes (i.e. all but one), the response of each tube to a source at the centre of the counter was required to be the same.

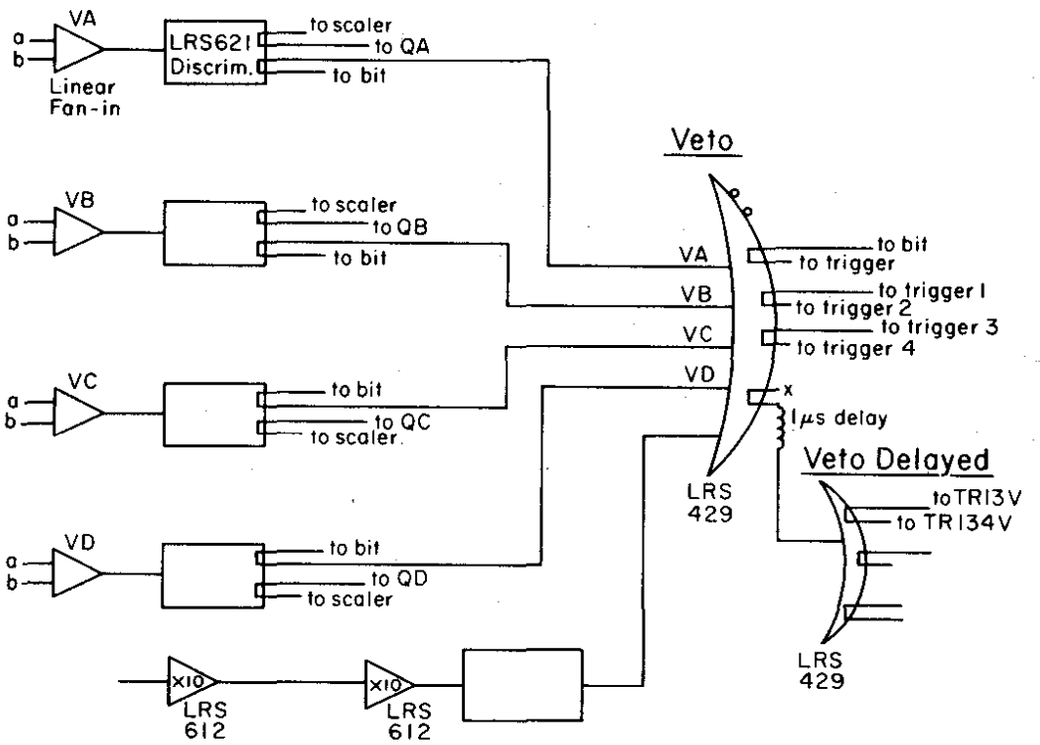

Figure III.7(a): Fast logic for Veto counter.

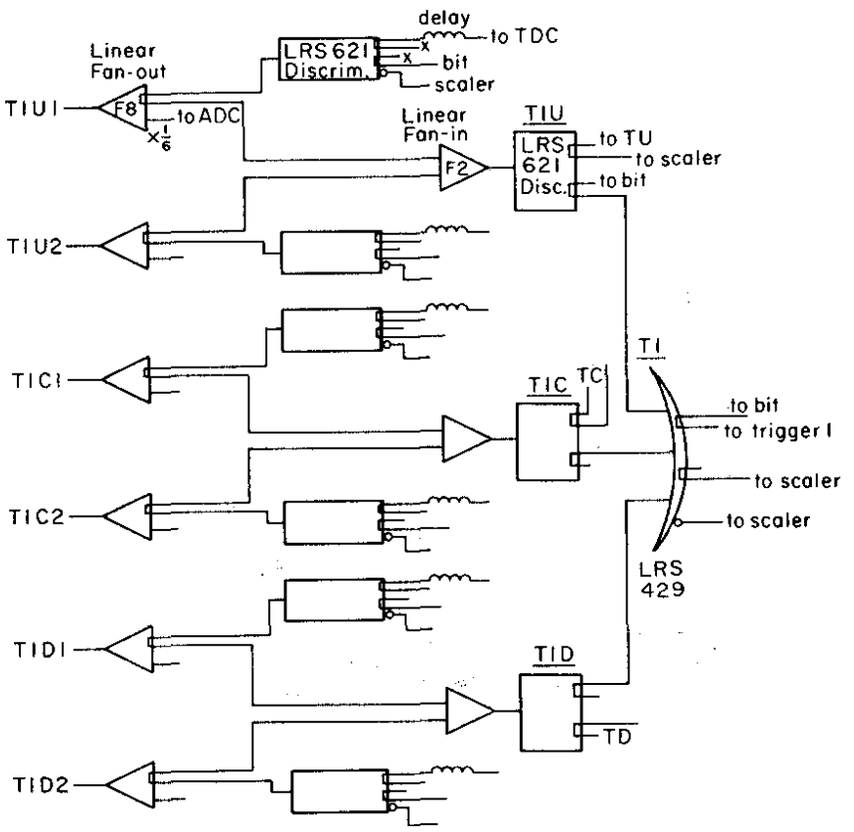

Figure III.7(b): Fast logic for trigger counter T1.

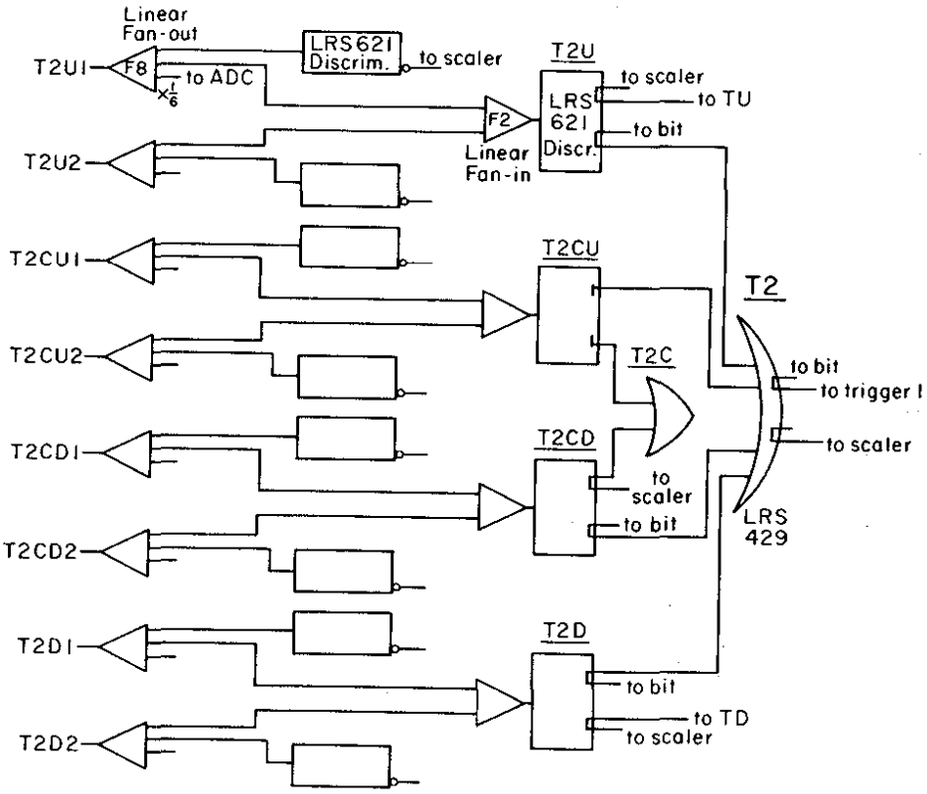

Figure III.7(c): Fast logic for trigger counter T2.

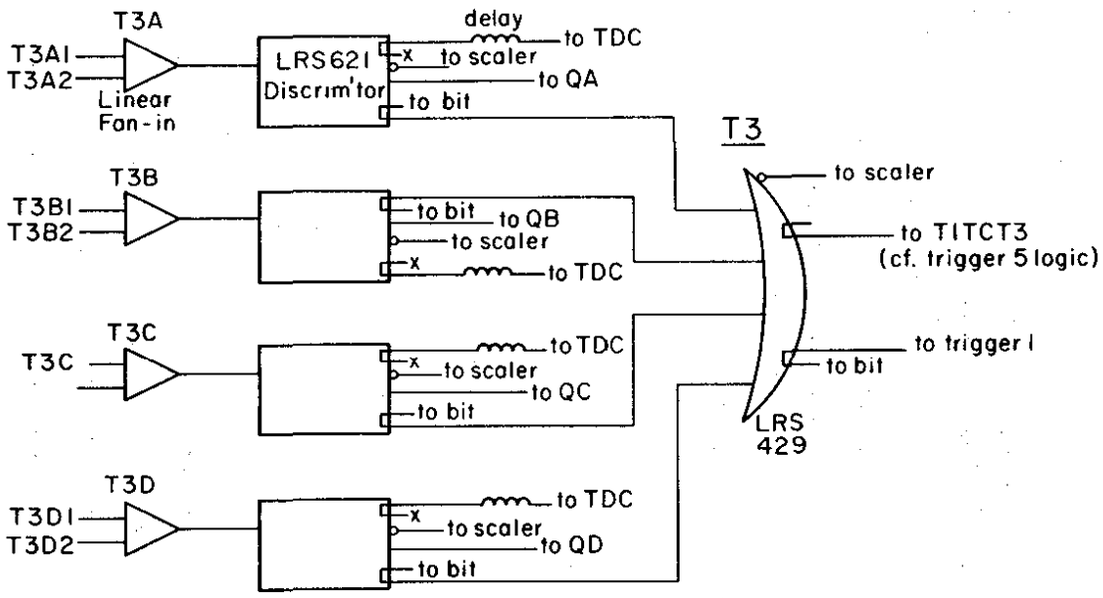

Figure III.7(d): Fast logic for trigger counter T3.

The fast logic for the trigger and veto counters is shown in Fig. III.7. The output signals from each phototube base on trigger counters T1 and T2 were sent to fan-outs via fast RG-8 foam cable. Three signals were generated by each fan-out; one was attenuated by a factor of six, while the other two were not attenuated. The attenuated signal was sent to an ADC channel. One un-attenuated signal was sent to a pulse height discriminator whose threshold was set to 50 mv (efficient for one minimum ionizing particle). The logic levels which were generated by this discriminator were sent to the bit modules, scalers, and TDCs.

The second non-attenuated signal for a tube was added to the corresponding signal from the other tube on that trigger counter segment by using a linear fan-in. The summed pulse height was discriminated (threshold of 80 mv), again so as to be efficient for a single minimum ionizing particle. The resulting logic pulse was used as part of the neutrino interaction and calibration triggers. It was also recorded by scaler and bit modules. When any of the segments of a counter fired, the "or" of the signals from the segments of that trigger counter produced a logic signal which was sent to the event triggers, as well as to scaler and bit modules. The signals from the Veto counter were used to reject muons entering through the front of the apparatus.

The fast logic for counter T3 and the veto wall was similar to that described above, except that information from the individual phototubes was not used. Rather, the summed signals from the trigger counter segments were used to form triggers, and were sent to bit, TDC, and scaler modules.

A few remarks should be made about features peculiar to the Veto counter logic. A "noise veto" was incorporated into the "or" of the signals from the four segments of the counter. This was the noise picked up by the loose end of a cable, amplified by a factor of 100. This signal was used to reject the very small number of triggers due to externally generated noise. One of the outputs of the Veto "or" was delayed by 1 μs, and then fanned out to five partial triggers. This signal was used in determining the deadtime caused by accidental firing of the veto. This procedure will be described in Chapter V of this thesis.

Figure III.8: Shown is the layout of a Wonder Building calorimetry counter.

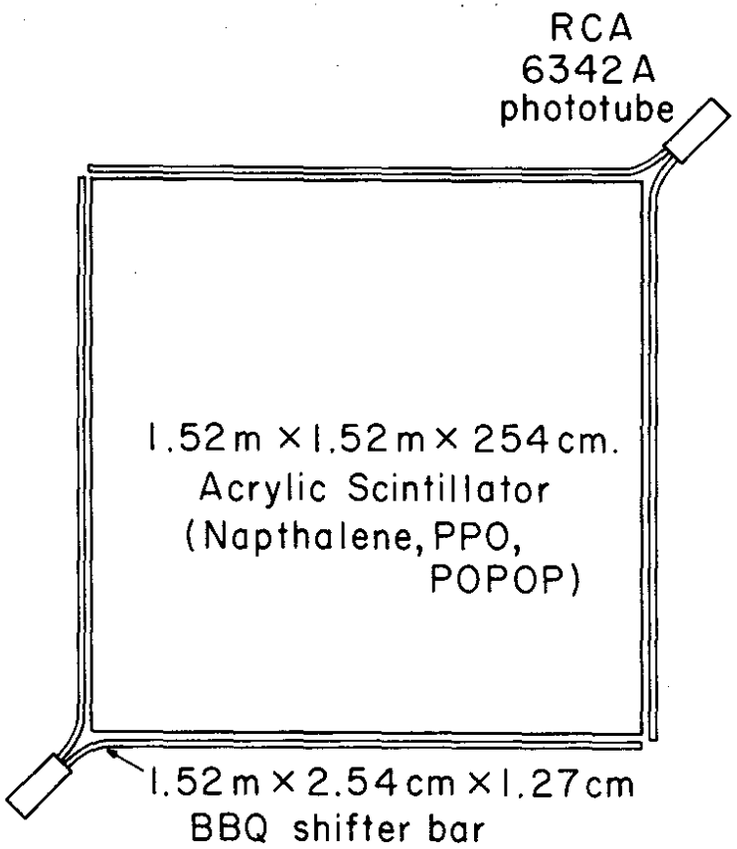

(b) Calorimetry Counters

The design of the 1" thick 5' x 5 ' calorimetry counters was similar to that of the trigger counters, and is shown in Fig. III.8. The scintillating material was acrylic[54] doped with Napthalene (10%), PPO (1%), and POPOP (0.01%). The primary fluor was PPO and the secondary fluor was POPOP. The scintillator measured 1.5-m x 1.5-m x 2.54-cm and was read out via a wave-shifter bar with a RCA 6342A phototube (S-11 photocathode).[52] The orientation of the phototubes and the counter alternated throughout the calorimeter, i.e. the top tube of counter 1 was on the west side of the target, the top tube of counter 2 was on the east side, etc.

Figure III.9: Response map of a sample Wonder Bldg. calorimetry counter obtained in measurements with a radio-active source.

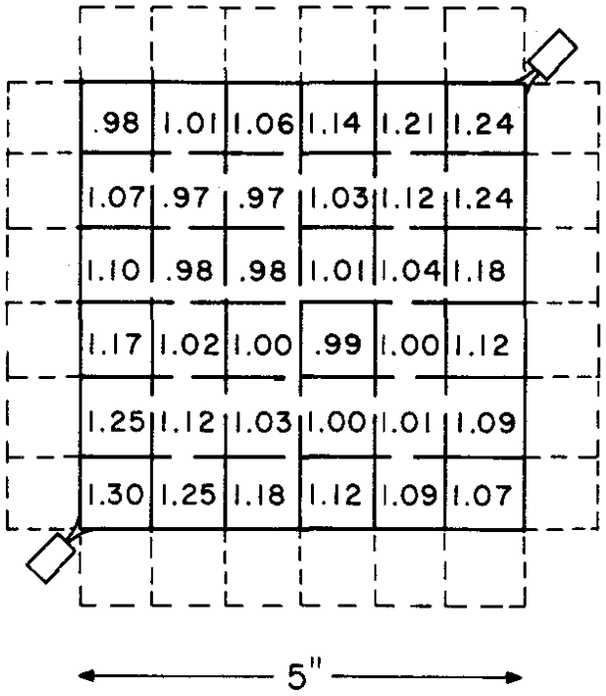

The attenuation length and light output of each counter were measured before assembly. In addition, it was necessary to measure the response of the counter as a function of position. This was done with a ^{60}Co γ-ray source (0.70 mCi). The response to the source was mapped on a 6 x 6 square grid (cf. Fig. III.9), as well as at "symmetry points" off the edges of the counter. These symmetry points were used to compensate for the finite divergence of the γ-ray source which led to losses out the side of the counter. The response at the symmetry points was approximately 10 % of that at the edge points. The map measurements were performed with the counters in an upright position. This was done to minimize reflections of γ-rays from the floor.

The phototube voltages (which ranged from 1250v to 1600v) were set so that the tubes were operating on their efficiency plateaus. The plateaus of only a few counters were measured; most voltages were set with a source using the same technique as was used for the trigger counters. The responses of both tubes to a source at the centre of the counter were required to be equal. Under these conditions, the amplified (x10) signal from both tubes summed for minimum ionizing was found to be about 40 channels above pedestal in a LRS 2249A 10-bit ADC. There were approximately 10 photoelectrons in each counter.

The design of the fast logic for the calorimetry counters is exemplified by Fig. III.10, which shows the logic for counter no. 20. The signal from each tube is fanned out (as in the case of the trigger counter logic) to two non-attenuated outputs and one output attenuated by a factor of 6. The attenuated output was sent to a "super-low" ADC, while one non-attenuated signal was sent directly to a "low" (i.e. un-amplified) ADC channel. The ADCs are discussed in detail in (c) below.

Figure III.10: Fast logic for a sample calorimetry counter. The muon trigger is formed by using the S-bits together with the signals from the trigger counters (cf. p. 67).

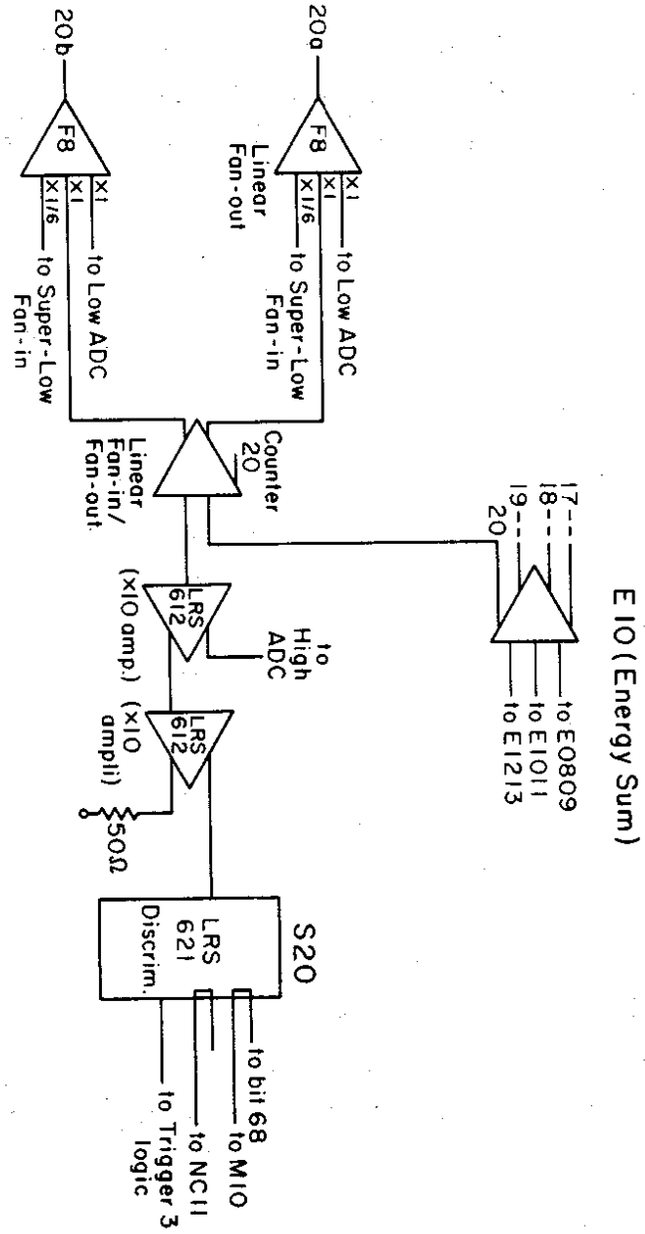

The remaining unattenuated signal was added to the signal from the other tube on the counter. The result was used to form an energy sum with 3 other counters to be used in forming event triggers. A second signal from the fan-in was amplified by a factor of 10 (to be sent to a "high" ADC), and by a factor of 100 (to be sent to a "S-bit" discriminator).

The gain of the calorimetry counters was monitored by light flasher system. Light from a spark gap[55] was transmitted via glass light fibres (typically 40 feet long) to each of the 56 calorimetry counters and to 2 reference phototubes (RCA 6342A). The rise time of the flasher pulse was 40 ns. An approximately even distribution of the light throughout a counter was obtained by directing the light onto a reflective white dot at the centre of the counter. All changes in the light output of the flasher system were monitored by the reference phototubes.

The drift in the gain of the reference tubes themselves was checked by monitoring their response during beam spills to an Americium γ-source embedded in NaI. The counting rate due to the source was small compared to the flasher, so that when the spark gap was fired there was a negligible probability for the overlap of a source and a flasher pulse. The pulse height of the photons from the source between beam

pulses were histogrammed using an LRS QVT pulse height analyser. The mean of this histogram was used to determine the variation in the gain of the reference tubes.

A more complete description of the Wonder Bldg. calorimetry may be found in Ref. 56.

(c) CAMAC Modules

The pulse height information from the calorimetry counters was read into the computer via four different types of CAMAC modules. These were referred to as bit modules, ADCs, TDCs, and scalers. The bit modules (EG&G C124) contained 24 latches which were switched on by logic levels from the fast electronics. Some latches were set when the pulse height from phototubes, or groups of phototubes, exceeded pre-set thresholds. Others were set when event triggers or components of triggers were fired. The LRS 2249A ADCs (Analog-to-Digital converters) digitised pulse height information from the calorimetry and trigger counters. The LRS 2228A TDCs (Time-to-Digital converters) recorded the timing of signals from all of the trigger

counter components, as well as selected calorimetry counters and the accelerator RF system. Scalers counted the number of times when selected counters, trigger components, and triggers fired during specified intervals. The bit modules, ADCs, and TDCs were enabled whenever any one of the six event triggers (cf. (d) below) or the pedestal, LED, or flasher triggers fired(cf. (f) below).

The size of the pulse height from the individual calorimetry counters was recorded by using LRS 2249A ADCs. The limited dynamic range (10 bits) of these devices necessitated the use of three signal levels: high, low, and super-low.

The high ADCs recorded the total output of a single counter (amplified by a factor of ten). These were needed to precisely record the value of the muon peaks. Typically the muon peak was in channel 40 (out of 1023 channels) above pedestal. Due to the amplification, these ADCs would saturate if the light equivalent of more than 5 GeV of hadronic energy was deposited in a counter. In order to allow accurate determination of the energy in hadron showers, which had energies of up to 240 GeV, the un-amplified signals from individual phototubes was sent into low ADCs.

In very energetic showers (E_{had} > 100 GeV), the low ADCs would saturate. For these events it was necessary to use the super-low ADCs. Signals from eight different phototubes (each attenuated by a factor of six) were summed and measured by a super-low ADC (cf. Table III.2). As there was a minimum of 28 inches of steel between counters in any given super-low, the probability of two low ADCs in the same super-low saturating was very small. This system also provided redundancy in retrieving the energy deposited in a counter when any single component of the ADC system saturated or failed.

Table III.2: Shown are the low ADC channels which make up each of the 14 superlow ADCs.

Superlow ADC No.	Low ADC No.							
1	1a	8a	15a	22a	29a	36a	43a	50a
2	1b	8b	15b	22b	29b	36b	43b	50b
3	2a	9a	16a	23a	30a	37a	44a	51a
4	2b	9b	16b	23b	30b	37b	44b	51b
5	3a	10a	17a	24a	31a	38a	45a	52a
6	3b	10b	17b	24b	31b	38b	45b	52b
7	4a	11a	18a	25a	32a	39a	46a	53a
8	4b	11b	18b	25b	32b	39b	46b	53b
9	5a	12a	19a	26a	33a	40a	47a	54a
10	5b	12b	19b	26b	33b	40b	47b	54b
11	6a	13a	20a	27a	34a	41a	48a	55a
12	6b	13b	20b	27b	34b	41b	48b	55b
13	7a	14a	21a	28a	35a	42a	49a	56a
14	7b	14b	21b	28b	35b	42b	49b	56b

Figure III.11: Shown is the logic governing the six event triggers. They are described on pp. 76-78 of the text.

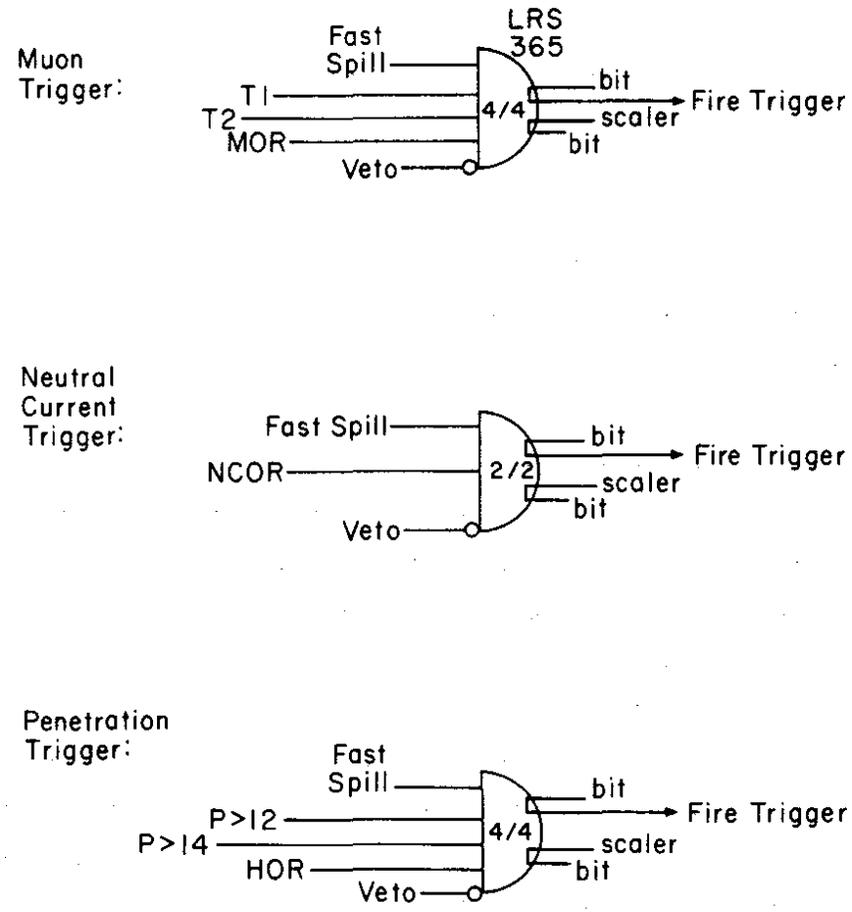

Figure III.11 (cont.):

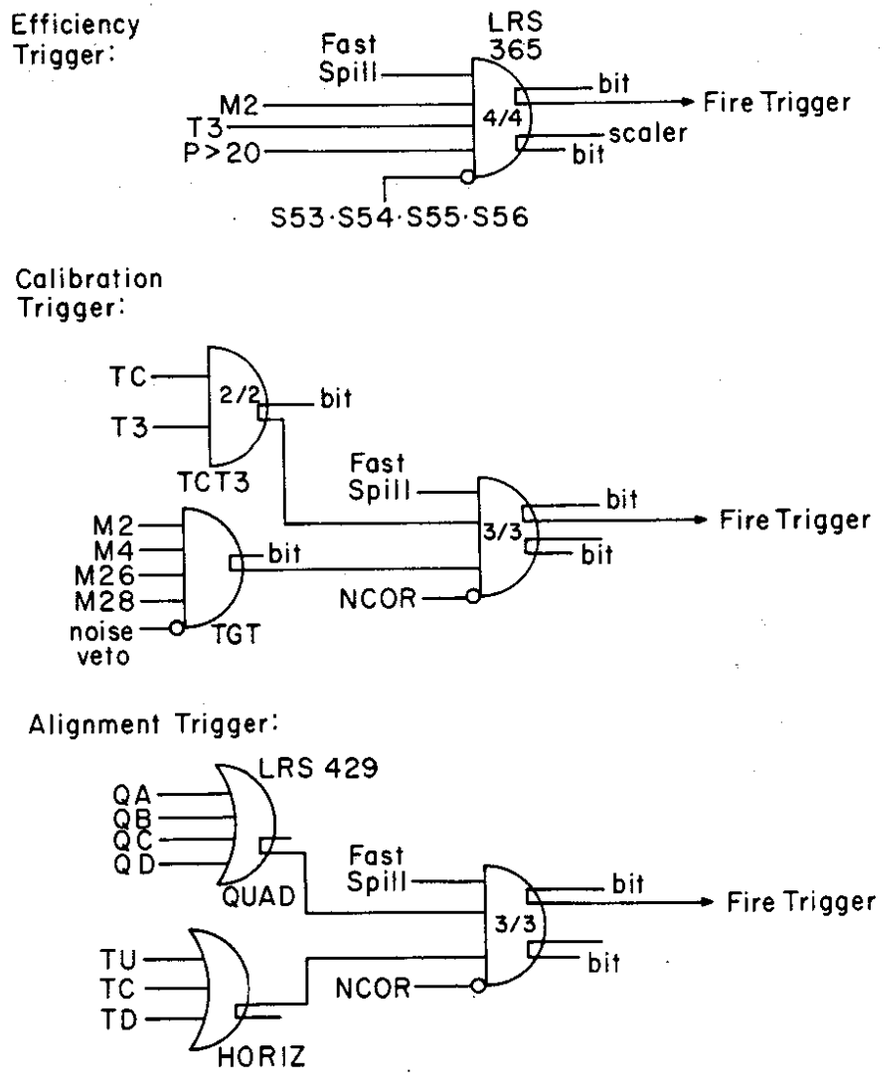

(d) Event Triggers

The logic signals which were generated by the trigger and calorimetry electronics described above were used to form six triggers. These were:

(1) Trigger 1, known as the "muon trigger". This trigger required at least one "M-bit" to fire in coincidence with trigger counters T1 and T2. Such a coincidence would be vetoed if it was in time with a signal in the veto counter. An M-bit was a majority logic condition requiring 2 counters in a group of 4 (e.g. nos. 21-24) to fire.

(2) Trigger 2, known as the "neutral current trigger". This trigger required that approximately 10 GeV or more of hadronic energy be deposited in the calorimeter in coincidence with 2 counters in a group of 4 firing, and that the veto counter not fire. The neutral current trigger was not used in the oscillation analysis.

(3) Trigger 3, known as the "penetration trigger". The penetration trigger fired if 14 or

more S-bits were set (corresponding to a μ penetration greater than 1.4 m of steel) in coincidence with approximately 5 GeV or more of hadronic energy deposited in the calorimeter. This trigger also rejected events with the veto counter firing.

(4) Trigger 4, known as the "efficiency trigger". The efficiency trigger required a coincidence between signals from trigger counter T3 and M-bit 2 (2 of the 4 most downstream calorimetry counters), in conjunction with at least 20 S-bits firing simultaneously. This trigger was vetoed if either S-bit 55 or S-bit 56 was set. The efficiency trigger had no component in common with the muon trigger. Moreover, its acceptance for charged-current neutrino interactions was smaller than that of the muon trigger. This ensured that whenever the efficiency trigger was satisfied, the muon trigger should have also fired.

(5) Trigger 5, known as the "calibration trigger", selected muons going through the centre of the detector for counter gain monitoring. This

trigger required signals from the centre components of counters T1 and T2 (i.e. T1C, T2CU, T2CD) in coincidence with counter T3 and M-bits 2,4,26 and 28 (i.e. the upstream and downstream ends of the calorimeter). The calibration trigger could be vetoed by the deposition of more than 20 GeV of hadron energy or by the noise veto (cf. (b) above). This was known as the "cosmic ray air shower veto".

(6) Trigger 6, known as the "alignment trigger". The alignment trigger required that the trigger components, "QUAD" and "HORIZ" (shown in Fig. III.12) fire in coincidence with the absence of a signal from the shower veto. This trigger selected muons passing through the trigger counters in a particular quadrant at a particular height. The calibration and alignment triggers were used for aligning the spark chambers in the target and toroid (cf. Chapter IV). The logic for these triggers is shown in Fig. III.11.

(e) Spark Chambers

The spark chambers which were used in the WB apparatus all measured 1.5-m x 3-m. There were 17 of these chambers in the target calorimeter, one after every 30-cm of steel. The 3-m x 3-m toroid chamber planes were formed by overlapping two 1.5-m x 3-m chambers. There were 4 such planes before the toroid and six behind the toroid.

Each chamber had two planes of strips (1 for x- and 1 for y-readout), 1.3 cm apart, mounted on Hexcel panels. The centres of adjacent strips were 1 mm apart. The spark chamber resolution of 0.5 mm was due to the strip spacing. A 90% He - 10% Ne gas mixture was continuously circulated through the chambers and a liquid N_2 purification system. About 1% by volume of alcohol was added to this mixture. When a charged particle passed through the gap between planes, the gas was ionized. If the spark chambers were then triggered, one of the planes would be pulsed to high voltage. Current then flowed across the gas where the resistence was least, that is, where the charged particle had ionized the gas.

Current was thus generated in the strips nearest to

the ionization. This current in turn induced an acoustic pulse in a magneto-restrictive wire which ran across one end of the strip. This pulse propagated to the end of the "wand" at the speed of sound (about 5mm/μs), passing through a pick-up coil which generated an electric pulse due to the induced magnetic field. The position of a spark along the wand was known because fiducial pulses were generated at surveyed points on both ends of the wands. The relative timing of the spark with respect to these fiducials was used to obtain the position of the charged particles (cf. Chapter IV). The timings were measured by a 20 MHz clock. Up to 16 sparks per event could be recorded.

The spark chambers were the major source of deadtime in the detector; 6 ms were required for the high voltage to re-charge. This limited the detector to one event per 1 or 2 ms spill. This feature of the apparatus made it preferable to receive 6 spills per 1 s accelerator cycle (each about 1 ms long) rather than receive all of the beam in one burst.

(f) Toroidal Magnet

The momentum analysing magnet in the Wonder Bldg. was a solid iron toroid with a 25.4 cm diameter central hole for the power coils. The outer radius of the toroid was 1.5 m, and the magnet was 2.4 m long.

The mean field in the toroid was 17.5 kG, giving a p_t kick of 1.2 GeV/c. The magnetic field was measured with a Hall probe at different radii and distances in a 1.5 cm gap between the top and bottom halves of the magnet. The results of these measurements were then modelled using the POISSON[57] computer program.

(g) On-line Software

Information from the detector was analysed on-line and written to magnetic tape by the PDP-11. Computer displayed events were displayed incessantly so that the physicist on shift could spot failures in the apparatus or electronics. Information from the ADCs and bits was also studied periodically.

Seven types of records were written to tape. They

were the event records (1 record for each event in the spill), the flasher record, the LED record, the NaI record, the pedestal record, the scaler record, and the monitor record. All but the event records were written once per accelerator cycle.

The data from an event trigger was written to tape in an "event record". Event records contained the current run number, cycle number (number of accelerator pulses processed during the current run), pulse number (accelerator pulse number as transmitted by the main control room), and the time at which the event occurred. This information was used in combining data from the two detectors. The bits which were set by the various counters, trigger components, and triggers were written in 18 16-bit words. The pulse height information from the ADCs was written in 240 words. The "event scalers" (i.e. scalers which were reset for each event) were packed into 16 words, and the TDC data was packed into 40 words. Finally, the spark times were stored in a 400 element array, while an 84 word array (one word per wand) contained the spark pointers and error flags.

Event records were written both after beam spills and after a 30-ms long "cosmic ray gate". Data taken after the cosmic ray gate was used to determine the negligible

background in the charged-current data sample due to cosmic rays satisfying the neutrino interaction triggers.

The light flasher system and the LED system were each fired once per spill. The pulse height information obtained during these gates was read in and written to tape. The ADCs and TDCs were also gated open by a "pedestal trigger" between spills. The pulse height which was recorded during this gate was written to tape and was used in analysing the ADC data. The reference phototubes viewing the NaI source were read out once between spills. Finally, the detector scalers and the beam-line monitors were read out once per spill and stored in their own records on tape.

Section III.1.2: The Lab E Detector

The Lab E detector was similar in design to the Wonder Bldg. apparatus, consisting of an iron target calorimeter and toroidal muon spectrometer (cf. Figs. III.12,13). The calorimeter was composed of 650 metric tons of 3.05 m x 3.05 m steel plates, 82 3.05 m x 3.05 m liquid scintillation counters, and 24 3.05 m x 3.05 m spark chambers. In contrast to the previous configuration of this detector,[1,4] only the four downstream carts (cf. Fig. III.12) were used. Thus the active part of the calorimeter was made up of 444 metric tons of steel and 56 liquid scintillation counters. The 12 spark chambers from the upstream two carts were moved to the toroidal spectrometer.

Figure III.12: Shown is a side view of the Lab E detector. The positions of the various trigger counters are indicated.

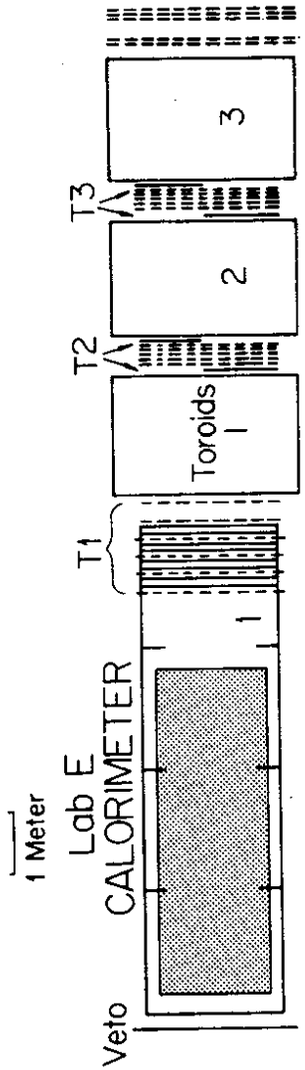

Figure III.13: The Lab E detector is shown, together with detailed drawings of one of the six target carts and one of the three iron toroidal magnets.

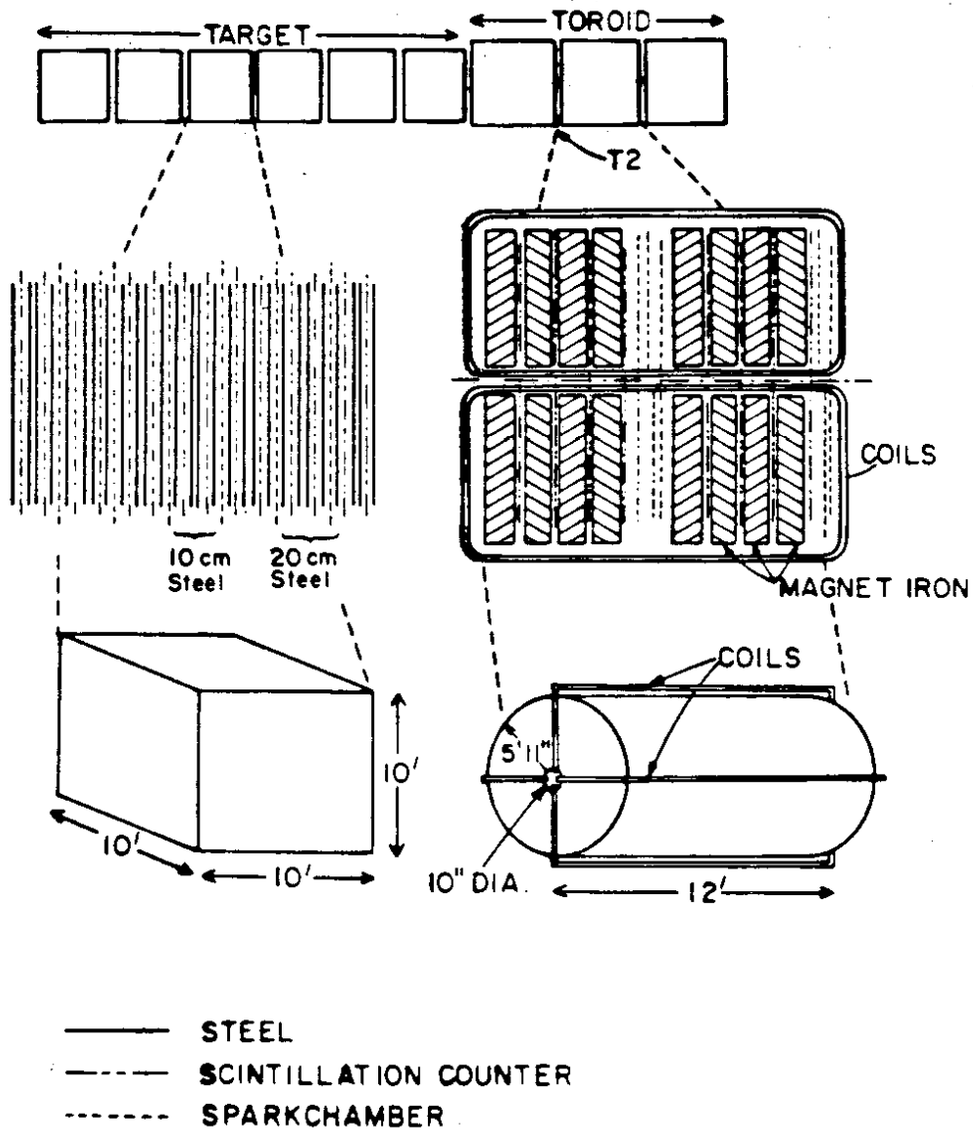

The toroidal magnet has been described previously.[45] It was made up of 3 components, each 3.5 m in diameter and 1.7 m in length. The p_t kick of the 3-magnet system was 2.4 GeV/c, and the average value of B was 17 kG. There was a 25.4 cm diameter coil at the centre of the toroid for the power coil. Unlike during previous runs of the detector, the gaps in the centre of each component were not instrumented with spark chambers. There were four 3.05 x 3.05 m spark chambers behind each toroid component. The 1.5 m x 3.0 m spark chambers in the Wonder Bldg. had previously been used in the Lab E spectrometer.

Trigger counters T1, T2, and T3 were unchanged from previous experiments, being 3 m x 3 m planes of plastic scintillators. Their locations are indicated on Fig. III.12. Counter T4 was removed to the Wonder Bldg. and modified to become that detector's Veto counter. The Lab E Veto counter was augmented by a "cart veto", which consisted of the 6 counters directly upstream of the active target (nos. 57 to 62).

There were 5 event triggers in Lab E, corresponding to Triggers 1-4 and 6 in the Wonder Bldg. Details of these triggers have been given elsewhere.[46,47] The muon trigger (Trigger 1) was similar to the Wonder Bldg. muon trigger (cf. p. 74) and is shown in Fig. III.14.

Figure III.14: Shown is the fast logic for the Muon Trigger (Trigger 1) in Lab E.

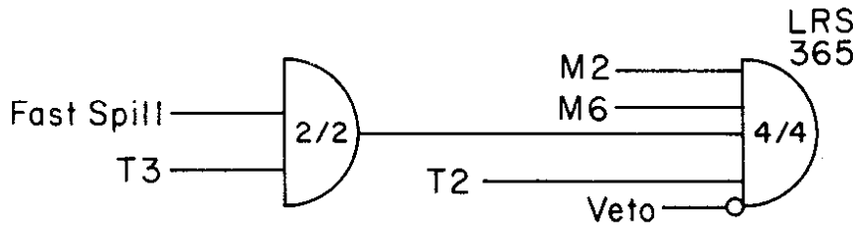

The on-line data-taking system was very similar to that in the Wonder Bldg. (in fact, the Wonder Bldg. system was copied from the Lab E system). The structure of the data records was the same, although the beamline monitors which were read out at the two locations were mostly different. This allowed more monitors to be recorded, since each detector could only read in a limited number.

A comparison of the two detectors is given in Table III.3.

Table III.3: The properties of the two neutrino detectors are compared below.

	LE	WB	UNITS
TARGET CALORIMETER			
Mean distance to decay pipe	1116	715	m
Steel, absolute:			
length	5.7	5.7	m
breadth	3 x 3	1.5 x 1.5	m
mass	444	108	metric ton
Steel, fiducial:			
length	3.8	3.8	m
breadth	2 x 2	1.3 x 1.3	m
mass	116	48	metric ton
Steel per counter	10.2	10.2	cm
Steel per chamber	20.3	30.5	cm
Hadron energy $\sigma(E)/E$	$0.9/\sqrt{E}$	$0.9/\sqrt{E}$	GeV
MAGNET SYSTEM			
Toriod:			
length	4.8	2.4	m
outer radius	1.8	1.5	m
inner radius	12.7	12.7	cm
field	17.5	17.5	kG
p_t kick	2.4	1.2	GeV/c

Section III.2.1: The Beam

The dichromatic ("narrow band") neutrino beam was obtained as follows. The Fermilab Main Ring delivered between 1 and 2 x 10^{13} protons to a BeO target each accelerator cycle. In general, this was done for five "pings" (about 0.5 ms duration) and one "fast spill" (1-2 ms). These pulses were separated from each other by 100-200 ms. The design of the neutrino beam has been extensively discussed elsewhere.[58,60]

A "train" of focussing and bending magnets was located behind the production target. These magnets served to select secondary particles with a given momentum and charge. Data were taken at 6 "train settings" (sets of magnet currents): +100 GeV, +140 GeV, +165 GeV, +200 GeV, +250 GeV, and -165 GeV. Positive (negative) train settings selected positive (negative) particles. The number of protons delivered at each train setting during the detector livetimes for the oscillation data sample are shown in Table III.4.

Table III.4: Number of protons delivered during the periods when both detector were operating without problems (gated on the detector livetimes).

Train Setting	Lab E Live	Wonder Bldg. Live
+100 GeV/c	3.46 x 10^{17}	3.66 x 10^{17}
+140 GeV/c	4.57 x 10^{17}	4.75 x 10^{17}
+165 GeV/c	3.53 x 10^{17}	4.09 x 10^{17}
+200 GeV/c	5.09 x 10^{17}	5.43 x 10^{17}
+250 GeV/c	5.64 x 10^{17}	5.97 x 10^{17}
-165 GeV/c	14.03 x 10^{17}	15.55 x 10^{17}

Table III.5: Number of protons delivered during each detector's livetime, after the further requirements of correctly merged monitor records and good beam steering. These are the totals which were used for livetime corrections.

Train Setting	Lab E Live	Wonder Bldg. Live
+100 GeV/c	3.27 x 10^{17}	3.49 x 10^{17}
+140 GeV/c	4.02 x 10^{17}	4.03 x 10^{17}
+165 GeV/c	3.09 x 10^{17}	3.54 x 10^{17}
+200 GeV/c	4.45 x 10^{17}	4.74 x 10^{17}
+250 GeV/c	4.84 x 10^{17}	5.12 x 10^{17}
-165 GeV/c	11.35 x 10^{17}	12.25 x 10^{17}

The dichromatic train is shown in Fig. III.15. The train transports the beam to a 352 m long evacuated pipe (80 cm in diameter). The rms momentum spread (σ_p/p) of the emerging beam is ± 11 %. Beam monitors are placed in the decay pipe (cf. Fig. III.16). The monitors which were used in the oscillation analysis were: (a) the Neuhall toroid, (b) secondary beam profile monitors at the Target Manhole and the Expansion Port, (c) split-plate ion chambers at the Target Manhole and the Expansion Port, and (d) muon profile monitors placed behind a hadron beam dump at the end of the decay pipe.[59]

Figure III.15: Shown is the N0 "train". The train was a series of bending and focussing magnets which selected particles of a particle charge and momentum to form a secondary hadron beam entering the decay pipe.

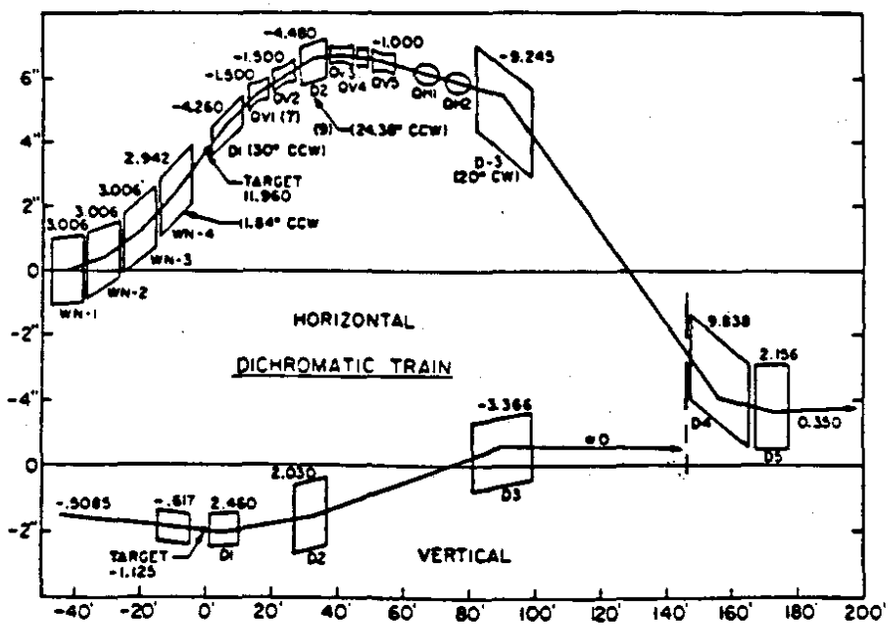

Figure III.16: The lay-out of the Fermilab neutrino beam-line is shown below. The locations of the monitoring stations in the decay pipe, as well as the neutrino detectors, are indicated.

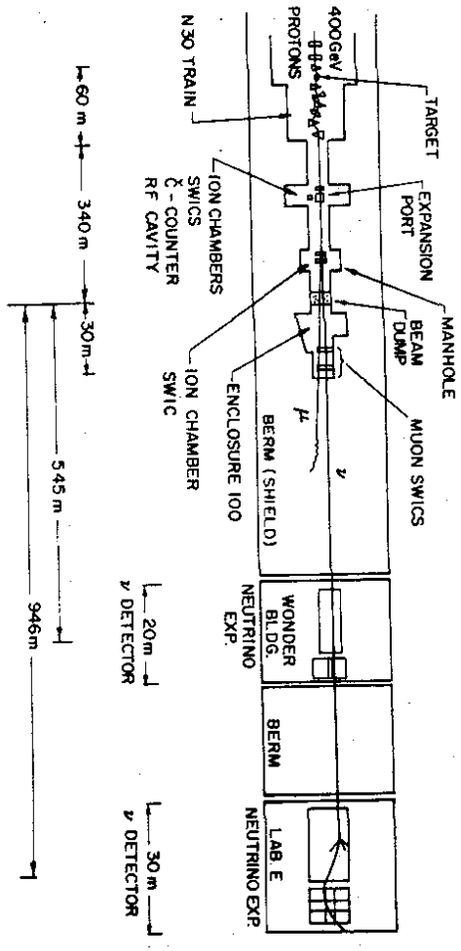

The Neuhall toroid (NT) was a beam-current transformer placed in front of the BeO target. It was used to determine the number of protons delivered to the target. The signal from this device was sent to scalers which were gated on four logic pulses: S(spill), which bracketed the entire pulse; B(beam), which turned on whenever 10^{11} of instantaneous rate was exceeded and turned off when the rate dropped below that level; E (Lab E), which turned on with B and turned off when the Lab E detector was triggered; and W (Wonder Bldg.), which turned on with B and E and turned off when the Wonder Bldg. detector fired. Gate B was also used to turn the two detectors on at the beginning of a neutrino beam spill. The principle live-time monitor was NT. The number of protons delivered for each train setting during each gate are given in Tables III.4 and 5.

Two decay pipe beam profile monitors were used in the oscillation analysis. One, a segmented wire ion chamber (SWIC) was located in the Target Manhole. The second monitor, known as the "XT-SWIC", was located in the Expansion Port. This device used copper strips, rather than wires, to collect the ionization. Sample profiles from a single beam pulse from these devices are shown in Fig. III.17. The data from these monitors was used to obtain information about the angular divergence of the

beam, and to test the predictions of the Monte Carlo beam simulations.

Figure III.17: Beam profiles from the XT SWIC, taken at the +165 GeV/c momentum setting.

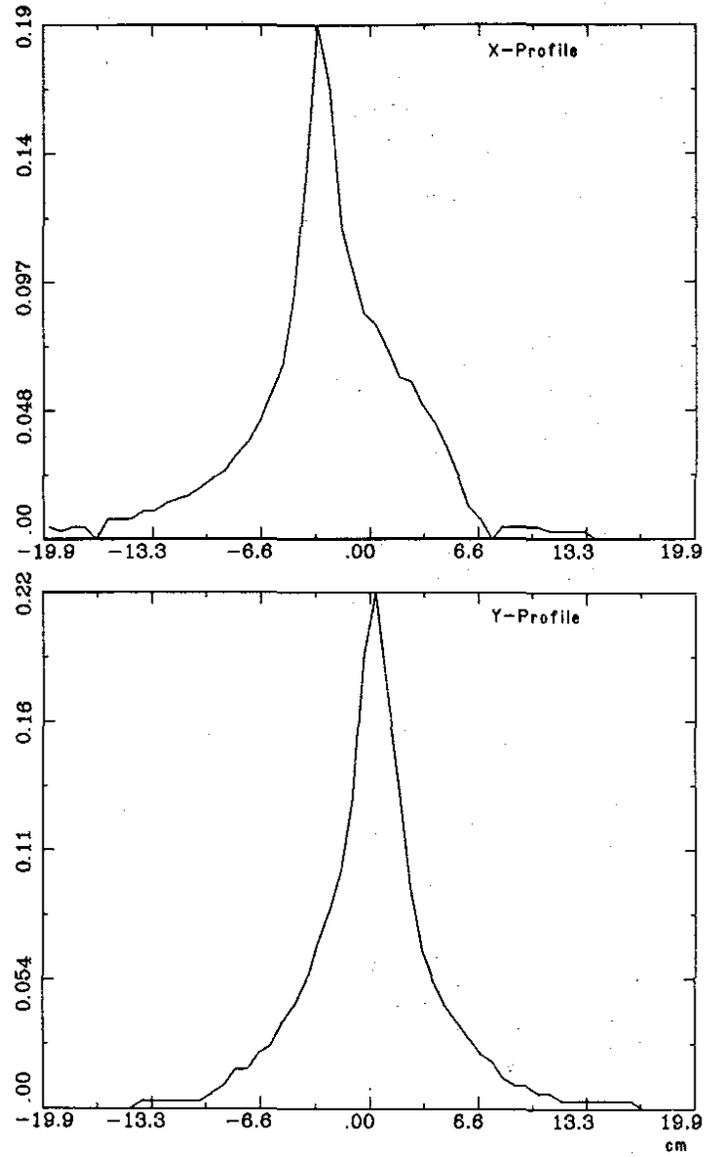

The split plate ion chambers were used both to monitor the steering of the beam on-line, and to reject pulses with bad steering in the off-line analysis. These devices contained two plates, one split horizontally and the other split vertically. The relative fraction of the beam-induced ionization collected by the two halves of a plate was very sensitive to where the beam passed through the ion chamber. The quantity:

$$\frac{Q_1 - Q_2}{Q_1 + Q_2}$$

was used to parametrize the steering, where Q_1 and Q_2 were the amounts of charge collected on each of the plates. Plots of this variable for each of the four devices (top-bottom and east-west in MH, and top-bottom and left-right in the Expansion Port) are shown in Fig. III.18. The cuts at 0.1 on either side of the mean correspond to a shift in the beam centre of less than 3 cm at Lab E.

Figure III.18: Shown are plots of the beam steering in x- and y-views at the Expansion Port and Target Manhole beam monitoring stations.

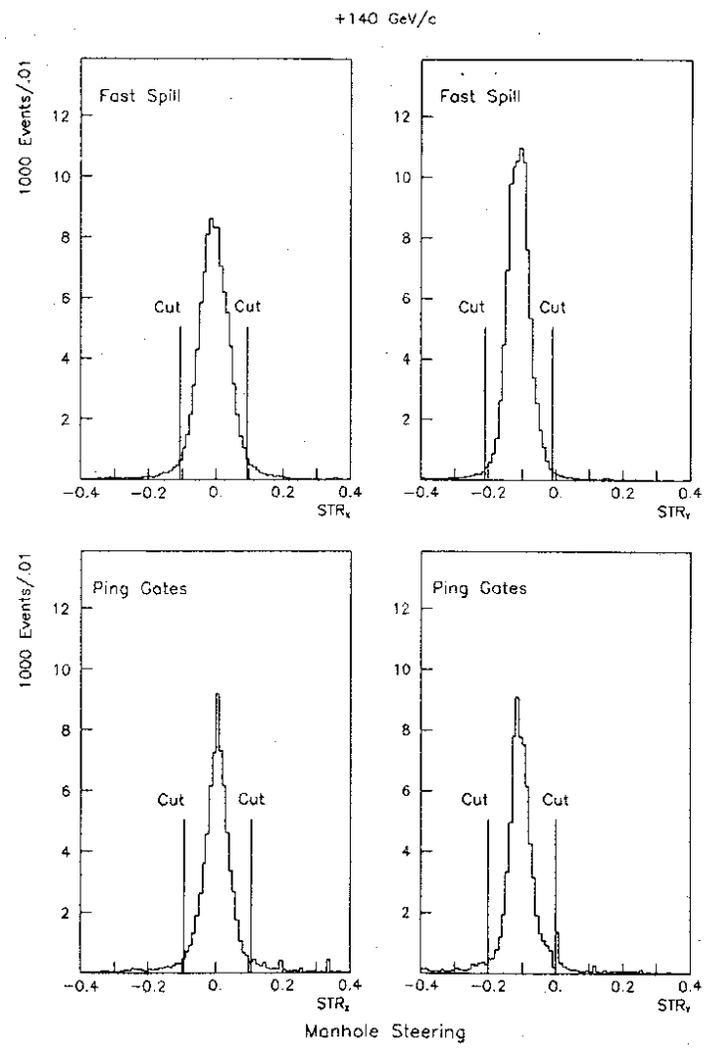

Muon SWICs (similar in construction to the XT-SWIC) were placed downstream of the beam dump (cf. Fig. III.16). Most particles which penetrated the dump were muons from the decay of mesons in the decay pipe. The profiles of these muons were used (in combination with the decay pipe profile monitors) to study the angular divergence of the beam.[60]

A hole collimator, measuring 1.2 cm x 1.2 cm transversely and 1.8 m in length, was placed at the end of the train for part of the data-taking. This collimator was moved across the beam so that the profiles due to each segment could be measured. This information was used to obtain the angular distributions of the beam.

Section III.2.2: The Beam Simulations

As the results of this experiment were based on the comparison of event rates at the Lab E and Wonder Bldg. detectors, it was important to understand what the relative behaviour of these event rates was expected to be. To this end, we used a simulation of the secondary hadron beam to study both the shape of the beam (as measured by the SWICs mentioned above), and the expected distributions of neutrino events in the detectors. The latter point will be discussed below (cf. Ch. V).

The dichromatic train was simulated using the beam transport program, "TURTLE".[61] Three sets of information external to TURTLE were required for this simulation. These were a spectrum of secondary particles, the locations of the magnets in the train, and the currents in the magnets. The particle spectrum was obtained by using a parametrization extracted from the data of Ref. 62, which reported a measurement of the production of hadrons off of a BeO target at CERN. The locations of magnets and other beam-line components, such as inserts and collimators, were measured by surveyers. The operating currents of the train magnets were directly measured. The magnetic fields were then calculated using these currents. These calculations have been tested by measurements of magnets used in the Fermilab accelerator.

The above information was used to generate a simulated beam. The particle production parametrization was used to generate secondary pions, kaons, and protons with the correct distributions in energy, angle, etc. This was done assuming a 400 GeV proton beam incident on a 30 cm-long BeO target. Those generated particles which entered the train's magnetic channel were transported through the train to the decay pipe entrance. Those particles whose paths intersected obstacles were not allowed to propagate any further.

It should be noted that this simulation of the beam was not expected to be perfect. No attempt was made to include the effects of the fringe fields of the magnets. All obstacles in the train were assumed to be infinitely deep; i.e. if a particle hit an obstacle, it was no longer propagated through the train. This ignored the possibility of the particle scattering back into the magnetic channel. Finally, no attempt was made to "fine-tune" the positions or currents of the magnets.

There were two ways to check this simulation. These were by comparing the predicted positions at the monitoring locations with the measurements, and by comparing the predicted angular divergence with the information obtained from the hole-collimator studies. The predicted beam profiles are shown in Fig. III.19 for the +165 GeV train setting. These are obtained by propagating the beam, delivered by TURTLE to the decay pipe, along a straight line to the positions of the two SWICs.

Figure III.19: Shown are the beam profiles at the XT-SWIC in the Expansion Port as predicted by the TURTLE beam Monte Carlo.

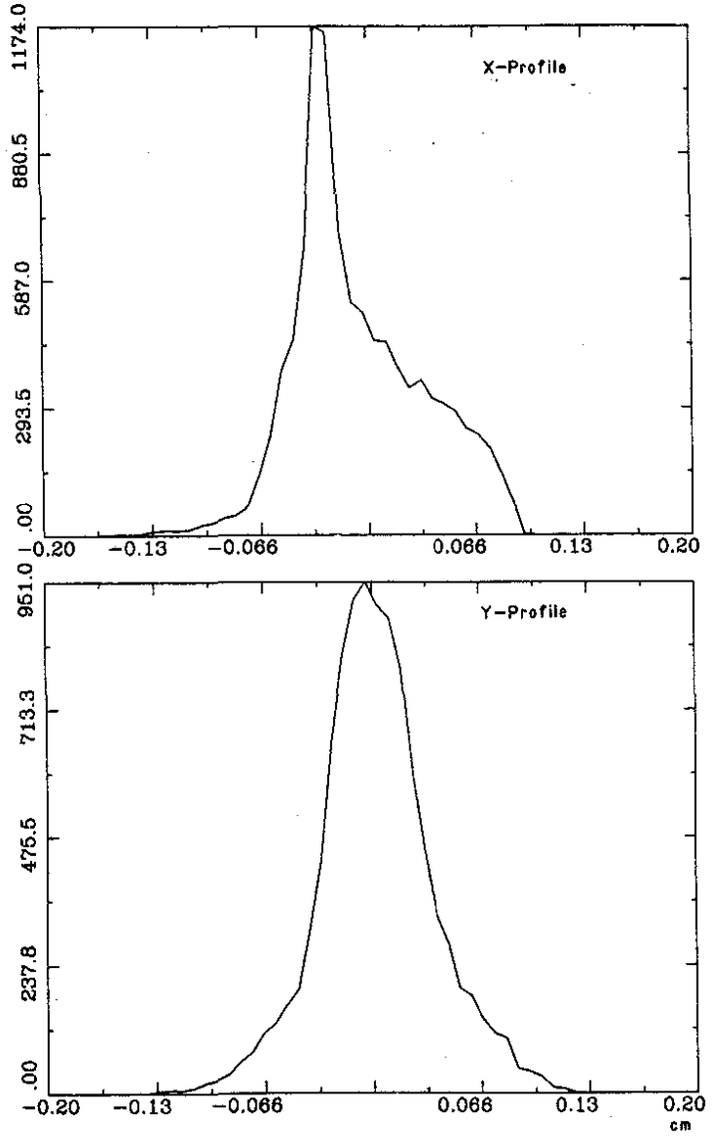

Figure III.20: The angular distributions (in θ_x and θ_y) obtained from the analysis of the hole-collimator data (cf. Ref. 60) is shown.

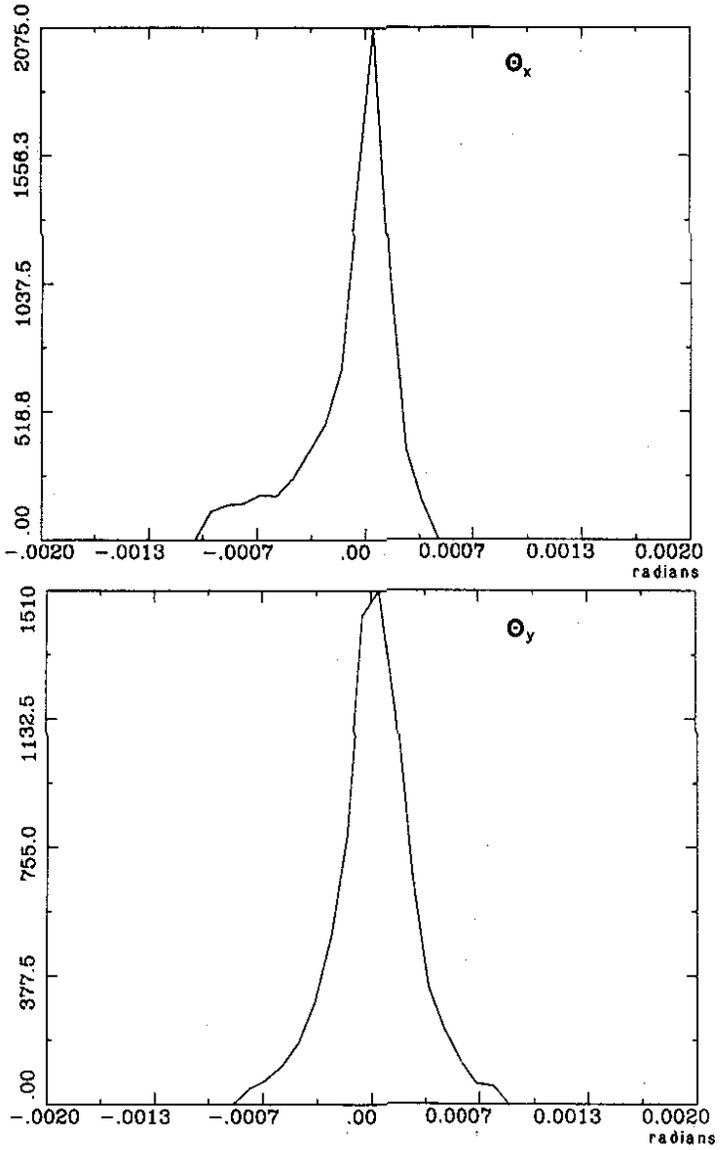

Figure III.21: Shown are the angular distributions (in θ_x and θ_y) predicted by the TURTLE beam Monte Carlo.

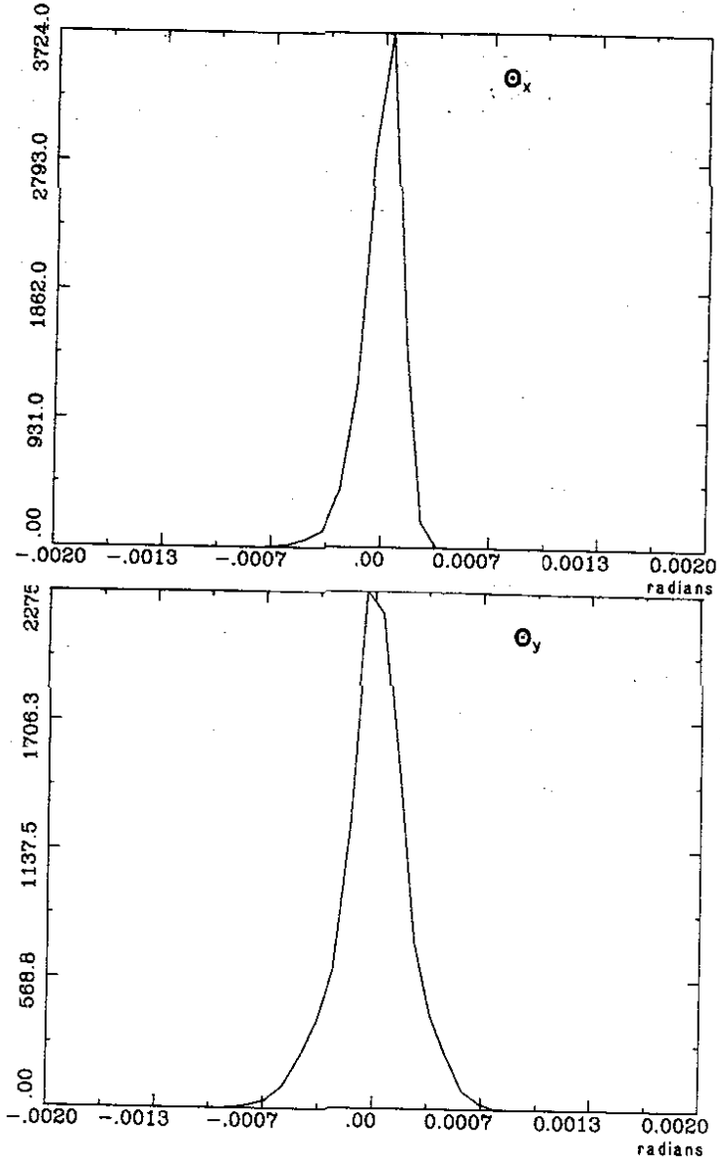

The predicted angular distributions and the results of the analysis of the hole-collimator data are shown in Figs. III.20 and 21. That analysis, which used the known hole-collimator positions and the measured XT SWIC profiles for those positions to obtain angular distributions, is described in Ref. 60.

The comparisons with the data indicated that the beam was well-understood. However, there was a small (and not unexpected) discrepancy between the data and the simulation. The systematic effects of that discrepancy were assessed by using what was called an "ad hoc" beam simulation. The ad hoc simulation was constructed to match the observed profiles, regardless of and independent of any physical considerations. The results of this simulation are shown in Figs. III.22 and 23.

Figure III.22: Shown are the SWIC profiles predicted by the Ad Hoc simulation of the secondary beam.

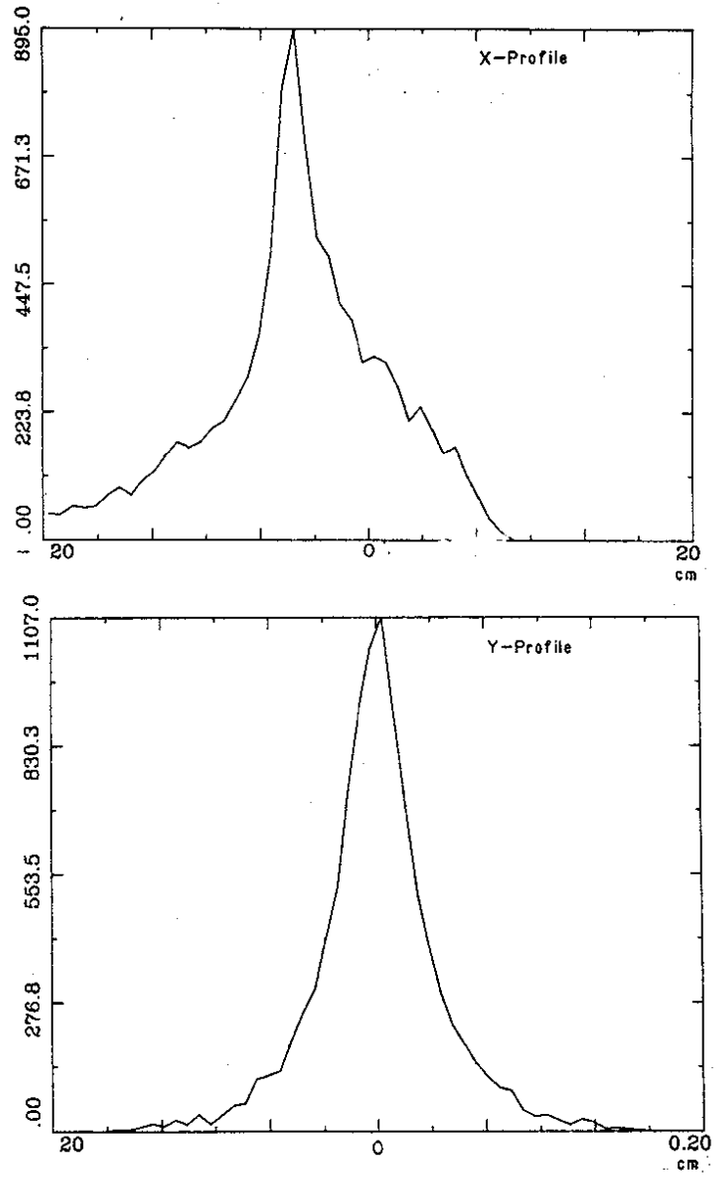

Figure III.23: Shown are the angular distributions predicted by the Ad Hoc simulation of the secondary beam.

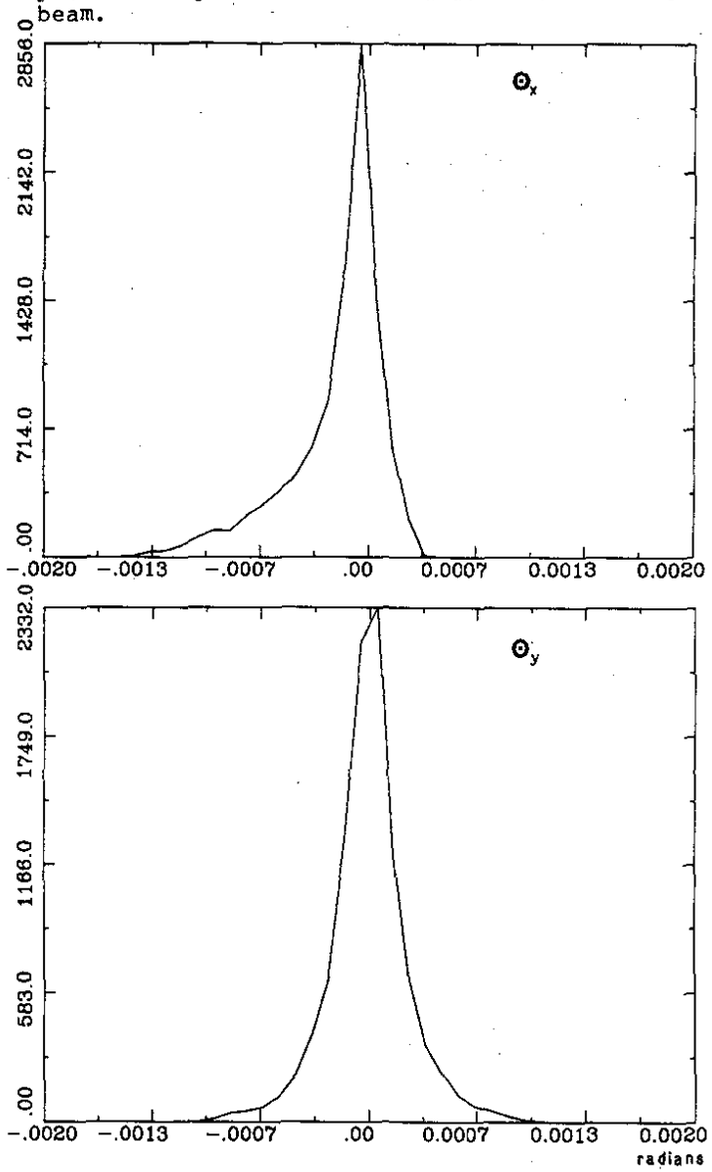

The secondary hadron beams which were generated by these two models were used to generate neutrino beams. The pions and kaons from each beam were allowed to decay as they traversed the decay pipe, and the neutrinos thus created were used to generate events in the two detectors. (This later step is described in Ch. V).

Scatter plots of the generated energy versus the radius for events at the Lab E detector for the six beam settings are shown in Fig. III.24. These use neutrinos (from the TURTLE beam Monte Carlo) passing through the Lab E detector. The correlation of the two quantities, which will be used in the later analysis, is clearly visible. It should be remarked that the neutrinos from pion decay (ν_π) are much more sensitive to the angular divergence of the secondary beam than are those resulting from kaon decay (ν_k). This is because the mean decay angle, $\langle\theta\rangle_x$, of the ν_π is approximately 0.35 mrad for 250 GeV/c parent particles, which is similar to the divergence, $\Delta\theta_x$, of about 0.20 mrad. The decay angle of the ν_k is much larger than the divergence, being 0.6 mr.

Figure III.24: Shown are scatter plots of the energy and radius of the neutrino events generated using the TURTLE beam Monte Carlo. No detector resolutions have been taken into account in these events.

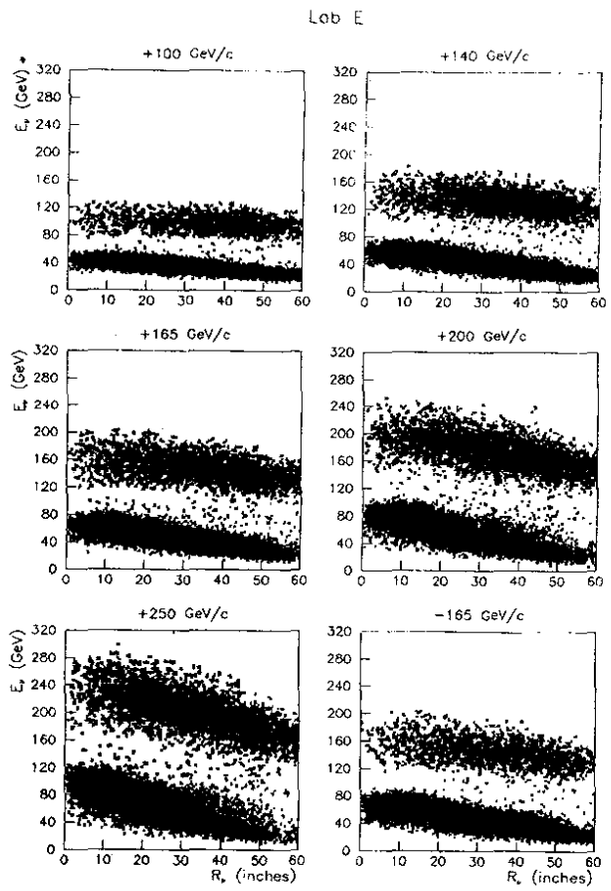

CHAPTER IV

Neutrino Event Reconstruction

Section IV.1: Determination of Muon Momentum

Th path of a muon in a charged current event was measured using the position information from the spark chambers. The bend in the particle trajectory induced by the iron toroidal magnet was obtained by comparing the tracks in front of and behind the magnets. This was done in four steps: (a) the spark times recorded on the data tapes were translated into positions with respect to surveyed fiducial marks on the chambers; (b) the relative positions of the spark chambers and the analysing magnets were determined first by surveying and then by an alignment process using measured muon tracks; (c) tracks were fit to sparks in front of and behind the magnet (in both x- and y-views); and (d) the muon momentum (p_μ) was determined

using the fit track parameters and the knowledge of the magnetic field in the toroid.

Section IV.1.1: Wonder Bldg.

The spark times were converted into positions by using the times of the "fiducials". The fiducials were pulses generated by small coils located at known positions on either end of a spark chamber wand. The timings of the fiducials were constantly updated because of fluctuations induced by the varying temperature in the detector building. These updated times (t_{fid1} and t_{fid2}), together with their known fixed positions (x_{fid1} and x_{fid2}) were used to obtain the position of the spark (x_{skp}) with the equation:

$$x_{spk} = (t_{spk} - t_{fid1}) \left(\frac{x_{fid2} - x_{fid1}}{t_{fid2} - t_{fid1}} \right)$$

where t_{spk} is the spark time recorded on the data tape. In case of an inefficiency in recording a fiducial for a particular event, the running average of that fiducial was used. Fiducial inefficiencies were typically 0.1 %.

The accurate alignment of the spark chambers and toroidal magnet (point (b) above) was a crucial factor in determining p_μ. The alignment was obtained iteratively, using the surveyed locations of the magnet and spark

chambers as a starting point. There were two survey points on the top of a 5′ x 10′ spark chamber, one at either end of the 10′ span. The co-ordinates in x, y, and z of two chambers were obtained with respect to a fixed point in the floor of the detector building; the co-ordinates of all other chambers were found with respect to these two chambers. From the two survey points on a chamber it was possible to find the angle of rotation in the plane of the chamber. All chambers were mounted so that there was no rotation out of the vertical plane.

The survey measurements were the initial values for an iterative alignment process. The front chambers were aligned first, followed by those behind the toroid. Finally the front and back groups were aligned with respect to each other. Using the fitted tracks (the calculation of which are described below), "residuals" were calculated for each spark on the track. The residual for spark number k is defined as:

$$R_k = \frac{x^k_{spk} - x^k_{fit}}{\sigma_k}$$

where x^k_{spk} is the position of the spark determined from the data, x^k_{fit} is the location of the fit in that chamber, and σ_k is the measurement error. The latter variable incorporated both the intrinsic resolution of the spark

chamber and the multiple scattering of the muon in steel. Each iteration processed approximately 500 events; the position of the fiducials was changed from one iteration to the next to minimize the residuals for each wand. The fiducials of the two reference chambers were never adjusted. The fiducials were required to converge to within .001"; this typically occurred after 3 iterations.

The procedure for aligning the back chambers was identical to that for the front chambers. When that process was finished, it was necessary to obtain the relative alignment of the two sets of chambers. This was done in two steps. The first step used those events which passed through the corners of the spark chambers and outside of the magnet steel. Using the survey measurements as a starting point, an iterative procedure similar to that described above was used to obtain the relative positions of the two sets of chambers.

Unfortunately, the procedure described above was not very powerful due to the small number of events in the corners of the detector. It was thus necessary to use momentum analysable muons which passed through the toroid. The left and right halves of the rear spark chamber planes (recall that these were made up of two 5′ x 10′ chambers each) were aligned separately.

Straight-line fits obtained for the muon trajectory were calculated using a simple procedure. All possible combinations of sparks were fit to a straight line, the only constraint being that a maximum of one spark per chamber was used in the fit. If any spark was more than 0.7" away from the fit, it was rejected and the calculation was redone. Fits were calculated using the least squares technique. Weights were calculated for each spark which included the effects of the intrinsic resolution of the spark chamber (0.5 mm) and the effects of the multiple scattering in steel. The weight was given by:

$$Wt_{spk} = \frac{1}{(.04")^2 + \alpha (z_{Fe})^3} \qquad (2)$$

where z_{Fe} is the distance in steel between the toroid and the spark in question, and α is given by:

$$\alpha = 0.197 \left(\frac{.015}{p_{\mu\,(GeV)}} \right)^2 \qquad (3)$$

It is important to note the dependence of α on p_μ. This was an important problem in the momentum reconstruction, as it introduced a correlation between p_μ and the error matrix. The weights were calculated in terms of the steel between the toroid and the chamber because the momentum reconstruction calculation demanded an accurate measurement of the trajectory going into the toroid. For other purposes

(e.g. structure function analysis[47,48,49]), it would have been preferable to calculate the weights in terms of the steel between the chamber and the event vertex.

The procedure given above was followed for both the back and the front tracks. The fit variables were the slope and intercept of the muon at the faces of the toroid. These fit variables were then used in the momentum fit. The particular tracks to be used in the momentum fit (recall that all possible combinations were tried) were chosen to be those fits in each view (front and back; x- and y-) with the most sparks. If two fits had the same numbers of sparks, the one with the smallest residuals was chosen. These selection criteria were checked by scanning a sample of events; they were found to consistently select the best possible track. The only problem with this procedure was that, in the absence of a good track, a bad track would be found. Such tracks were typically made up of noise sparks. The result of choosing such a track invariably was that p_μ would fail to be reconstructed.

The parameters of the fits to the front and back tracks were used to calculate the value of p_μ via an iterative procedure. The first guess of the muon momentum was obtained by extrapolating both views of each fit track to the centre of the toroid and deducing p_μ from the locations

of the fits and the slopes. The non-uniformity of the magnetic field and the effects of multiple scattering and dE/dx energy loss were neglected in making this approximation. The formula used for this guess is given in Appendix A.

The iteration used the guessed value of p_μ and the measured slope and intercept of the muon trajectory at the fron face of the toroid. The muon was propagated through the magnet, with dE/dx losses, multiple scattering effects, and the bend due to the magnetic field applied at the centre of each of the 11 slabs which constituted the toroid. The magnetic field was determined by using the subroutine derived from the Hall probe measurements described in Chapter III (cf. p. 81 above).

The track resulting from this procedure was compared to the measured back track by calculating the χ^2 function:

$$\chi^2 = \Delta^T \varepsilon^{-1} \Delta \tag{4}$$

Here, ε is the error matrix and Δ is a four element vector consisting of the differences between the measured and predicted values of the back track fit parameters. The elements of Δ are Δx, Δs_x, Δy, and Δs_y, which are given by:

$$\Delta x = x_{pred} - x_{fit} \tag{5a}$$

$$\Delta s_x = slope^x_{pred} - slope^x_{fit} \tag{5b}$$

$$\Delta y = y_{pred} - y_{fit} \tag{5c}$$

$$\Delta s_y = \text{slope}^y_{pred} - \text{slope}^y_{fit} \tag{5d}$$

The error matrix, ε, is a convolution of the error matrices resulting from the least squares fits to the front and back tracks, as well as the errors introduced by the multiple scattering. The exact form of ε is given in Appendix A, but a few comments will be made regarding the effect of the multiple scattering on the fitting procedure below.

After a χ^2 is calculated for the initial guessed momentum, the momentum is changed by a small amount (typically 10 % of p_μ) and the χ^2 is re-calculated. If the χ^2 decreases, then the new value of p_μ is adopted as the best guess and another iteration is done. If the χ^2 increases, then the momentum is changed in the opposite direction. The χ^2 space is thus mapped out and the muon momentum which gives the smallest χ^2 is taken to be the best value.

The presence of multiple scattering caused problems with this procedure. The contribution of the multiple scattering to the error matrix is dependent on the inverse of p_μ; that is, as the momentum gets smaller the error gets

larger. This is illustrated by the equation for the error on the angle[63]:

$$\langle\theta^2\rangle_{MS} \simeq \frac{.015\ L_{Fe}}{p^2 L_{rad}} \tag{6}$$

where L_{Fe} is the distance in steel traversed by the muon, and L_{rad} is the radiation length is steel. It is possible that if a muon is propagated through the toroid with several different momenta, and the error matrix is separately calculated for each momentum, that the smaller values of p_μ might have a smaller value of χ^2 due to the larger error.

The bias toward lower muon momenta which was introduced by the multiple scattering terms in the error matrix was minimized by <u>not</u> recalculating the error matrix on each iteration of the muon momentum. Rather, p_μ was required to change by a factor of two before ε would be recalculated. In addition, ε was never recalculated if p_μ has dropped below 10 GeV/c.

The distributions of momenta resulting from this calculation are shown in Fig. IV.1 for each train setting.

Figure IV.1: Shown are the muon momentum (p_μ) distributions for the Wonder Bldg. detector at each of the six secondary momentum settings.

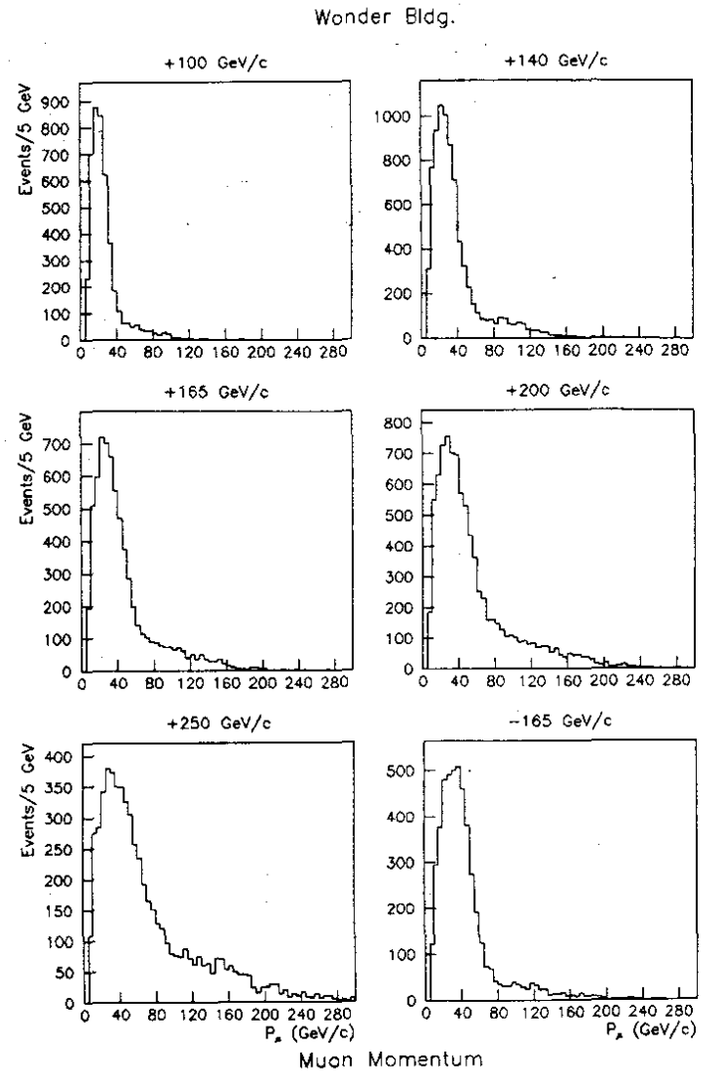

Section IV.1.2: Lab E

The method of reconstructing the muon momentum in Lab E has been described in detail elsewhere[48,49]. In this discussion, that method will be summarized briefly, with particular emphasis on those features which differ from the procedure followed in the Wonder Bldg.

The spark unpacking procedure was identical to that used in the Wonder Bldg. The alignment of the target chambers proceeded in a similar fashion to that described above. The locations of each chamber were first measured with surveying instruments. The alignment was then done in a two step iteration. First, two chambers were fixed and the residuals were minimized for the other chambers in the target. When this iteration had converged, two different chambers were fixed and the procedure was repeated. This procedure converged by the time the third set of fixed chambers was selected. The toroid chambers were aligned by simultaneously fitting the momenta of muons and minimizing the fiducials. This procedure automatically assured that the toroid chambers were aligned with the target.

The momenta of muons in neutrino events was fit iteratively, as in the Wonder Bldg. Unlike in the Wonder Bldg., the χ^2 function which was minimized was not a

function of fit parameters. Rather, a simultaneous fit was done to all sparks in both the target and the toroid system. This function was given by:[48]

$$\chi^2 = \sum_i \sum_j (x_i - x_i^P)\, \varepsilon_{ij}^{-1}\, (x_j - x_j^P) \qquad (7)$$

where x_i (x_i^P) is the measured (predicted) position of the spark and ε^{-1} is the inverse of the full error matrix. Note that due to the different fit technique followed in Lab E, this is <u>not</u> the same ε as given above for the Wonder Bldg.

The results of this procedure are given in Fig. IV.2 for each of the six train settings.

Figure IV.2: Shown are the muon momentum (p_μ) distributions for the Lab E detector at each of the six secondary momentum settings.

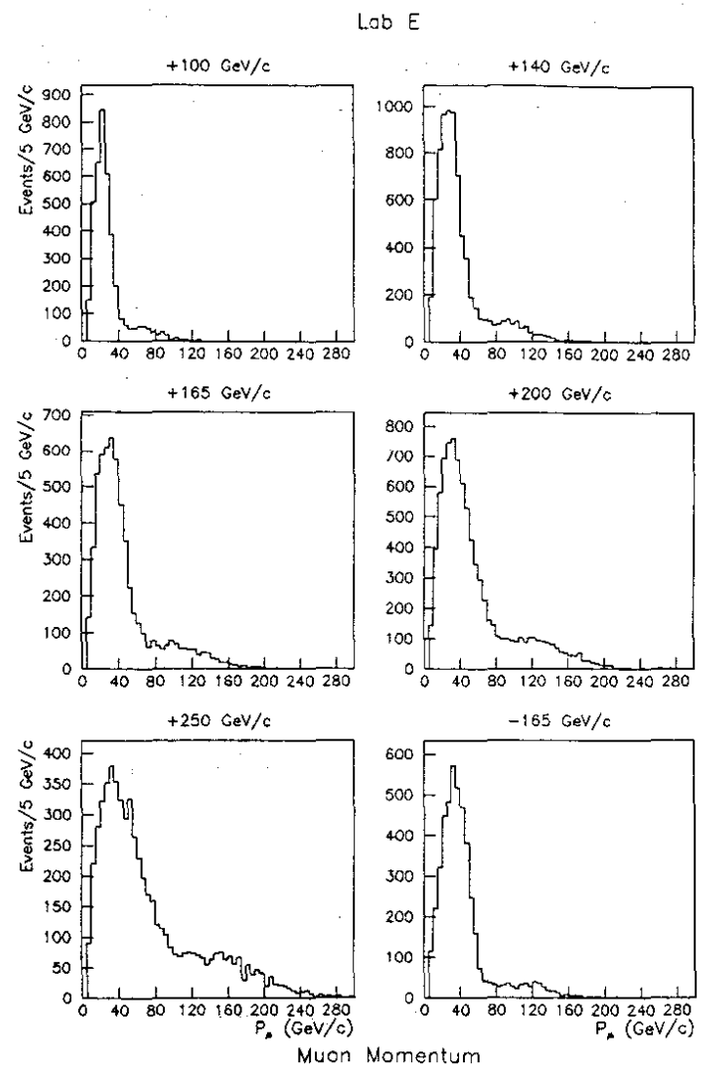

Section IV.2: Determination of Hadron Energy

Section IV.2.1: Wonder Bldg.

The Wonder Building calorimeter has been described above (cf. p. 64). The process of converting the pulse height information from the high, low, and super-low ADCs into a measurement of the hadron energy of an event is, in principle, straight-forward. The calorimeter must first be calibrated, which means that the relationship between scintillation counter pulse height and energy must be determined. This is done by measuring the dependence of the pulse height deposited by a minimum ionizing particle on the absolute energy (say, in GeV). The best way to do this is by using a test beam of hadrons and muons. Having obtained the calibration factor, one then finds the minimum ionizing peak for a counter in the neutrino data (using the appropriate un-saturated ADC), and uses that peak to calculate the hadronic pulse height in absolute units.

Unfortunately, the Wonder Building did not operate in an ideal world. The principle factors which complicated the afore-mentioned procedure were: non-linear ADCs (i.e. the number of ADC counts wasn't exactly proportional to the input voltage), non-zero pedestals in the ADCs, drifts in the gain of the counters (i.e. $E_{had} = a_1 P.H.$ one day and

$a_2 P.H.$ the next), failures of ADCs, non-uniform counter response (cf. map description, p. 66), and the lack of a calibration beam in the Wonder Building. The technique used to reconstruct the hadron energy (E_{had}) in an event under these conditions is given below. Further information may be found in Ref. 56.

Before any corrections could be applied to the ADC pulse heights, the pedestals had to be subtracted. The pedestal of each ADC channel was measured during a special "pedestal gate" between beam spills. The ADCs were turned on for 200 ns during this gate, and the running average of the measurement was used to subtract the pedestals in the neutrino data.

The pulse heights were first corrected for the non-linearity in the ADCs. This non-linearity may be parametrized as:

$$R = aV^{1+\alpha}$$

where R is the number of counts in an ADC channel, V is the voltage at the ADC input, a is an arbitrary constant, and α is a small constant (ranging from .01 to .03) which reflects the non-linearity. The value of α was determined for each channel by measuring the response, R, of each ADC channel to 30 ns wide pulses from a linear source (Mercury pulser). An

example of such a measurement, together with its fit, is shown in Fig. IV.3. The measured non-linearity, α, was used to correct the pedestal-subtracted pulse height.

Figure IV.3: Shown is the ADC response as a function of input voltage (points) and a fit to that data (curve) with α = .013 in the equation given above.

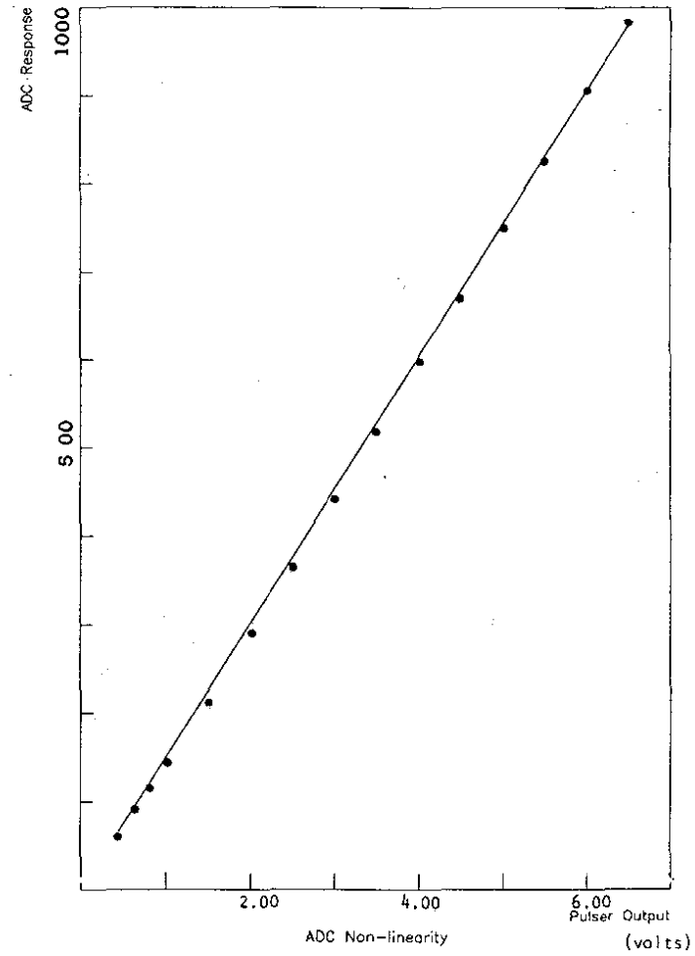

The effect of drifts in the gains of the phototubes was removed by using information from the light flasher system. For every two days of data taking, the following quantity was calculated:

$$d(t) = \frac{\text{Flasher P.H.}(t)}{R(t)/\text{NaI}(t)}$$

where R(t) is the reference tube pulse height, NaI(t) is the mean value of the Am peak in the NaI, and t is the time elapsed since the beginning of the data-taking. The drift was defined to be:

$$\text{drift}(t) = \frac{d(t)}{d(0)}$$

A value of the drift was obtained for each tube, and each counter's pulse height was corrected by that quantity. Three examples of this quantity as a function of time are shown in Fig. IV.4. The importance of the NaI information in monitoring the gain of the counters is illustrated by Fig. IV.5. There is shown the value of NaI(t) over a period of four months. The gain of the reference tube is seen to be unstable at the 10 % level over a period of four months.

Figure IV.4: Shown is the value of the drift for 3 phototubes over a period of one week.

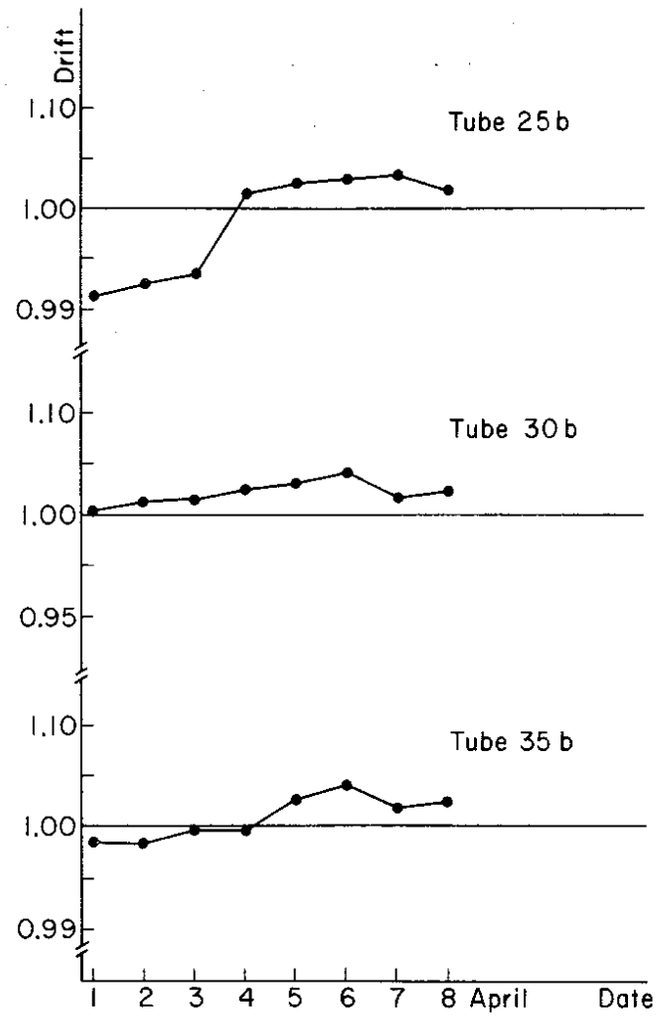

Figure IV.5: The value of NaI(t) is given over a 4 month period. The size of the fluctuations indicates a 10 % variation in the gain of the reference phototube.

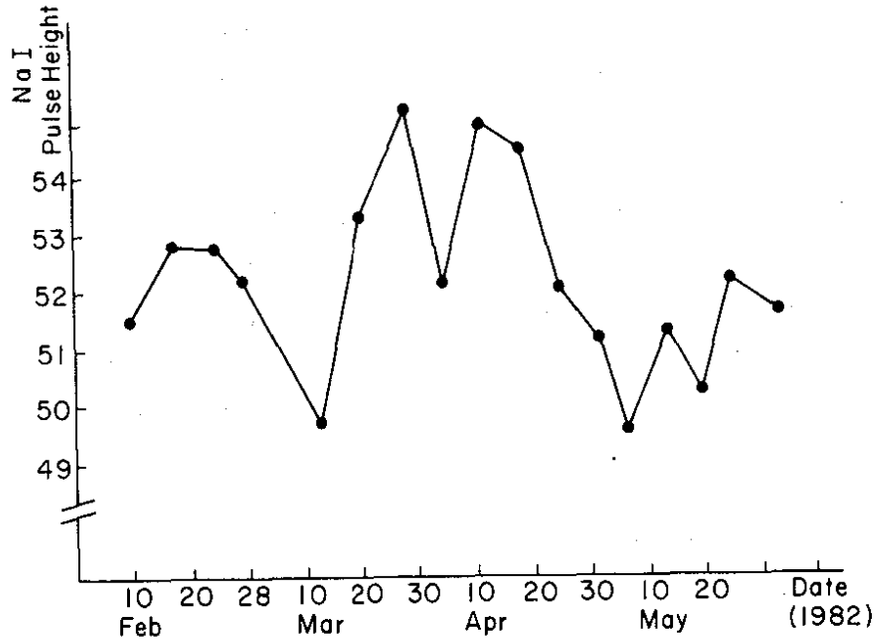

The pulse height, P, from each counter was then calculated in terms of "equivalent high channels". For those counters whose high ADC was neither saturated nor broken, this quantity was just the contents of the high ADC. If the the high could not be used, then the data from the low ADCs, L_i, were used; P was then given by:

$$P = a_1 L_1 + a_2 L_2 .$$

The a_i were calculated using the data where both the high and low pulse heights were reliable. These co-efficients were approximately equal to 10. For those events in which one low failed, the other low was used. If both the highs and lows were broken and/or saturated, the superlows were used to obtain the total pulse height. A superlow, SL, was related to low ADCs by:

$$SL = \Sigma \alpha_i L_i$$

where the α_i were approximately equal to $\frac{1}{6}$. The value of a particular low, L_j, was extracted using the values SL and L_i ($i \neq j$). The precise values of the co-efficients, α_i, were calculated using data for which both SL and the L_i were usable. The approximate regimes where the different types of ADCs were used is shown in Table IV.1.

Table IV.1: Shown are the energy regimes in each detector which were covered by each of the elements (high, low, and superlow ADCs) in the calorimeter electronics. For example, if between 4.5 and 45 GeV of hadronic energy was deposited in a Wonder Bldg. calorimetry counter, then the low ADC would be used. These ranges are given for both Lab E and the Wonder Bldg.

ADC Type	Lab E Range (GeV)	Wonder Bldg. Range (GeV)
High	0 - 5.5	0 - 4.5
Low	0 - 170	0 - 45
Superlow	10 - 1000	10 - 1000

The pulse height, P, which was thus obtained was then corrected for the non-uniformity of the counter's response across its face using the radiation source maps. The event vertex calculated from the spark chamber data was used to obtain the correction factor. The muon position was used to choose the correction factor downstream of the hadron shower. The map was the last factor for which the pulse height needed to be corrected.

The first step in converting the corrected pulse height into energy was to determine the maximum of the minimum ionizing particle distribution (the "muon peak"). This was done by an iterative procedure. The muon peak was assumed to have a default value, p_0 (usually 40 channels in a high ADC). The corrected pulse height for a counter was then histogrammed from 0.1 to 2.0 x p_0 for events comprising two days of data-taking. A new muon peak, p_1, was then found, and the procedure was repeated with the histogram running from 0.1 to 2.0 x p_1. The procedure was declared to have converged when $|p_i - p_{i+1}| < 0.01\ p_i$ was satisfied. An example of a muon peak resulting from the process is shown in Fig. IV.6.

Figure IV.6: Shown is a muon peak obtained from a calorimetry counter in the Wonder Bldg. detector over two days of running. Typically 1500 to 3000 events were used in the calculation of each muon peak.

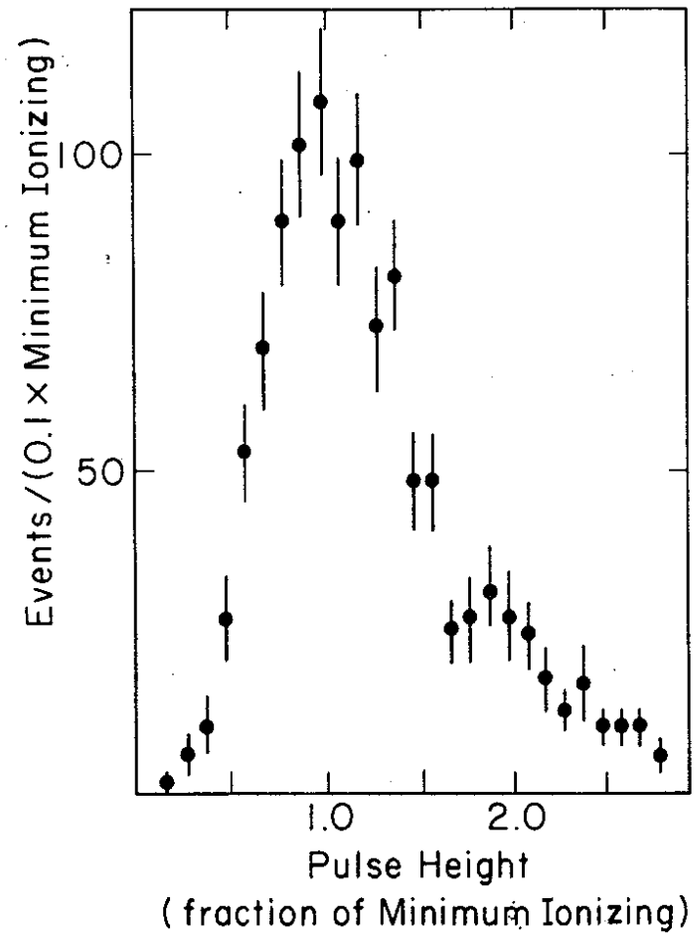

After all of the muon peaks had been calculated for each period of running, the pulse height was converted into "times-minimum", i.e. corrected pulse height ÷ muon peak, for each counter in the calorimeter. As mentioned above, it is preferable to obtain the conversion factor between times-minimum and GeV from test beam data. As this was impossible, the conversion factor was calculated with reference to the Lab E detector (which had been calibrated with hadrons during an earlier run of the experiment). For each secondary momentum setting, the hadron energy of the ν_k events with vertices inside a 25" (39") square box at the Wonder Building (Lab E) were histogrammed. The WB conversion factors were chosen so that the mean hadron energies for these plots were the same in each detector. The results of this procedure are shown in Table IV.2. The hadron energy distributions in the Wonder Bldg. detector for all train settings are shown in Fig. IV.7.

Table IV.2: Values obtained for the Wonder Bldg. calibration constant for each train setting.

Train Setting (GeV/c)	Wonder Bldg. Calibration (GeV/minimum ionizing)
+100	.152 ± .010
+140	.161 ± .007
+165	.171 ± .005
+200	.165 ± .005
+250	.169 ± .004
-165	.171 ± .005
Average	.164 ± .003

Figure IV.7: Shown are the hadron energy distributions for the Wonder Bldg. detector at all six secondary momentum settings.

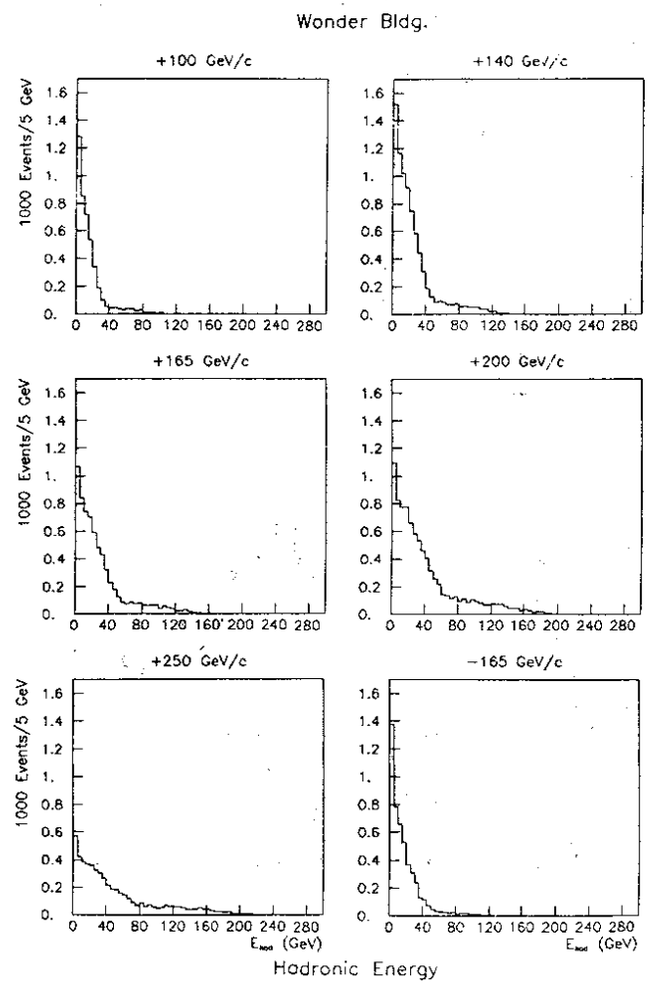

Section IV.2.2: Lab E

The method used to obtain E_{had} in Lab E was very similar to that used in the Wonder Bldg. The principle differences were: (a) the ADCs were more linear and had a larger dynamic range than those in the Wonder Bldg.; (b) the light flasher system could only be used for correcting the gains of phototubes in a counter with respect to each other, not to correct a single tube's drift as a function of time; (c) maps calculated from hadronic showers were used to make corrections for the variation in response over the face of a counter; and (d) the Lab E calorimeter had been calibrated in a hadron beam during a previous experiment. These differences will be discussed below; the procedure for obtaining E_{had} will then be briefly outlined.

The ADCs which were used in Lab E (LRS 2280) were in almost all respects superior to those installed in the Wonder Bldg. The single exception was the poor mechanical design which made them awkward to maintain. The first advantage was their dynamic range, which was 15 bits as opposed to 10 bits for the ADCs in the Wonder Bldg. As is shown in Table IV.1, this made the Lab E calorimetry less dependent on the redundancy provided by the High-Low-Superlow system described above for the Wonder

Bldg. The equivalent system existed in Lab E, with the LRS 2280's being used as low ADCs and LRS 2249A's being used as high and superlow ADCs, but in practise the low ADCs were almost invariably used. The minimum ionizing peak was set to be in approximately channel 40 in both the high and the low ADCs, so that the high channel was only necessary if the low failed. Since the low ADCs saturated at channel 32767, the superlows were needed only when the pulse-height exceeded that value (i.e. never) or when a low ADC failed.

The second advantage of the Lab E low ADCs was their linearity. The co-efficient α described for the Wonder Bldg. non-linearity measurements above (cf. p. 126) was zero for these ADCs. Thus only the "back-up" ADCs - the highs and superlows - needed to be corrected for non-linearity.

Unlike the ADC system, the light flasher system in Lab E was inferior to that in the Wonder Bldg. This was because the time-dependence of the light source was not monitored by a reference phototube. Thus, the system was useful only for determining how the gain of the four phototubes in a counter with respect to each other changed as the run progressed. The gain of a single phototube could not be monitored, and the counters could not be "balanced". This was because light flashes were not distributed evenly to all four

phototubes.

Radiation source maps were not available for the Lab E counters. Maps calculated from hadronic showers were used to determine the position-dependent corrections instead. Events were required to fire the muon trigger and have a vertex within 50" of the centre of the detector in order to be included in the calculation. In addition, the four tubes of a counter had to have a pulse height above twice minimum, be one of the first 4 counters in the shower, and have a left-right symmetry of less than 30 %. The maps were calculated using a five parameter fit with the computer program MINUIT.[64] The attenuation lengths in x and y were given by λ_x and λ_y, the relative gains of three phototubes with respect to the fourth were g_1, g_2, and g_3. These co-efficients were required since measurements using a radioactive source determined that the flasher did not correctly balance a counter. The attenuation lengths of the wave-shifter bars were fixed at 115 cm in the fit. The maps were calculated for a "reference section" of the data in the middle of the data-taking period. A map averaged over all of the counters in the calorimeter in shown in Fig. IV.8.

The last important difference between the two calorimeters was that Lab E had been calibrated with a beam of pions ranging in energy from 50 to 250 GeV. The

calibration constant was found to be 0.216 GeV per minimum ionizing particle. This value was obtained two years before the experiment described herein ran. Preliminary analysis of recent data (taken two years after the run of the ν oscillation experiment) indicates that this calibration constant has not changed.[65]

The procedure which was used to calculate E_{had} from the pulse height is similar to that described above for the Wonder Bldg. The pedestals are first subtracted using data taken during a special pedestal gate. The high and superlow ADCs were then corrected for non-linearities (this was not necessary for the lows, as noted above). The drifts in the relative gains of the four phototubes on a counter were then corrected relative to the aforementioned reference section of the data-taking. This was done using information obtained with the light flasher system. Muon peaks were then calculated using the same procedure as was followed for the Wonder Bldg. (p. 134). The map correction was applied and new muon peaks were calculated using the previous value as the input to the iterative procedure. Finally, small corrections were made based on the measured shape of the hadron showers, following the procedure of Ref. III.4, p. 43. After a corrected pulse height had been found, E_{had} (in GeV) was obtained using the measured calibration constant. The final E_{had} distributions are

shown in Fig. IV.9.

Figure IV.8: Shown is a typical response map for a counter in the Lab E calorimeter. If an event falls on the innermost contour, its pulse height is corrected by a multiplicative factor of 1.05. This factor is 1.10 for the second contour, 1.15 for the third, and so on.

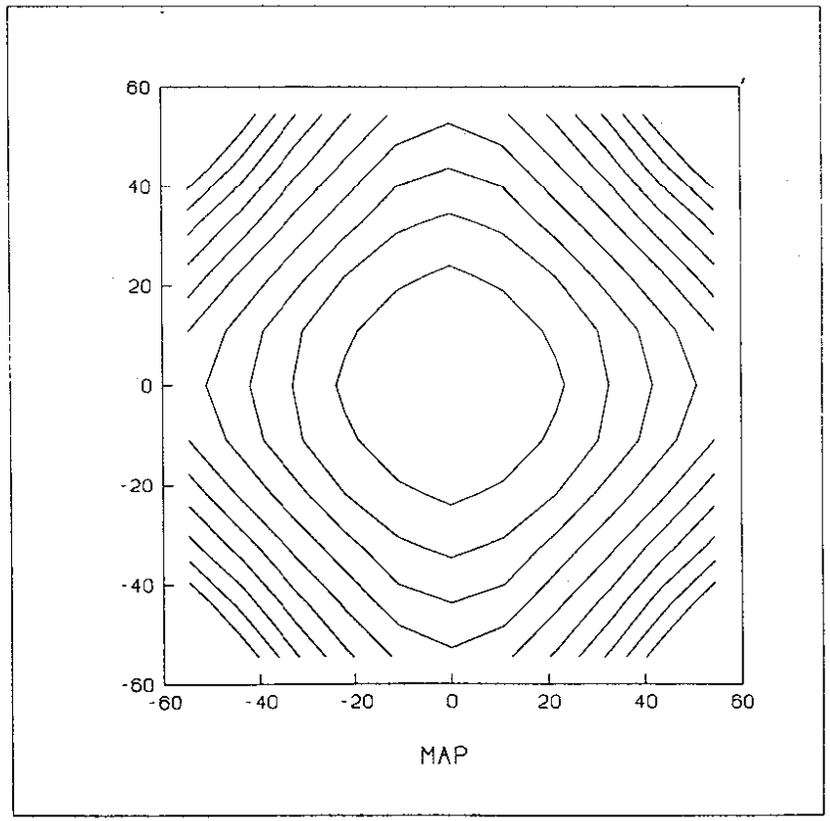

Figure IV.9: Shown are the distributions of E_{had} for the Lab E detector at each of the six secondary momentum settings.

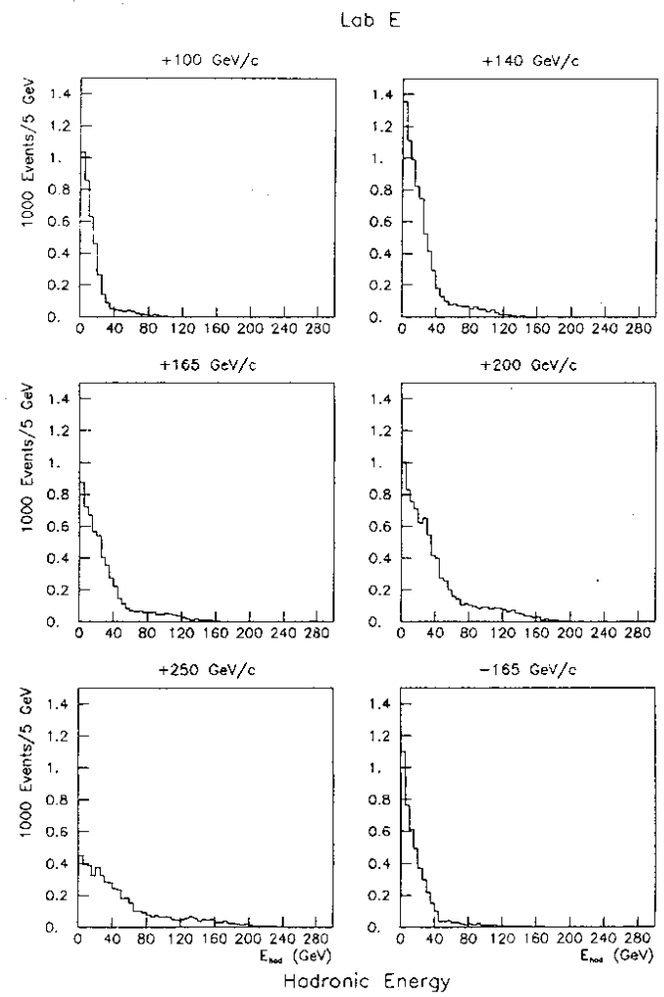

CHAPTER V

The Oscillation Analysis

In order to complete the data analysis, it was necessary to use the results of the event reconstruction programs described above to obtain the ratios of events between the two detectors. This process involved merging the monitor, Lab E, and Wonder Building data summary files (DSTs), selecting that data which was taken during good running, applying cuts to the events so that the acceptances of the two detectors were similar and restricted to analysable data, and binning the events from each detector so that ratios of events in energy bins could be calculated.

Section V.1: Merging

Combining the monitor, Lab E, and Wonder Building DSTs into a single merged DST file was, in principle, a

straight-forward task. Each monitor record contained the pulse number from the accelerator, the run numbers at each detector, and the PDP on-line computer cycle number for that spill in each of the two runs. The merging program would only need to read the pulse number from the monitor record, search the Lab E and WB files for events with the same pulse number, and then combine any events found with the monitor record to form a "pulse buffer". The run and cycle numbers would then be available as a cross-check.

Several problems prevented the smooth implementation of such a scheme. The greatest single problem was that the beamline control system, which provided the monitor information (including the pulse number) to the experiment, failed sporadically during the run, and failed frequently during several isolated periods. Additionally, an un-diagnosed problem in the on-line software in the Wonder Bldg. caused the pulse number to be recorded incorrectly on occasion. There were no problems with either the run or cycle number in either detector, as these were not obtained from the beamline system.

Bearing these difficulties in mind, the following merging procedure was followed. When the merging program read a monitor record, it picked out the Lab E run and cycle numbers, and the Wonder Bldg. run and cycle numbers for use

as "matching variables". It first searched the Lab E event file for all events with the correct run and event number. If any such events were found, they were placed in a pulse buffer behind the monitor record. The program then searched the Wonder Bldg. event file for events with matching Wonder Bldg. run and cycle numbers. Such events (if any) were added to the end of the pulse buffer. If any events contained in the buffer after this procedure had a pulse number which differed from that in the monitor record, a flag was set. Pulses were rejected later in the analysis by checking this flag. Some events did not have a matching monitor record. This could occur when the beamline read-out devices failed at both detectors and bad monitor records were produced. These "orphan" events were packed into separate "phoney" pulse buffers and written to the Merged DST (MDST). They were not used in the oscillation analysis, but were available for other studies.

Section V.2: Good Running Requirements

Certain portions of the data set were rejected because the data was obtained during "bad running". The most common cause of bad running was failures in the spark chamber system, typically caused by contamination of the gas. When this occurred, the chamber efficiency deteriorated badly. There were times when one or both of the toroidal magnet

systems tripped off; events from these episodes were rejected since they could not be momentum analysed. Other causes of bad running were beamline gating problems, fast trigger logic failures, computer hardware failures, beamline monitor failures, and off-line software errors. The number of events cut by these conditions is shown in Table V.1.

Table V.1: Total numbers of events in each detector for different running conditions.

	After Monitor Cuts	After Good Running Cuts	After Steering Cuts
Lab E	179615	123808	112582
Wonder Bldg.	155617	107245	96527

Section V.3: Event Selection

The success of the oscillation analysis depended on obtaining data sets in Lab E and the Wonder Building which had the same acceptances. While the two detectors were of similar design, their muon triggers had somewhat different acceptances. It was also necessary to apply cuts which guaranteed that those events accepted by the analysis software could be fully reconstructed. These cuts shall be described in the order in which they were applied. Then the methods of equalizing acceptances (called "projection cuts") shall be explained.

Section V.3.1: Quality of Data Cuts

There were two types of selection criteria which were applied to the data: "geometrical" and "momentum" cuts. Geometrical cuts used the measured vertex and muon trajectory to detemine the quality of a neutrino event, while the momentum cuts depended on the values of p_μ and the χ^2 of the momentum fit. The geometrical cuts will be described first.

The first group of geometrical cuts was applied to the measured vertex of an event in order to guarantee that there was no leakage of hadron energy out of either the downstream end or the sides of the calorimeter.

Figure V.1: Shown are distributions of the longitudinal vertex, PLACE, for the +250 GeV/c secondary momentum setting. The cuts on PLACE are indicated on the plot.

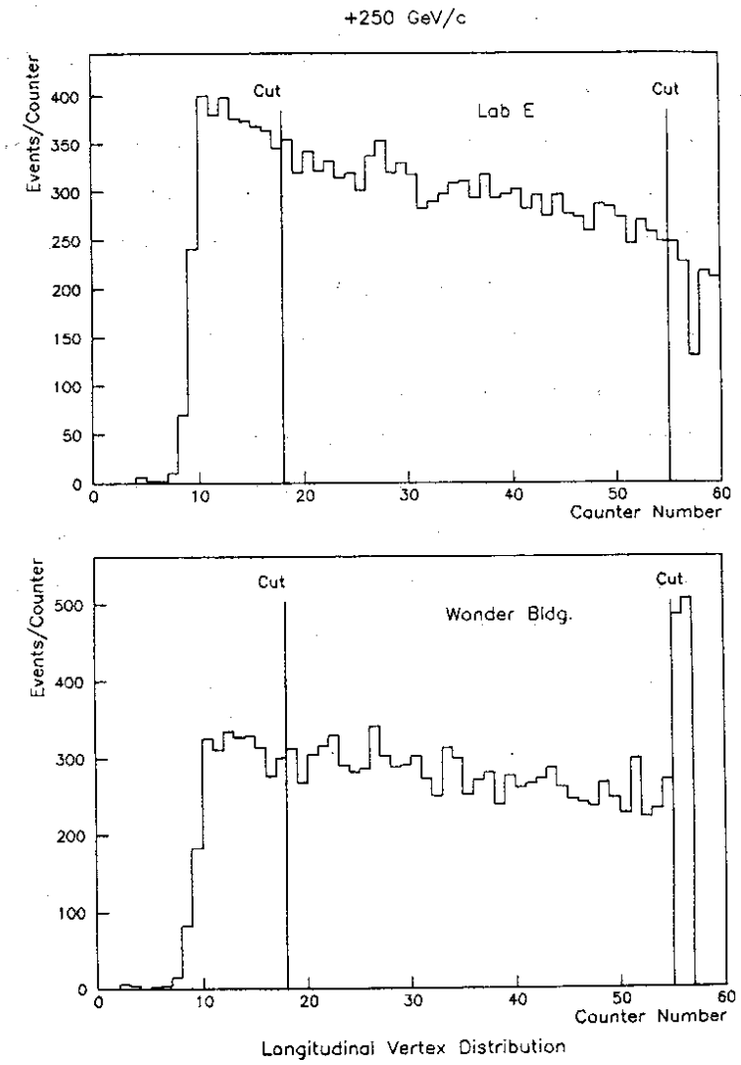

Longitudinal shower containment was ensured by cutting on "PLACE", which was defined to be the nearest scintillation counter to the neutrino interaction vertex. All events were required to have PLACE between 18 and 54 inclusive. Distributions of PLACE with these cuts indicated are shown in Fig. V.1. The upper bound of 54 was chosen to minimize the possibility of a neutrino event in the Wonder Bldg. being vetoed because of particles from a hadronic shower going backward to fire the Veto counter. The lower bound of 18 was chosen so that the fraction of the hadron shower punching through the end of the calorimeter was minimized. If a significant amount of hadron energy was lost, then ν_k events might be misidentified as ν_π events. Events from the +250 GeV/c train setting which occurred in the middle of the calorimeter (18 < PLACE < 36) were used to study the effect of this cut; we found that less than 5 % of the hadronic energy was lost when the cut was applied at counter 18. For a PLACE cut larger than 14, no ν_k event was misidentified as a ν_π event (cf. Fig. V.2).

Figure V.2: Shown is the percentage of ν_k events which are mis-identified as ν_π events as a function of the PLACE cut. As the cut increases, more events are correctly identified because of improved longitudinal shower containment.

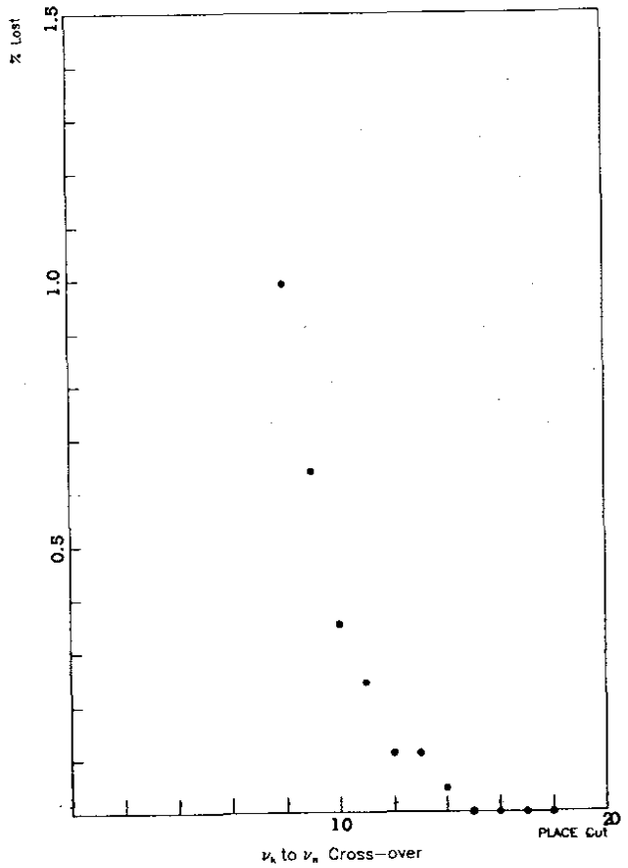

In order to minimize the transverse shower leakage, a "square cut" was applied to the x- and y- vertices of the events. Since the Wonder Bldg. calorimeter measured only 5′ x 5′ transversely (as opposed to 10′ x 10′ for Lab E), the events were required to lie within a 50" x 50" box centred on the calorimeter (the technique used to transform this requirement to the Lab E detector is discussed on pp. 165-166).

In addition to passing the square cut, an event was required to have a radius within 25" (22.5") of the centre of the beam at the Wonder Bldg. for ν_k (ν_π) events. (Again, this cut's application to Lab E events is described below). The ν_π events are cut at a smaller radius because those outside of the 22.5" cut tend to come from the tails of the pion angular distribution. These tails may not be simulated as well as the central portion of the beam. The ν_k events, as noted above, are little affected by the angular divergence of the beam. The method used to separate ν_π from ν_k events is described below (cf. p. 174).

The effectiveness of these cuts in containing the hadron shower was studied by dividing the calorimeter into octants. If leakage was occurring for a particular square cut, then the effect would be less in the corner octants due to the additional steel between the square and the edge of

the calorimeter. The absence of a difference indicated that containment was not a severe problem. The mean hadron energies for ν_k events in the corner and side octants were in the ratio 0.986 ± .015 for the +250 GeV train setting. Since these hadron showers were more energetic than those at the other train settings, this number gives the upper bound on the effect of any leakage.

Figures V.3,4, and 5 show the vertex (in x and y), and radius distributions for Lab E and the Wonder Bldg. The cuts described above are indicated on the figures. These plots are for the +250 GeV train setting.

Figure V.3: Shown are the x- and y- vertex distributions for both the Lab E and Wonder Bldg. detectors at the +250 GeV/c secondary momentum setting. The PLACE cut is already applied to these data; the vertex cuts are indicated.

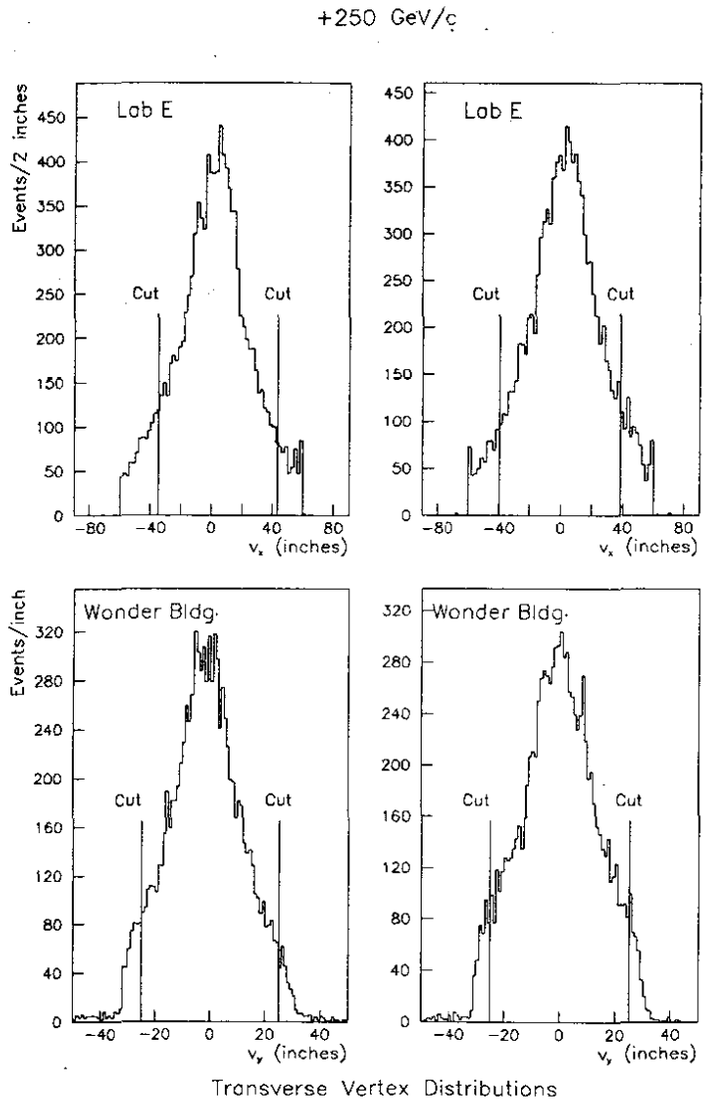

Figure V.4: Shown are the radius distributions of ν_π events in both detectors at the +250 GeV/c train setting. The vertex cuts are already applied and the radius cut for ν_π events is indicated.

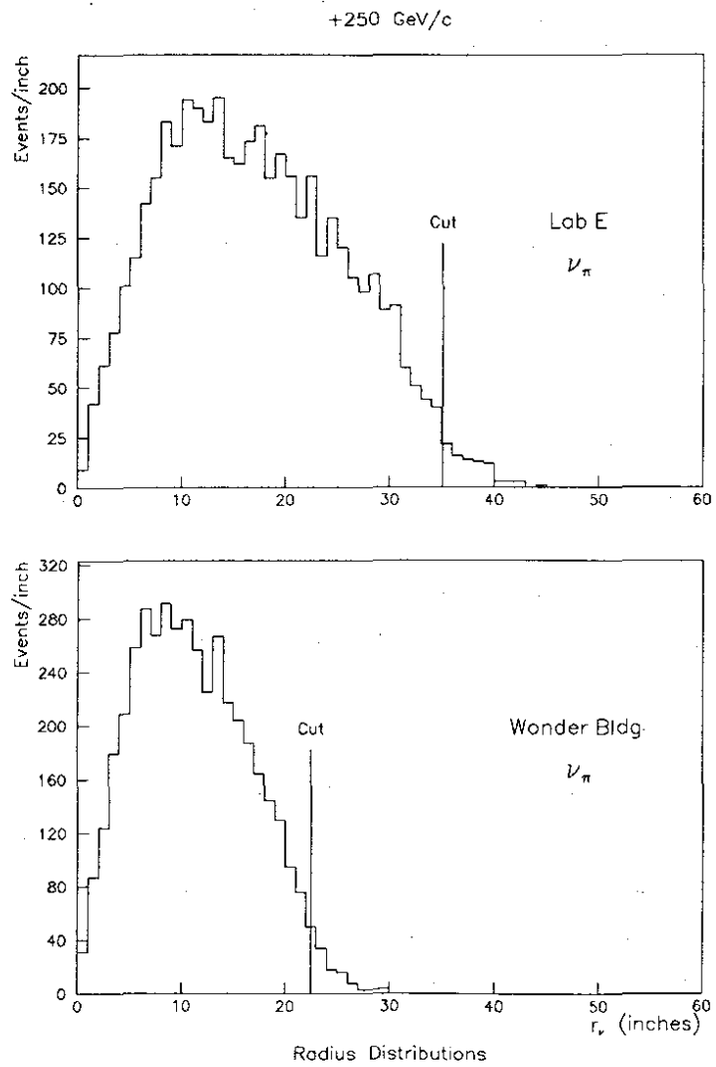

Figure V.5: Shown are the radius distributions of ν_k events in both detectors at the +250 GeV/c train setting. The vertex cuts are already applied and the radius cut for ν_k events is indicated.

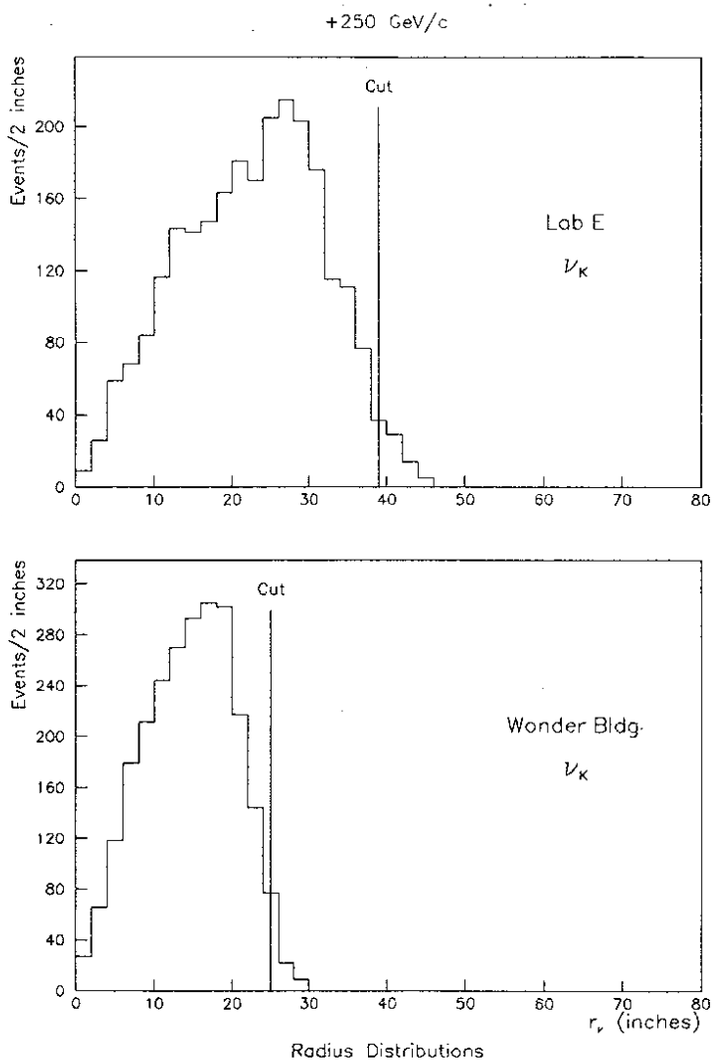

The cuts mentioned so far were devised to ensure that the hadron energy was accurately measured. There was a further set of cuts, this time applied to the muon trajectory. These cuts were intended to select events whose p_μ could be accurately determined. All cuts on the muon trajectory were momentum-independent. Only the vertex of the interaction and the production angles of the muon were used to determine whether an event was used in the later analysis.

Figure V.6: A sample charged current ν interaction is shown to illustrate the muon trajectory cuts. The extrapolation of the muon trajectory is required to satisfy cuts at the toroidal magnet and trigger counter T2.

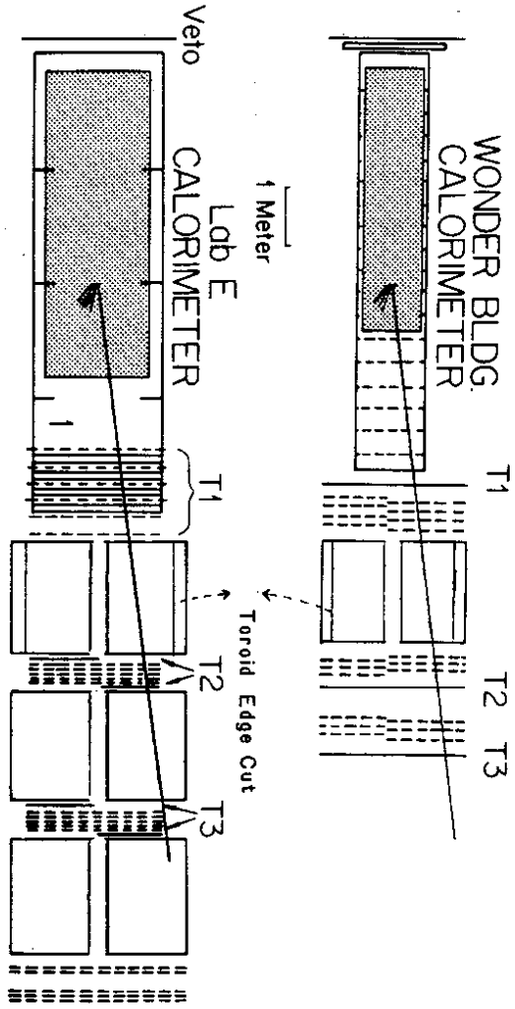

The muon trajectory cuts are illustrated by Fig. V.6. There is shown a sample event in the target calorimeter, together with the locations of the toroidal magnets and counter T2 in each detector. The first cut applied to an event was a requirement that θ, the angle of the muon with respect to the longitudinal axis of the detector, be less than 200 mr. The θ distributions are shown in Fig. V.7. A series of cuts were then applied to the straight-line extrapolation of the muon track through the magnets and trigger counters.

Figure V.7: Shown are the θ_μ distributions for events in Lab E and the Wonder Bldg. at the 100 GeV/c secondary momentum setting. Shower containment cuts have already been applied.

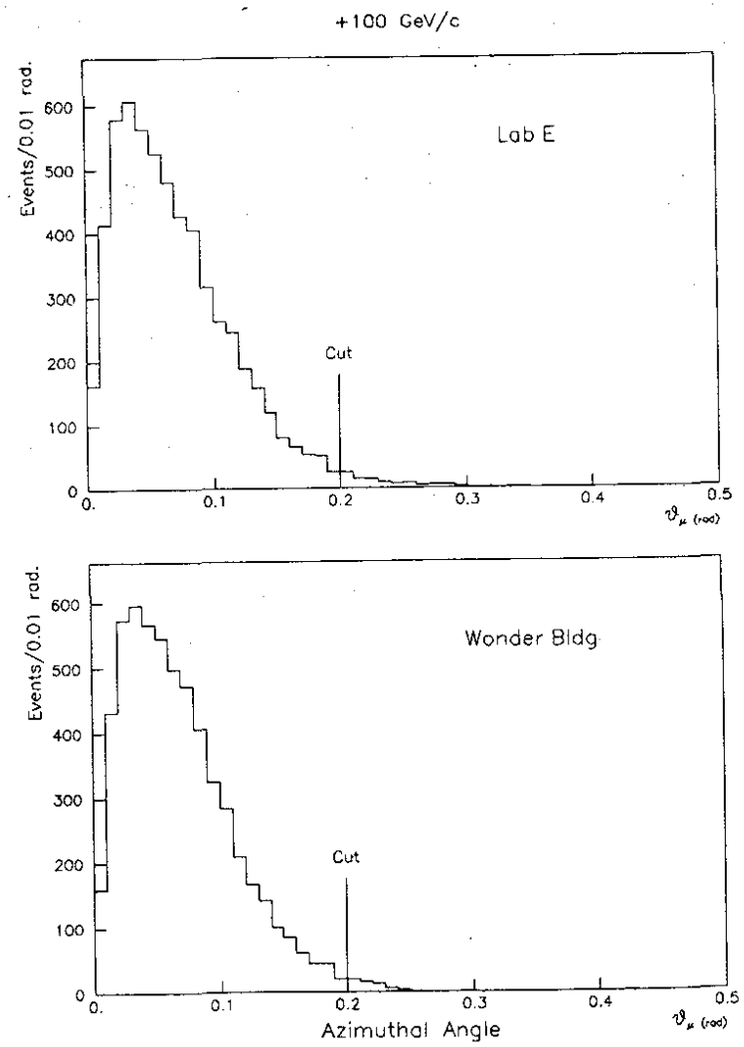

The extrapolation was first required to pass through trigger counter T2. This cut provided a momentum-independent means of ensuring that the muon would fire T2, and thus the muon trigger. enough). There were then applied cuts which required the extrapolation to (a) have at least 80 % of its path in the magnet steel, and thus less than 20 % in the 10" diameter central hole (this was called the "Hole Cut"); and (b) enter the magnet at least 5" from its edge.

There were two cuts on the reconstructed muon momentum. The minimum momentum which could be efficiently measured was 6.5 GeV/c at the front face of the toroid. This was due to the dE/dx loss of the muon in the iron toroidal magnets. The reconstructed momentum was required to be larger than this value. If the muon was determined to be de-focussing (a "wrong sign" event), then the event was rejected. Such an event may not arise from the standard charged current neutrino interaction, and is usually due to a background anti-neutrino.

Section V.3.2: Projection Cuts

In order to make the acceptances of the two detectors identical for a particular neutrino interaction, it would be

necessary to first apply cuts in the detector where the event occurred and then extrapolate the neutrino along its trajectory from the decay pipe to the "corresponding" location in the other detector. The cuts pertaining to the second detector were then applied. There were two difficulties with this procedure. First, the neutrino's trajectory was not known; only the interaction vertex in one detector is measured. Second, the corresponding location in the other detector was not well defined.

Addressing the second question first, the vertex in the second detector was required to have the same "PLACE" as in the detector in which it occurred. Choosing this vertex gave the same amount of steel to absorb the hadron energy in each apparatus because the density of material in the two detectors was nearly identical.

The neutrino trajectory was obtained by using an approximation. For the purpose of extrapolating an event from one detector to the other, the neutrino was assumed to have originated at the centre of the decay pipe. The trajectory was then defined by this point and the interaction point in the detector where the event occurred. This procedure is shown schematically in Fig. V.8.

All cuts which used the extrapolation of the muon

trajectory (ZT2, toroid edge, hole-cut) were then easy to apply. Once the event's "vertex" had been determined, the muon's production angle from the original detector determined the extrapolation. As all p_μ cuts were applied to the momentum at the toroid front face, and there was the same amount of material between any given counter and the toroid front face in both detectors, the acceptances of the p_μ cuts were the same in each detector. The cuts on the χ^2 of the momentum fit are different for the two detectors. This is corrected for by a reconstruction efficiency correction, described below (p. 170).

As noted above, the transverse vertex and radius cuts were defined at the Wonder Bldg. detector. These cuts were extrapolated to the Lab E apparatus using the projection technique just described. The number of events in the two detectors which failed each cut are given in Table V.2. The number of events passing successive cuts is given in Table V.3.

Table V.2: Number of events which fail individual cuts (independent of all other event selection criteria). The monitor and beam steering cuts have already been applied, as well as a requirement that the muon trigger must have fired.

Cut Failed	Lab E	Wonder Bldg.
Muon trigger required	112582	96527
PLACE	44109	29512
Square	40443	23591
Radius	53824	36537
θ_μ	14709	8190
T2 Cut	26334	17883
Toroid Hole Cut	6734	6624
Toroid Edge (LE)	8734	7321
Toroid Edge (WB)	12100	8205
χ^2 cut	24102	12535
Small or Negative p_μ	16650	11143

Table V.3: Number of events which fail successive cuts. The monitor and beam steering cuts have already been applied.

Cut Failed	Lab E	Wonder Bldg.
Muon trigger required	112582	96529
PLACE	77011	70899
Square	57575	58150
Radius	49399	49387
θ_μ	51528	48974
T2 Cut	44871	45310
Toroid Hole Cut	41188	41528
Toroid Edge (LE)	41188	41528
Toroid Edge (WB)	41153	41480
χ^2 cut	38206	40605
Small or Negative p_μ	36730	38989

Figure V.8: The projection cut technique is illustrated. Events occurring in one detector are "projected" to the other using the assumption that the ν originated at the centre of the decay pipe.

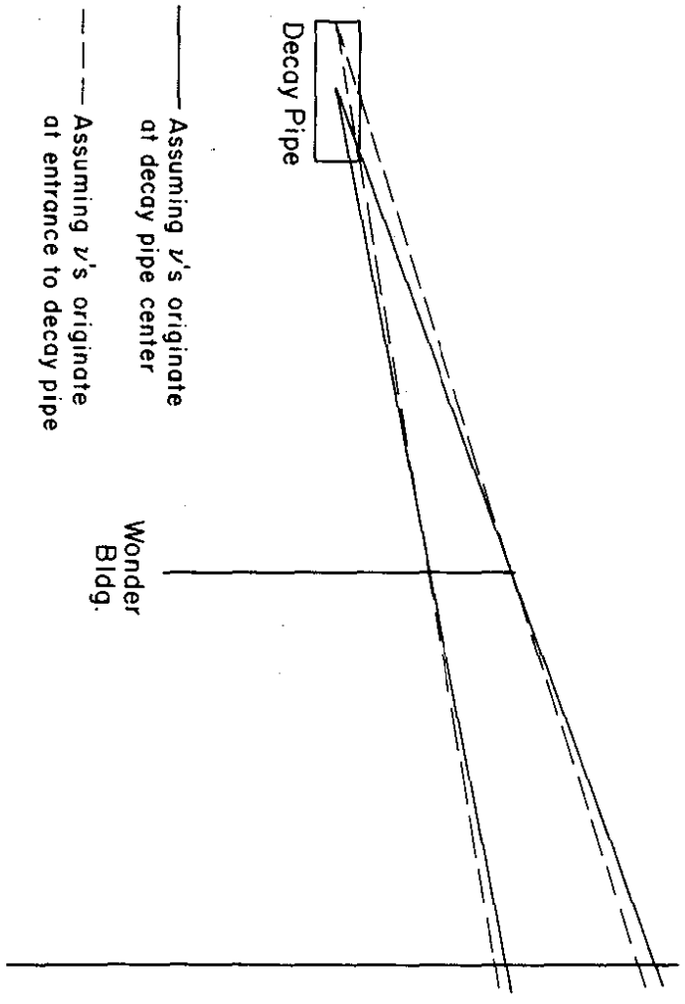

Section V.4: Reconstruction In-efficiency Correction

Due to the different problems encountered in operating the two detectors, there were different types of reconstruction failures for each apparatus. Those events which were failures (described below) were written to special "failure" output tapes. A subset of these events was visually scanned using interactive computer display programs. Those events which could be "fixed" by removing bad sparks from tracks, or by adding correct sparks to tracks were then reconstructed.

Events from the Wonder Bldg. detector were written to the failure tapes if the χ^2 of the momentum fit was larger than 8 per degree of freedom, or if the muon was de-focussing and p_μ was larger than 100 GeV/c. These criteria were determined by scanning events with $\chi^2 > 5$ and negative p_μ. Most of the large χ^2 events had the wrong sparks on the back tracks. A small number had bad sparks on the front tracks. Some events could not be fixed because of noisy or inefficient chambers. Some wrong sign events with $p_\mu > 100$ GeV actually had high momentum focussing tracks with bad sparks skewing the reconstruction program. These events are summarized in Table V.4.

Table V.4: The results of the event scanning in the Wonder Bldg. are given. The total number of events at each train setting, together with the total number scanned, and the different types of failures are shown.

Train Setting: (GeV/c)	+100	+140	+165	+200	+250	-165
Number of Good Events	4414	7769	6627	8867	6354	4958
Number Failed	73	156	131	247	205	70
Number Scanned	33	87	111	163	112	67
Irreparable Back Track	4	3	10	8	11	7
Reparable Track	25	80	89	153	98	48
Good Original Fit	1	1	3	0	3	9
Low p_μ	3	3	9	2	2	3

An event from the Lab E detector was written to a failure tape if its χ^2 was larger than 5 per degree of freedom, or if it was de-focussing with $p_\mu > 100$ GeV/c. These criteria were determined by scanning, as in the Wonder Bldg.

The results of the visual scanning are incorporated into the final event sample as follows. A weight is calculated for each radial bin at each train setting. This weight is the ratio of the total number of failures to the number of failures which were scanned and reconstructed in that bin. Each scanned event is added back into the event sample with the weight appropriate to that bin.

Section V.5: Monte Carlo Event Simulation

The projection and fiducial cuts described above rely on the assumption that the neutrino beam originated from a point source at the centre of the decay pipe. This assumption is not entirely correct. The neutrino beam, which has a non-zero angular divergence and a finite momentum bite, results from the decay of a beam of hadrons over the entire length of the decay pipe. The Monte Carlo beam simulations described in Chapter III were used to obtain corrections to the event ratios which compensated for these effects.

Thirty thousand neutrinos were generated in the decay pipe for each of the five ν and one $\bar{\nu}$ train settings. Each neutrino was required to interact in both detectors. The generation program used the Buras-Gaemers structure function parametrization[66] to obtain the kinematical variables x ($=Q^2/2m\nu$) and y ($= E_{had}/E_\nu$). These in turn were used to generate the muon momentum, azimuthal production angle, and the hadron energy.

The measured hadron energy was simulated by smearing the generated hadron energy with a Gaussian random number generator. The hadron energy resolution (90 %/ $\sqrt{E}$) was used as the standard deviation for this generator. The generated muons were propagated through the detectors, taking into account the dE/dx loss and multiple scattering of the muon in steel. The propagation of the muon through the iron toroids was simulated by using the same magnetic field function as was used for the momentum reconstruction (cf. p. 81). The spark chamber resolutions were mimicked with a Gaussian random number generator. No attempt was made to simulate either spark chamber noise or in-efficiencies.

The Monte Carlo events were analysed by using the same subroutines as were used to reconstruct the events in the actual data sample. The data summary files which were then written contained information about the incoming neutrino,

the generated event variables, and the reconstructed event variables.

Section V.6: Energy Binning

The two detectors had different energy resolutions. This made it very difficult to use measured energies for binning events. Different smearing corrections (dependent on p_μ) would be required in each detector, introducing large ($\approx$ 10%) systematic uncertainities. To avoid this problem, the dichromatic nature of the neutrino beam was used to obtain 3 energy bins for each train setting. The resolution for each bin was the same in both detectors, avoiding the complications associated with using the measured neutrino energy.

The first step in binning the data was to separate the ν_π events from the ν_K events. A general form for a radius dependent separatrix was obtained from the decay kinematics of the parent mesons. This equation was:

$$E_{sep}(r) = \frac{0.65\ E_K^{max}}{1 + r_\nu^2 B_{sep}^2}$$

The co-efficients for each train setting are given in Table V.5. The radius (in inches) of an event at Lab E is given by r_ν, while E_ν is the measured neutrino energy in GeV. It

is important to emphasize that this is the <u>only</u> way in which the measured neutrino energy is used for energy binning. Scatter plots of E_ν versus r_ν for both detectors at each train setting are given in Figs. V.9 and 10. The separatrix is indicated on the figures.

Table V.5: Values of the co-efficients in the separatrix for each of the six train settings.

Train Setting	E_k^{max}	B_{sep} (inch^{-1})
+100 GeV/c	88.0 GeV	.000
+140 GeV/c	135.3 GeV	.0126
+165 GeV/c	160.6 GeV	.0140
+200 GeV/c	190.1 GeV	.0155
+250 GeV/c	233.4 GeV	.0177
-165 GeV/c	160.6 GeV	.0140

Figure V.9: Shown are scatter plots of the measured neutrino energy vs. the event radius for each of the six secondary momentum settings in the Lab E detector. The three energy bins obtained at each setting are indicated by the solid lines.

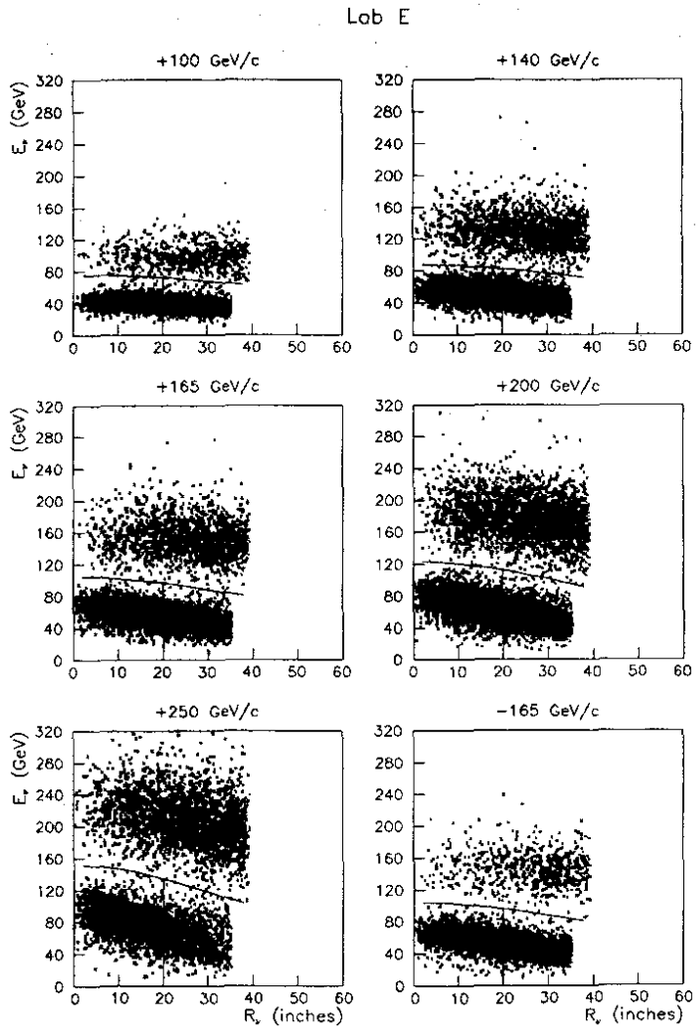

Figure V.10: Shown are scatter plots of the measured neutrino energy vs. the event radius for each of the six secondary momentum settings in the Wonder Bldg. detector. The three energy bins obtained at each setting are indicated by the solid lines.

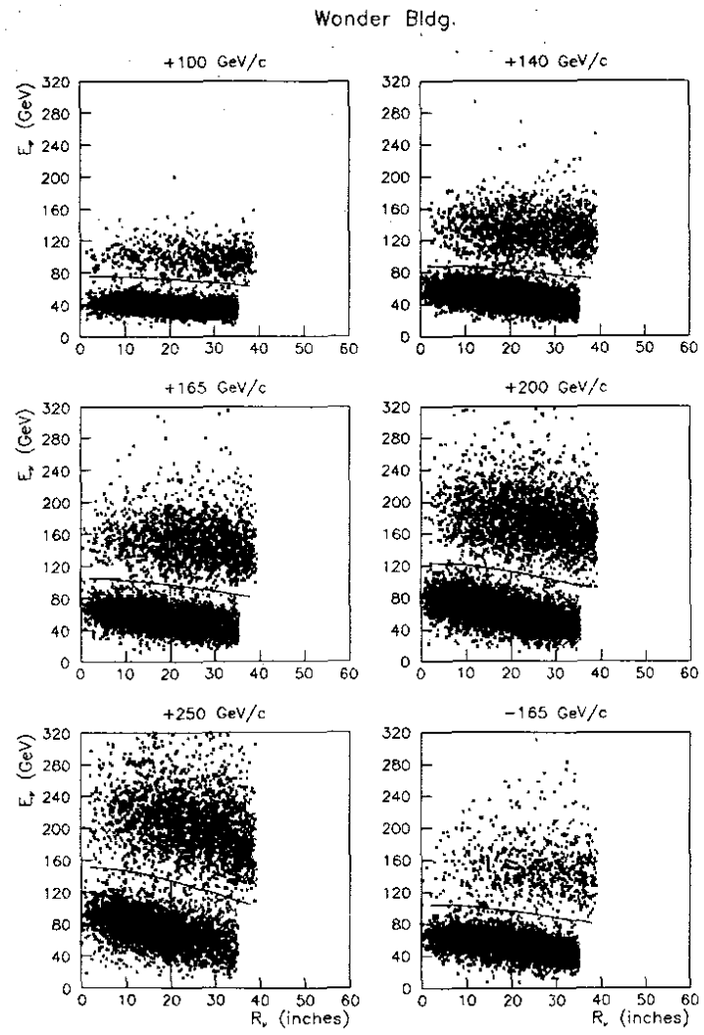

The ν_k events for a given train setting constituted one energy bin. Two additional bins were obtained by dividing the ν_π into $r\nu < 20''$ (higher energy) and $r_\nu > 20''$ (lower energy) bins. The energy resolution of these bins was completely determined by the properties of the dichromatic beam and was thus the same for each detector, thus minimizing the systematic error. The ratio of the mean measured energies, $\langle E_\nu^{LE}\rangle/\langle E_\nu^{WB}\rangle$ is shown in Figs. V.11 and 12 for the 15 ν and 3 $\bar{\nu}$ energy bins, respectively. The relative error in energy calibration of less than 5 % led to a maximum systematic error in the ν_π/ν_k separation of 0.5 %.

Figure V.11: Shown is the relative energy calibration between the Lab E and Wonder Bldg. detectors for each of the energy bins for the ν data.

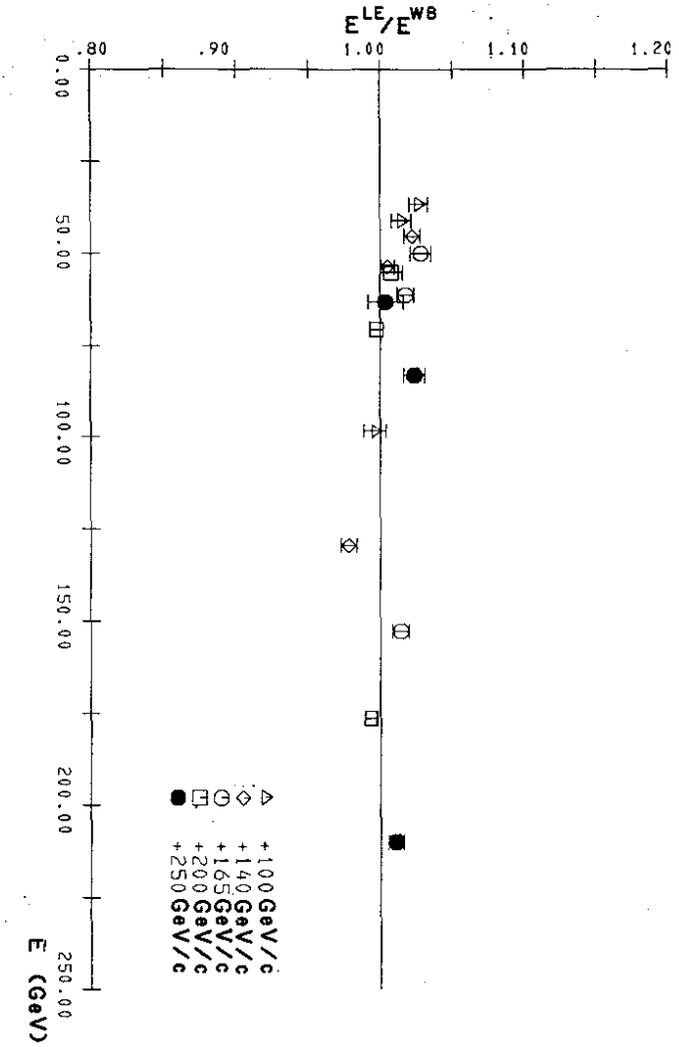

Figure V.12: Shown is the relative energy calibration between the Lab E and Wonder Bldg. detectors for each of the energy bins for the $\bar{\nu}$ data.

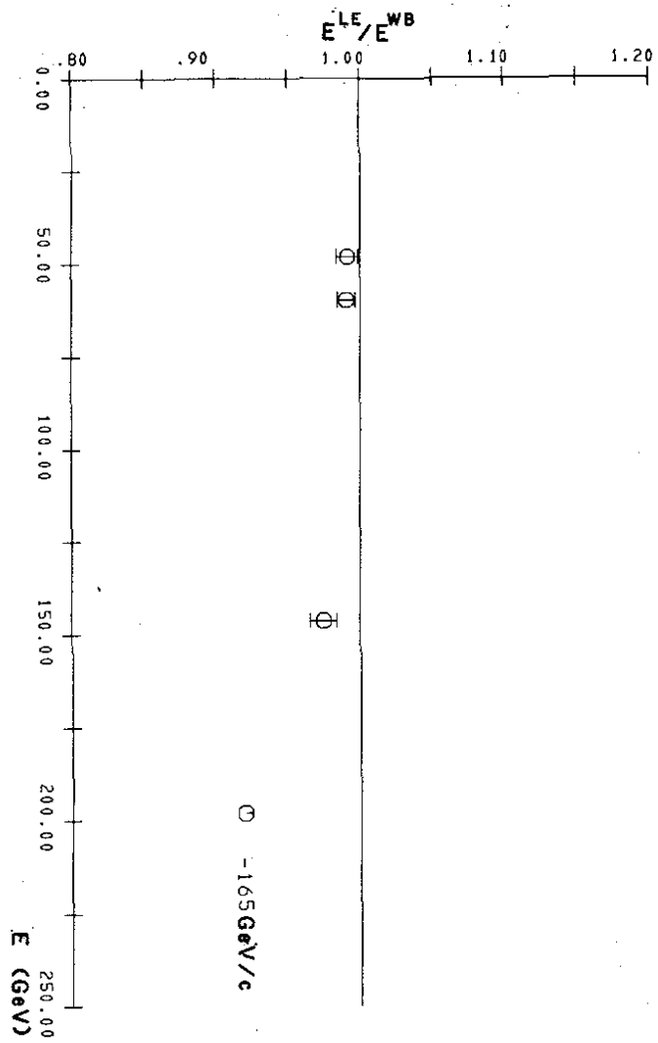

Section V.7: Calculation of Event Ratios

Both data and Monte Carlo data summary files were analysed by the same program. If the program was reading from the data files, the beam monitor information was required to to satisfy a series of cuts. These cuts guaranteed that the data was taken during good running (cf. Section V.2 above), that the monitor and event records had been successfully merged (cf. Section V.1 above), that the Neuhall Toroid (the principle livetime monitor; cf. Ch. III, p. 96), had been read in correctly, and that the beam had been correctly steered during that spill. The program kept running sums of the protons delivered to the BeO production target while each detector was live.

The events from both Monte Carlo and data files were passed through the same analysis subroutines. These subroutines applied the geometric and momentum cuts described above (cf. Section V.3). A histogramming routine allowed easy studies of the data. All events which passed the cuts were divided into ν_π and ν_k events, based on their decay kinematics (cf. Section V.6 above). A final subroutine divided the good events into the 3 energy bins at each train setting. The event totals for the data are shown in Table V.6.

The ratios shown in these tables may not be directly used to analyse the data for neutrino oscillations. There are several effects which must be corrected for to obtain properly normalized event ratios. As shown in Table V.7, the two detectors had different livetimes for each train setting. This necessitated corrections of up to 13 %. These corrections were obtained using the Neuhall Toroid; they were checked by analysing the data with a "simultaneous live" requirement. This means that an event in one detector had to occur when the other detector was live. This elliminated the need for the livetime corrections, while costing some statistical power. The systematic error estimated from this procedure is 1 %.

Table V.6: The event totals for the data are given. No corrections have been applied to these numbers. The ν_π with radii of less than 20 inches (at Lab E) are referred to as "inner ν_π" events; those with larger radii are "outer ν_π" events.

Train Setting (GeV/c)	Energy Bin	N_{LE}^{data}	N_{WB}^{data}
+100	Inner ν_π	1413	1656
+100	Outer ν_π	1816	2072
+100	ν_k	640	686
+140	Inner ν_π	2922	3024
+140	Outer ν_π	2975	3075
+140	ν_k	1730	1670
+165	Inner ν_π	2283	2543
+165	Outer ν_π	1946	2258
+165	ν_k	1532	1826
+200	Inner ν_π	3402	3470
+200	Outer ν_π	2347	2521
+200	ν_k	2800	2876
+250	Inner ν_π	2278	2235
+250	Outer ν_π	1318	1441
+250	ν_k	2720	2678
-165	Inner ν_π	2068	2131
-165	Outer ν_π	1886	2104
-165	ν_k	654	723

Table V.7: The relative livetimes for the fast spill, ping gates, and combined (fast+ping) data sets are given for each secondary momentum setting.

Train Setting (GeV/c)	Fast Spill	Ping Gates	Combined
+100	1.098	1.037	1.067
+140	1.035	0.979	1.001
+165	1.147	-----	1.147
+200	1.091	1.014	1.067
+250	1.075	1.014	1.058
-165	1.079	-----	1.079

The second normalization correction was necessitated by the deadtimes of the front Veto counters in each detector. These deadtimes led to inefficiencies in the muon trigger which were different for each detector. This effect was corrected for by using the efficiency triggers (Trigger 4; p. 77). The quantity:

$$\varepsilon_n = 1 - (BT4)_n/(BT14)_n$$

gives the efficiency for detector number n, where BT4 denotes the number of efficiency triggers, BT14 is the number of simultaneous efficiency and muon triggers, and n equals 1(2) for the Lab E (Wonder Bldg.) detector. The correction factors thus obtained are shown in Table V.8, together with the systematic errors. The systematic error was calculated using blind scalers which counted the number of partial triggers: T1, T1·Veto delayed, and the clock during the livetime. The difference between the two techniques gave the systematic error.

Table V.8: Shown are the veto-deadtimes (with the systematic errors) for the two detectors at each train setting. The correction to the normalization is also given.

Train Setting (GeV/c)	Veto-Deadtime (LE)	Veto-Deadtime (WB)	Correction Factor	Total Corr.
+100	1.000 ± .004	0.984 ± .008	0.984 ± .010	1.0144
+140	0.997 ± .002	0.991 ± .002	0.995 ± .003	0.9617
+165	0.996 ± .005	0.980 ± .004	0.984 ± .006	1.0900
+200	0.995 ± .002	0.989 ± .002	0.993 ± .003	1.0239
+250	0.992 ± .002	0.984 ± .004	0.991 ± .005	1.0136
-165	0.990 ± .003	0.987 ± .004	0.997 ± .005	1.0316

Table V.9: The event ratios (corrected for reconstruction inefficiencies and relative detector normalizations), the Monte Carlo event ratios (both Turtle and Ad Hoc), and the correction due to the wide band background (WBB) are given. The effects of the WBB and the finite size of the beam must be taken into account before any comparison is made with ν oscillation hypotheses.

Train Setting (GeV/c)	Energy Bin	R_{data}	R_{MC} (TURTLE/ Ad Hoc)	R_{WBB}
+100	Inner ν_π	0.986±.034	1.013 ± .008 1.013 ± .008	1.007
	Outer ν_π	1.019±.031	1.000 ± .008 1.000 ± .008	1.005
	ν_k	1.003±.054	0.964 ± .011 0.964 ± .011	1.001
+140	Inner ν_π	0.974±.025	1.022 ± .007 1.027 ± .007	1.004
	Outer ν_π	1.017±.025	1.025 ± .008 1.032 ± .008	1.004
	ν_k	0.999±.034	0.974 ± .008 0.990 ± .008	1.000
+165	Inner ν_π	1.022±.032	1.001 ± .006 1.032 ± .006	1.004
	Outer ν_π	0.993±.033	1.027 ± .008 1.025 ± .008	1.004
	ν_k	0.935±.035	0.974 ± .007 0.959 ± .006	1.000
+200	Inner ν_π	1.046±.025	1.022 ± .006 1.032 ± .006	1.005
	Outer ν_π	1.011±.028	1.014 ± .008 1.021 ± .008	1.007
	ν_k	0.994±.026	0.974 ± .005 0.984 ± .005	1.000
+250	Inner ν_π	1.059±.030	1.023 ± .005 1.035 ± .005	1.008
	Outer ν_π	0.985±.037	1.004 ± .009 1.015 ± .009	1.011
	ν_k	1.021±.027	0.992 ± .005 0.996 ± .005	1.001
-165	Inner ν_π	1.026±.032	1.007 ± .005 1.032 ± .006	1.001
	Outer ν_π	0.949±.031	1.007 ± .006 1.025 ± .008	1.006
	ν_k	0.920±.050	0.975 ± .010 0.959 ± .006	1.000

The final normalization factor was due to the slightly different target mass densities in the two detectors. The Wonder Bldg. calorimeter was less dense than that in Lab E due to the different spark chamber spacing. There were also small effects, such as the presence of the water bags which helped to balance the pressure of the Lab E liquid scintillation counters. The correction factor and associated systematic error are 1.036 ± .007.

Table V.9 shows the total normalization correction, the final corrected event ratios, and the ratios for the Monte Carlo events. These data are plotted in Figs. V.13-16. The energy calculated using the beam and detector Monte Carlo programs is used to plot the points and to test ν oscillation hypotheses. As is evident in the figures and table, the event ratios predicted by the Monte Carlo are not equal to unity. This reflects a confluence of several competing effects - the angular divergence of the beam, the experimental decay of the secondary hadron beam along the decay pipe, and the differing solid angles subtended by the two detectors from different points along the decay pipe.

Figure V.13: Shown are the event ratios for the 15 ν energy bins after the normalization correction.

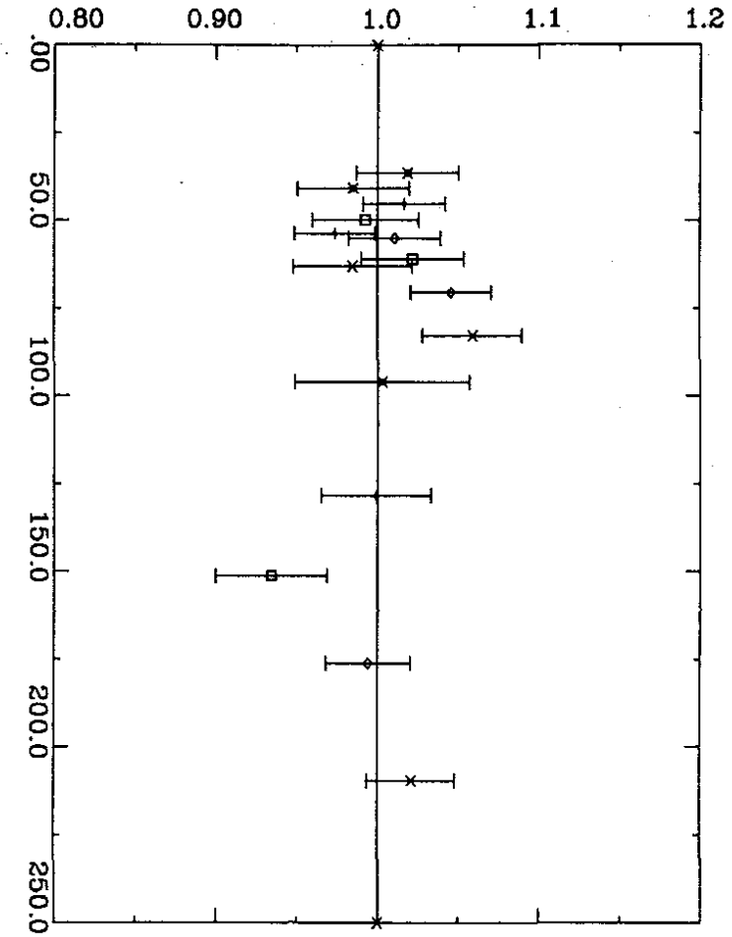

Figure V.14: Shown are the event ratios for the 3 $\bar{\nu}$ energy bins after the normalization correction.

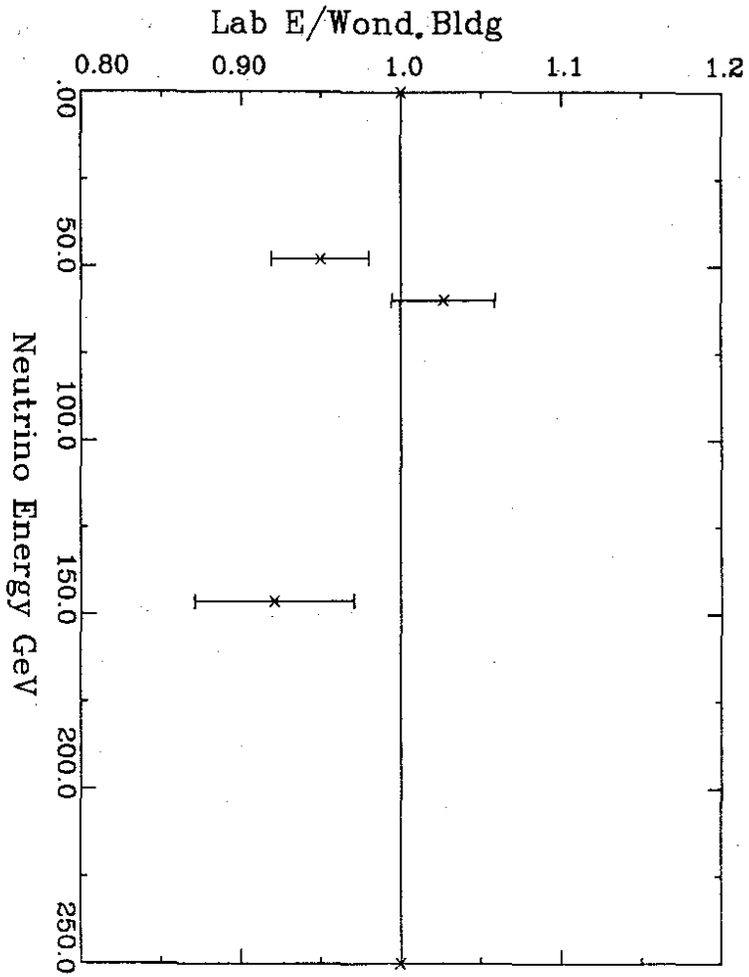

Figure V.15: Shown are the Monte Carlo event ratios for the ν flux files. These events are used to correct the data for effects which are due to the finite size of the ν beam (cf. Chapter VI).

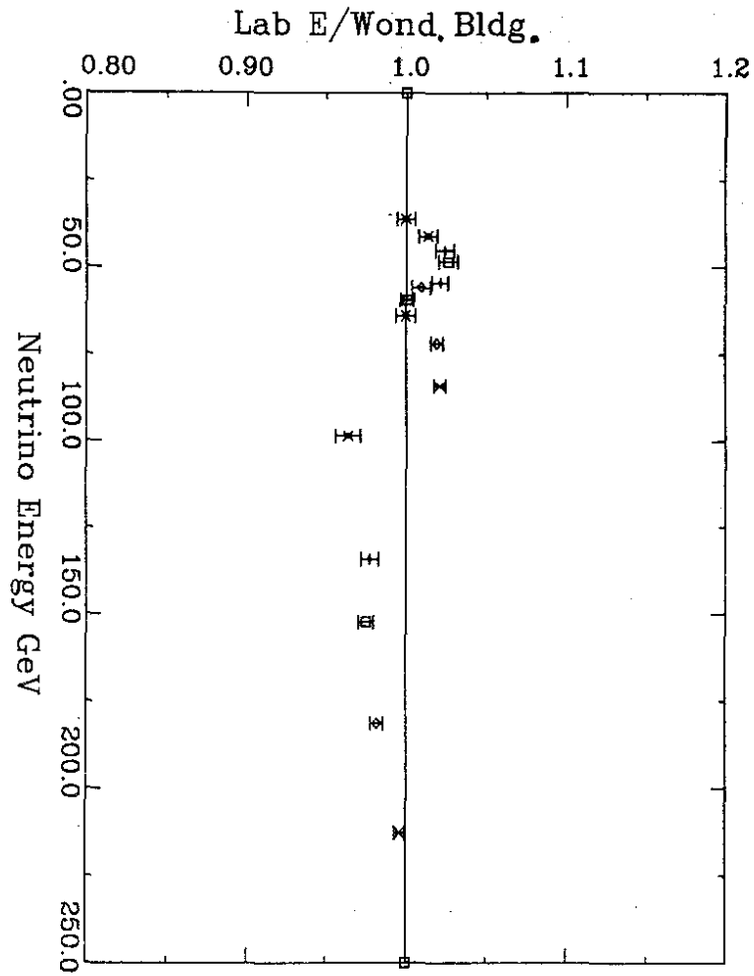

Figure V.16: Shown are the Monte Carlo event ratios for the $\bar{\nu}$ flux files. These events are used to correct the data for effects which are due to the finite size of the ν beam (cf. Chapter VI).

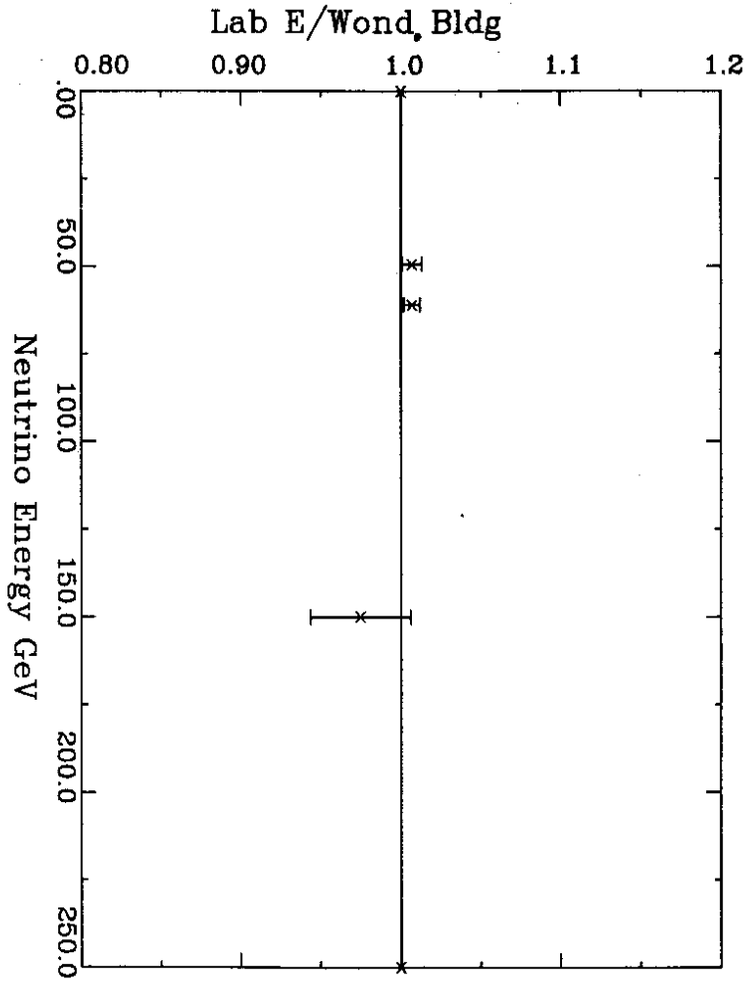

The effects due to the finite size of the beam may be understood by considering Fig. V.8. The data was analysed under the assumption that all neutrinos originated at the centre of the decay pipe. If this assumption was false, and all neutrinos originated at the entrance of the decay pipe, then the event ratios would be larger than unity (cf. dotted line in Fig. V.8). Contriwise, if all neutrinos originated at the end of the decay pipe, the ratios would be less than unity.

The angular divergence of the beam was approximately 0.2 mr. If the decay kinematics of the parent mesons gave no contribution to the ν angle, then the neutrino beam would be seen to be originating from the decay pipe entrance. If the angle due to the decay was much larger than the angular divergence, then no effect would be expected. The mean decay angles for ν_π and ν_k Monte Carlo events are shown in Table V.10 for each train setting. The mean decay angles for the ν_π events is comparable to the angular divergence; thus the ν_π event ratios were expected to be larger than unity. The large decay angles of the ν_k events wash out the effect for those bins.

Table V.10: The mean decay angles for ν_π and ν_k Monte Carlo events are given.

Train Setting (GeV/c)	$\langle\theta\rangle_\pi$ (mrad)	$\langle\theta\rangle_k$ (mrad)
+100	.697	.687
+140	.596	.661
+165	.561	.658
+200	.487	.640
+250	.422	.615

The exponential decay of mesons in the decay pipe made the neutrinos appear to originate closer to the upstream end of the decay pipe. This was most important for ν_k events (due to the short kaon lifetime), and is the reason that the Monte Carlo event ratios for those bins were less than unity. The solid angle effects also tended to make the event ratios less than one.

The TURTLE Monte Carlo corrections are shown in Figs. V.15,16, and 19. The event ratios divided by the TURTLE event ratios are shown in Figs. V.17-19 (the numbers are given in Table V.11). For no oscillations this quantity should be unity. The χ^2 for this hypothesis is given in Table V.11 for the ν and $\bar{\nu}$ data separately, and then combined. The χ^2 calculation is described in detail below (cf. Ch. VI).

Table V.11: The event ratios for the data corrected for the effects due to the finite size of the beam are given. This quantity should be unity for the case of no ν oscillations.

Train Setting (GeV/c)	Energy Bin	Energy (GeV)	σ_E (GeV)	R_{final}
+100	Inner ν_π	40.76	5.17	0.966 ± .034
	Outer ν_π	36.42	5.29	1.014 ± .032
	ν_k	96.08	10.90	1.039 ± .057
+140	Inner ν_π	53.62	7.79	0.949 ± .025
	Outer ν_π	45.20	7.39	0.988 ± .026
	ν_k	128.50	14.78	1.026 ± .036
+165	Inner ν_π	61.01	9.19	1.017 ± .032
	Outer ν_π	49.78	10.18	0.963 ± .033
	ν_k	151.28	16.90	0.959 ± .036
+200	Inner ν_π	70.51	12.06	1.018 ± .025
	Outer ν_π	55.05	13.18	0.990 ± .029
	ν_k	176.25	19.70	1.021 ± .027
+250	Inner ν_π	82.86	16.15	1.027 ± .030
	Outer ν_π	63.00	19.41	0.971 ± .037
	ν_k	209.60	24.02	1.028 ± .028
-165	Inner ν_π	61.06	8.71	1.019 ± .032
	Outer ν_π	49.46	9.26	0.938 ± .031
	ν_k	150.18	16.64	0.945 ± .060

Figure V.17: Shown are the 15 ν data points corrected for the effects due to the finite size of the ν beam.

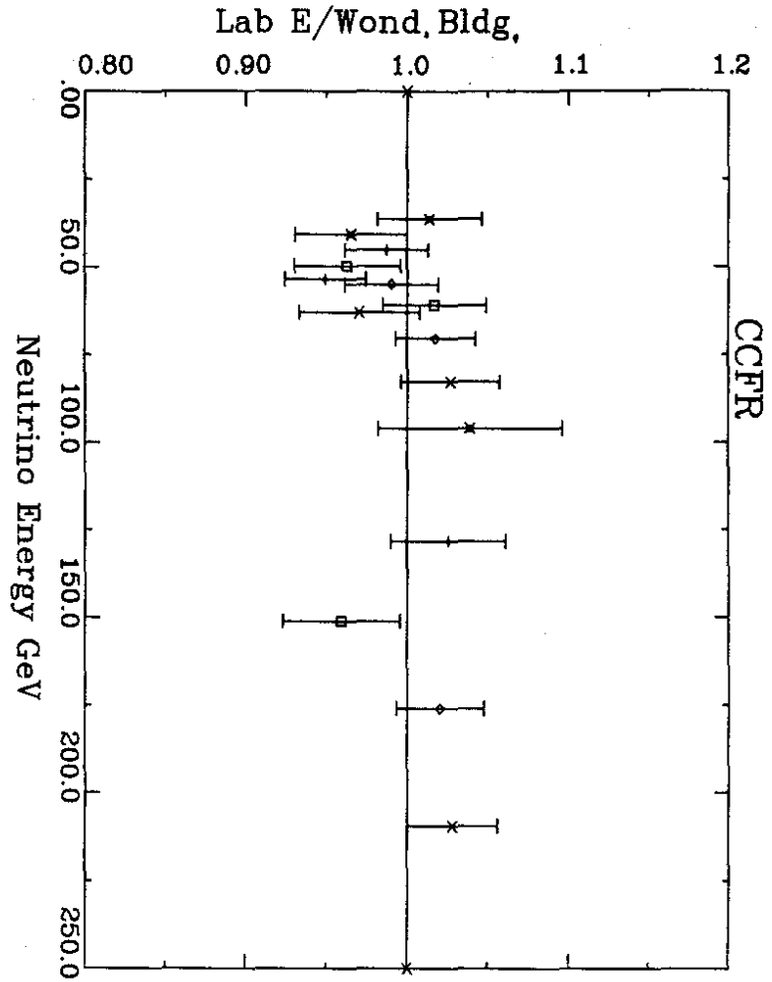

Figure V.18: Shown are the 3 $\bar{\nu}$ data points corrected for the effects due to the finite size of the $\bar{\nu}$ beam.

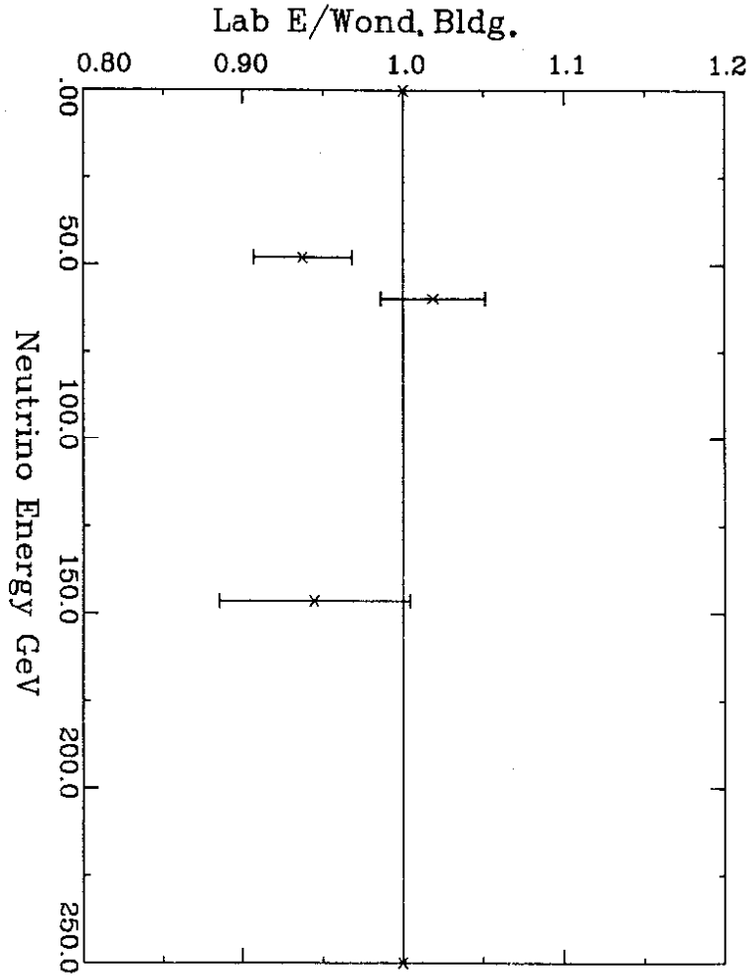

Figure V.19: Shown for the combined ($\nu+\bar{\nu}$) data set are the (a) Monte Carlo event ratios, and the (b) data event ratios corrected for the finite size of the ν beam.

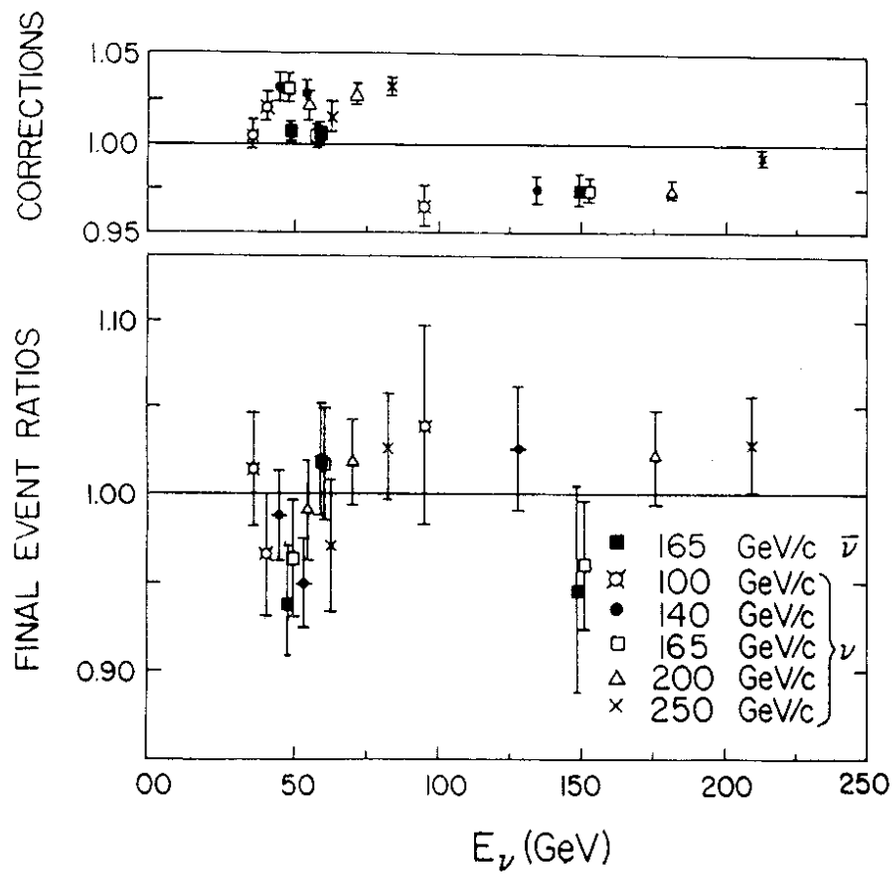

Table V.12: The values of χ^2 for the ν, $\bar{\nu}$, and $(\nu+\bar{\nu})$ data sets for the hypothesis of no ν oscillations are given. The details of the χ^2 calculation are given in Chapter VI.

Data Set	(χ^2) - no ν oscillations
ν	11.04
$\bar{\nu}$	4.72
$(\nu+\bar{\nu})$	15.76

CHAPTER VI

Results and Conclusions

The final step in the data analysis is to use the measured event ratios and the Monte Carlo simulation programs which predict event ratios for our experiment to test neutrino oscillation hypotheses. This is done within the framework of the two-component ν mixing model. It is first necessary to calculate a χ^2 as a function of Δm^2 and $\sin^2 2\theta$. A statistical test is then applied to the χ^2 at each point in the $(\Delta m^2, \sin^2 2\theta)$ plane to determine if that point is excluded at the 90 % Confidence Level (C.L.). In this parameter space the line, $\sin^2 2\theta = 0$, corresponds to the hypothesis of no ν oscillations.

This procedure is described in detail below. Following that discussion, these results are compared to other

oscillation experiments; and general comments regarding the present status of neutrino mass measurements are made.

Section VI.1: Calculation of the Limit

Section VI.1.1: Calculation of χ^2

The form of χ^2 as a function of Δm^2 and $\sin^2 2\theta$ is given by:

$$\chi^2 = \sum_{i=1}^{N} \sum_{j=1}^{3} \frac{(R_{ij}^{meas} - f_i^{norm} R_{ij}^{MC}(\Delta m^2, \sin^2 2\theta))^2}{\sigma_{ij}^2} + \sum_{i=1}^{N} \frac{(f_i^{norm} - 1)^2}{(\sigma_{norm}^i)^2} \qquad (1)$$

The measured event ratio is denoted by R_{ij}^{meas}, while σ_{ij} is the statistical error on that ratio. The number of train settings is given by N; N may take the values 1, 5, or 6 for the $\bar{\nu}$, ν, and $(\nu+\bar{\nu})$ data sets, respectively. The systematic error on the normalization is given by σ_{norm}^i. This accounts for the possible effects of the relative target densities, veto-deadtimes, livetime corrections, etc. on the event ratios. The systematic error is assigned on a train setting - by - train setting (not point-by-point) basis, since any normalization error affects all 3 points at that setting

identically. The systematic error is incorporated into the χ^2 via the factor f_i^{norm}. Finally, the predicted ratio for a particular oscillation hypothesis is given by R_{ij}^{MC}.

The factor f_i^{norm} takes account of a possible systematic shift in R_{ij}^{meas} away from the predicted value, R_{ij}^{MC}. The factors were calculated by minimising χ^2 with respect to each f_i^{norm} in turn; the equations:

$$\frac{\partial \chi_1^2}{\partial f_i^{norm}} = 0$$

were solved for each f_i^{norm}. The variable $\chi^2{}_1$ denotes the χ^2 of equation (1) without the second (normalization) term. The values of f_i^{norm} ranged from approximatedly .995 to 1.005.

The predicted event ratios, R_{ij}^{MC}, were calculated using each of the beam simulations (that is, the TURTLE and Ad Hoc models). The effects of oscillation hypotheses were factored in by giving each generated neutrino weights, W_{det}^k, at each detector. The W_{det} were directly related to the oscillation probability. The neutrino "interactions" at the detectors were then passed through the standard analysis package (exactly as for the no oscillation case), and summed counting each event k as W_{det}^k instead of unity.

The result of this procedure was 6 χ^2-grids, 3 pertaining to each of the two beam simulations. The 3 grids were for the ν data (15 points), $\bar{\nu}$ data (3 points), and the $(\nu+\bar{\nu})$ data (18 points) sets.

The values of $\sin^2 2\theta$ and Δm^2 which give the minimum χ^2, along with that χ^2, are given in Table VI.1 for each of the six grids. The hypothesis giving the minimum χ^2 for the Monte Carlos are superimposed on the data in Figs. VI.1-3.

Table VI.1: Shown are the hypotheses giving the lowest χ^2 for each of the 3 data sets (ν, $\bar{\nu}$, and ($\nu+\bar{\nu}$)) obtained using each of the two Monte Carlos (TURTLE and Ad Hoc).

Data Set	Monte Carlo	Δm^2 (eV^2/c^4)	$\sin^2 2\theta$	χ^2_{min}
ν	TURTLE	1252	0.55	9.04
ν	Ad Hoc	42	0.06	6.38
$\bar{\nu}$	TURTLE	132	0.16	0.23
$\bar{\nu}$	Ad Hoc	132	0.16	0.26
($\nu+\bar{\nu}$)	TURTLE	1252	0.61	12.54
($\nu+\bar{\nu}$)	Ad Hoc	10	0.43	8.75

Figure VI.1: The 15 ν event ratios, corrected for relative normalizations and the effects of the finite beam size, are shown with a typical ν oscillation prediction for the ν data set (using the TURTLE Monte Carlo).

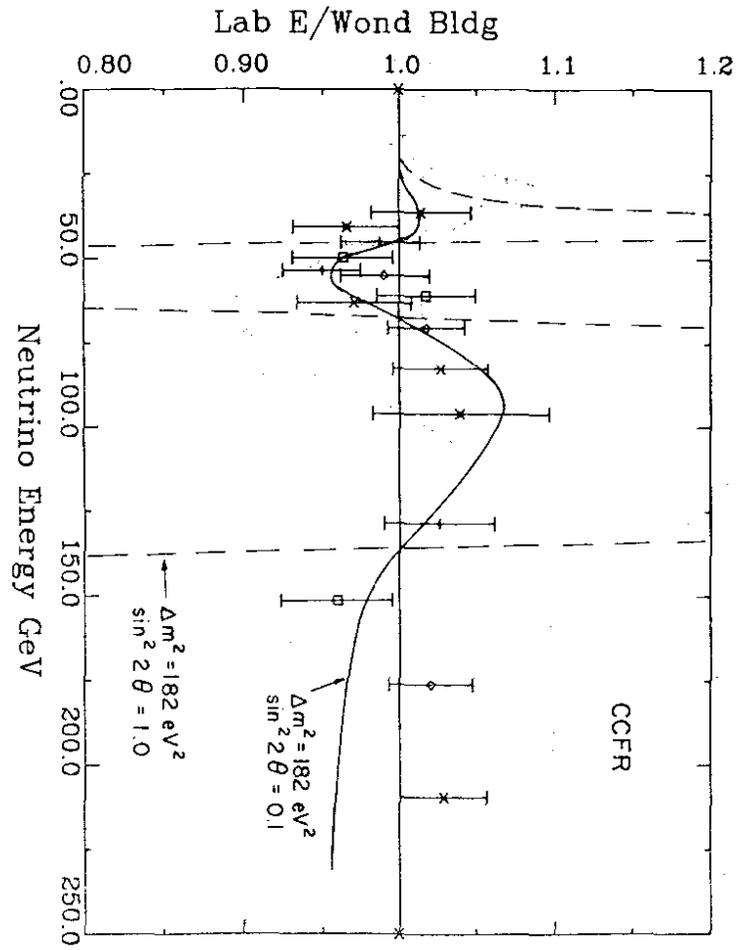

Figure VI.2: The 3 $\bar{\nu}$ event ratios, corrected for relative normalizations and the effects of the finite size of the beam, are shown with the ν oscillation prediction giving the lowest χ^2 for the ν data set (using the TURTLE Monte Carlo). The parameters are given in Table VI.1.

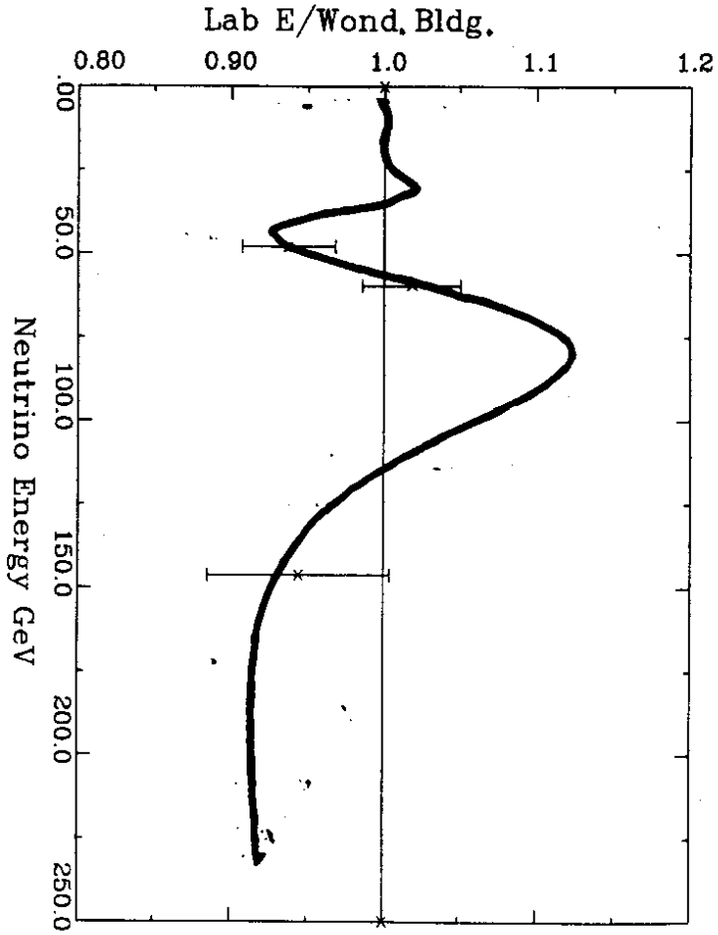

Figure VI.3: The 18 $(\nu+\bar{\nu})$ event ratios, corrected for relative normalizations and the effects of the finite size of the beam, are shown with the ν oscillation prediction giving the lowest χ^2 for the ν data set (using the TURTLE Monte Carlo). The parameters are given in Table VI.1.

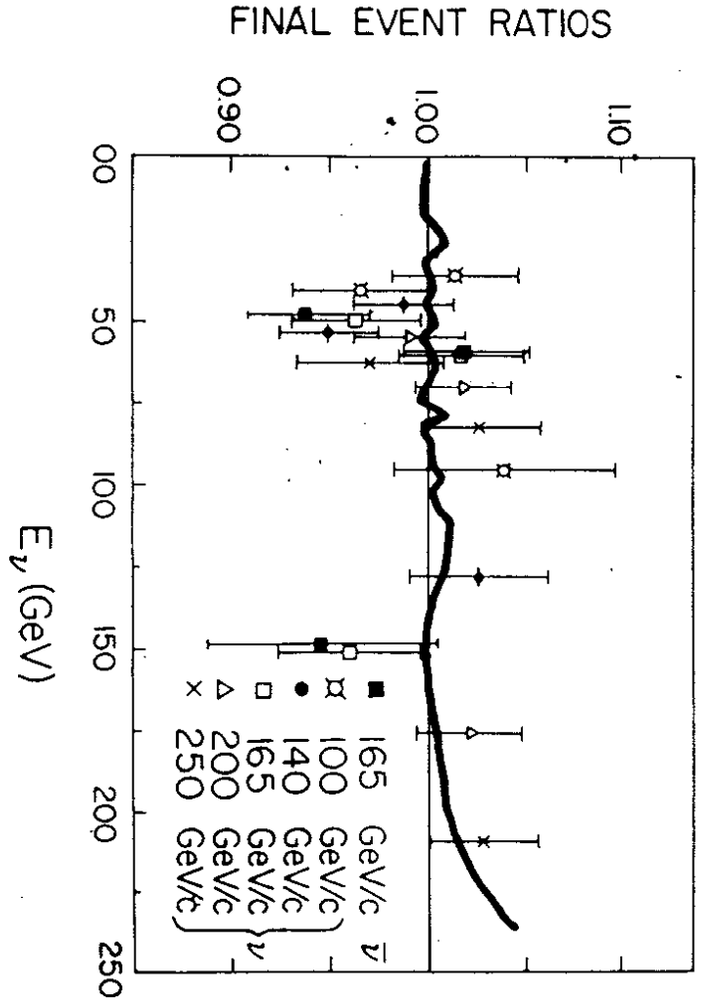

Section VI.1.2: Likelihood Ratio Test

Having found that the data were consistent with the absence of neutrino oscillations, it remained to obtain 90 % C.L. limits on possible oscillations. The definition of the term "90 % C.L. limit" will first be given, followed by a rationale for using the Likelihood Ratio test to obtain this limit. The details of the test's implementation will then be discussed, culminating in the presentation of correlated limits in the $(\Delta m^2, \sin^2 2\theta)$ parameter space, S, obtained from the ν, $\bar{\nu}$, and $(\nu+\bar{\nu})$ data sets.

The 90 % C.L. limit is defined as that statistical test which, when applied to a data set resulting from some true hypothesis, will reject that hypothesis in less than 10 % of experiments performed. In other words, if the neutrino mixing is accurately described by a two component hypothesis with parameters $P_0 = (\Delta m^2{}_0, \sin^2 2\theta_0)$, then the test should reject P_0 in at most 10 experiments out of every 100 performed.

The Likelihood Ratio test[57,68] is a statistical test applied using the test statistic:

$$\lambda = \frac{L(\underline{x}|P_1)}{\max\limits_{P \in S} L(\underline{x}|P)} \qquad (2)$$

Here, P_1 is a point $(\Delta m_1^2, \sin^2 2\theta_1)$ in the parameter space S.

The set of N observations (the event ratios in our case) is given by the array $\underline{x}$. An element of this set is denoted as x_i. The likelihood function is defined as:

$$L(\underline{x}|P) = \prod_{i=1}^{N} f(x_i|P) \qquad (3)$$

The function f gives the probability of observing the point x_i given the hypothesis $P \in S$. If x_i is Gaussian-distributed, then f may be written as:[69]

$$f(x_i|P) = \frac{1}{\sqrt{2\pi}\,\sigma_i} \exp\left(-(x_i-\alpha_i)^2/2\sigma_i^2\right) \qquad (4)$$

where α_i is the data point predicted by using P and σ_i is the error on the measurement of x_i. The likelihood is then given by:

$$L(\underline{x}|P) = \prod_{i=1}^{N} \frac{1}{\sqrt{2\pi}\,\sigma_i} \exp\left(-(x_i-\alpha_i)^2/2\sigma_i^2\right) \qquad (5)$$

The argument of the exponential is similar in form to the term in the first sum of our expression for χ^2 (equation (1)). Noting this, we define the variable χ_i^2 so that equation (5) becomes:

$$L(\underline{x}|P) = \prod_{i=1}^{N} \frac{1}{\sqrt{2\pi}\,\sigma_i} \exp(-\chi_i^2/2) \qquad (6)$$

We will see that the natural logarithm of the likelihood is a useful quantity. For that reason we give it below:

$$\ln L(\underline{x}|P) := -\frac{1}{2}\sum_{i=1}^{N} \chi_i^2 + \text{constant} \qquad (7)$$

Returning to the likelihood ratio, λ, we see that it may fall between 0 and 1. A value of 1 for a hypothesis P_1 indicates a high probability relative to the other points in the parameter space; on the other hand, a value near 0 indicates a very low probability. This variable thus appears to be useful in rejecting or accepting hypotheses. It is important to note that this test statistic is only defined within a specified parameter space. In our case, that space is the set of all two component neutrino mixings. Any test using this test statistic will only be valid in that space. Practically, this means that the Likelihood Ratio test will test a specific 2 neutrino mixing hypothesis against all other 2 component mixings. It will <u>not</u> test against other hypotheses, such as 3-component mixings, combinations of mixing and neutrino decays, etc.

We want to use λ to obtain a 90 % C.L. limit. This means the test will reject hypotheses when:

$$0 < \lambda < \lambda_c \tag{8}$$

The cut, λ_c, is defined so that:

$$0.10 = \int_0^{\lambda_c} g(\lambda \mid P_0) \cdot d\lambda$$

where g is the probability that a hypothesis P_0 will give a likelihood ratio λ. For our problem, the value of λ_c will

have to be obtained through a Monte Carlo calculation. This calculation, which obtains a probability distribution by simulating our experiment many times, is described below (cf. p. 215).

It can be shown[70] that the distribution of $-2 \cdot \ln\lambda$ is distributed like a χ^2 with N' degrees of freedom, where N' = N (the number of data points) - 2 (the number of dimensions of the parameter space). Using equations (2) and (7), we obtain for this quantity:

$$\Delta\chi^2 = -2 \cdot \ln\lambda = \sum_{i=1}^{N} \chi_i^2(P_1) - \sum_{i=1}^{N} \chi_i^2(P_{min})$$

Recalling that we have generalized our definition of the χ^2 to include the systematic normalization error, we get:

$$\Delta\chi^2 = \chi^2(\Delta m^2, \sin^2 2\theta) - \chi^2_{min} \tag{9}$$

The minimum χ^2 is called χ^2_{min}. Writing equation (8) in terms of χ^2 instead of λ, we exclude oscillations at the 90 % C.L. for:

$$\Delta\chi^2_c < \Delta\chi^2 < \infty \tag{10}$$

In order to use this test, the value of $\Delta\chi^2_c$ must be determined. The procedure for doing this is outlined below for the analysis of the ν data alone. The application of the method to the $\bar{\nu}$ and $(\nu+\bar{\nu})$ data sets is similar.

The 90 % C.L. limit, $\Delta\chi^2_c$ is obtained by doing many (1000-2000) Monte Carlo simulations of the experiment. The Monte Carlo reads in the mean energies of each of the 15 energy bins, together with the statistical error associated with that bin. For several points in the parameter space (most at values of $\sin^2 2\theta$ below 0.10), the prediction for the event ratio in each of the 15 bins is calculated. The prediction for a bin is then smeared by using a Gaussian random number generator and the statistical error for that bin. A χ^2 is calculated, comparing the prediction to the "true" value. For each of the 1000-2000 "experiments", 3 histograms are incremented; these are for χ^2, χ^2_{min}, and $Wx2 = (\chi^2 - \chi^2_{min})$. The value of $\Delta\chi^2_c$ is chosen to delineate the upper 10 % of the area in the $\Delta\chi^2$ histogram.

Figure VI.4: The histograms below show distributions of χ^2, χ^2_{min}, and $\Delta\chi^2$ for 15 degrees of freedom (ν data set). These histograms were generated assuming $\Delta m^2 = 602$ eV^2 and $\sin^2 2\theta = .04$.

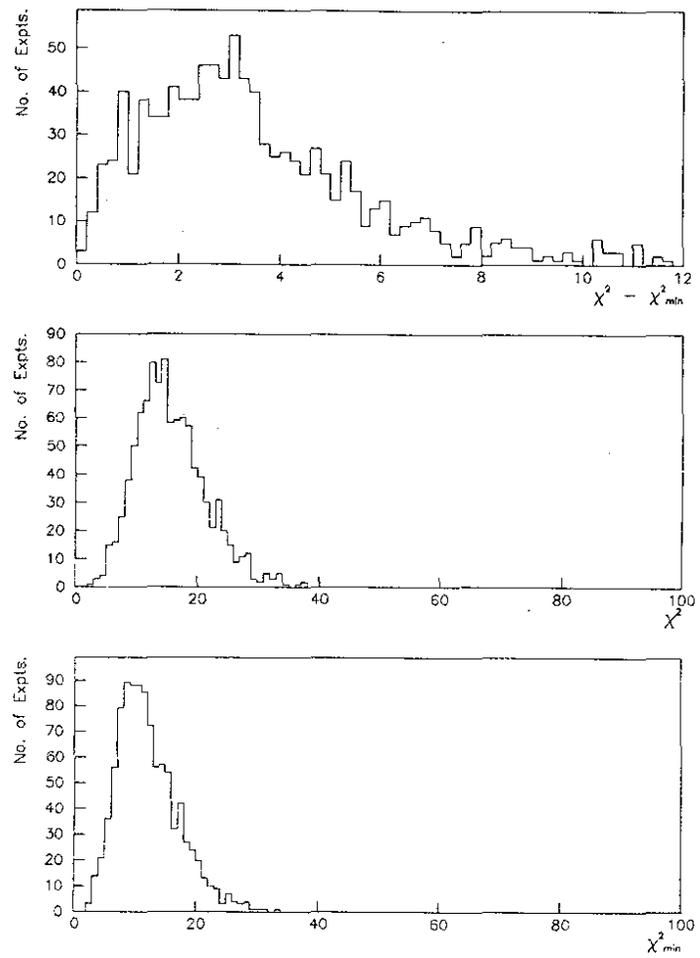

Figure VI.5: The histograms below show distributions of χ^2, χ^2_{min}, and $\Delta\chi^2$ for 3 degrees of freedom ($\bar{\nu}$ data set). These histograms were generated assuming $\Delta m^2 = 162$ eV^2 and $\sin^2 2\theta = .04$.

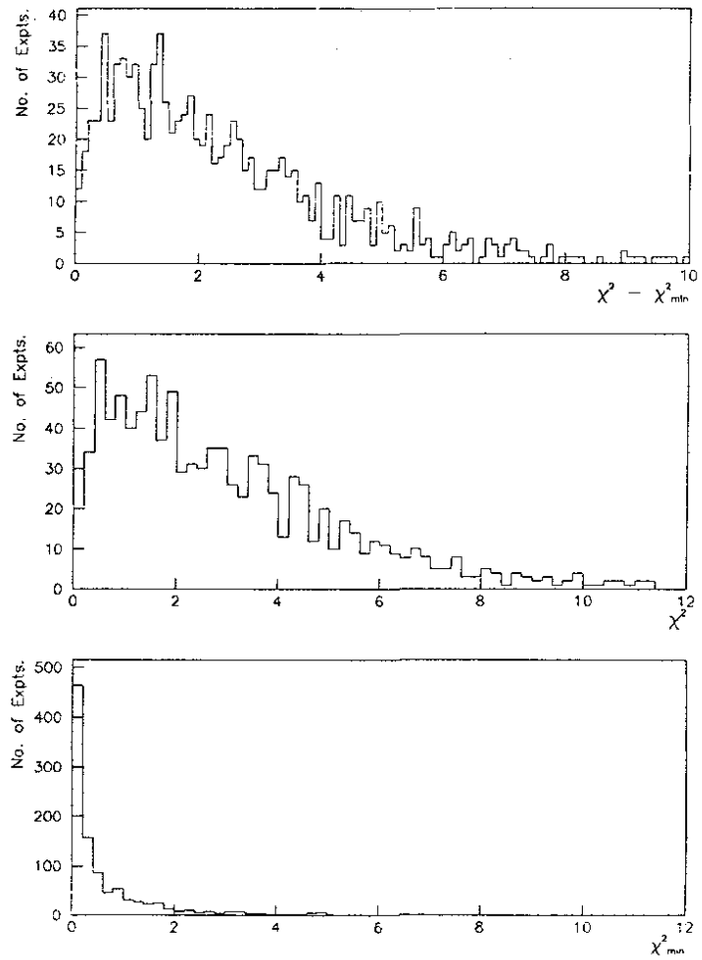

Figure VI.6: The histograms below show distributions of χ^2, χ^2_{min}, and $\Delta\chi^2$ for 18 degrees of freedom ($(\nu+\bar{\nu})$ data set). These histograms were generated assuming $\Delta m^2 = 162$ eV^2 and $\sin^2 2\theta = .04$.

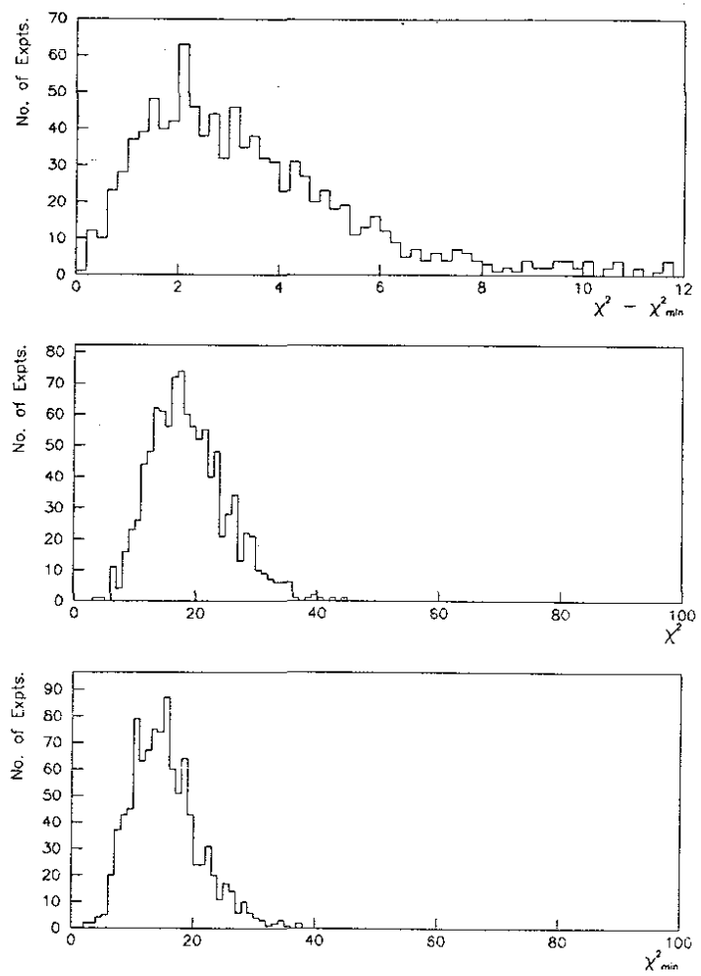

Table VI.2: Values for $\Delta\chi^2$ are given at selected points in the $(\Delta m^2, \sin^2 2\theta)$ parameter space. These are calculated for the ν data using the Monte Carlo techniques described on p. 215.

Δm^2 (eV^2/c^4)	$\sin^2 2\theta$	$\Delta\chi^2_c$	$\Delta\chi^2_c+\chi^2_{min}$	$\chi^2_{Pearson}$
----	0.00	6.6	15.6	22.3
102	0.02	6.3	15.3	22.3
162	0.04	6.3	15.3	22.3
162	0.10	4.5	13.5	22.3
162	0.26	3.5	11.5	22.3
302	0.04	6.4	15.4	22.3
302	0.10	5.3	14.3	22.3
302	0.26	4.9	13.9	22.3
902	0.04	6.5	15.5	22.3
902	0.10	6.5	15.5	22.3
902	0.26	5.9	14.9	22.3
1252	0.30	5.5	14.5	22.3

Table VI.3: Values of $\Delta\chi^2_c$ calculated for the $\bar{\nu}$ data set.

Δm^2 (eV^2/c^4)	$\sin^2 2\theta$	$\Delta\chi^2_c$	$\Delta\chi^2_c+\chi^2_{min}$	$\chi^2_{Pearson}$
90	0.04	5.17	5.40	6.25
90	0.10	5.13	5.36	6.25
90	0.26	5.00	5.23	6.25
162	0.04	4.95	5.18	6.25
162	0.10	5.21	5.44	6.25
162	0.26	4.55	4.78	6.25
302	0.04	4.60	4.83	6.25
302	0.10	4.47	4.70	6.25
302	0.26	4.33	4.58	6.25
902	0.04	5.00	5.23	6.25
902	0.10	5.01	5.24	6.25
902	0.26	4.86	5.09	6.25

Table VI.4: Values of $\Delta\chi^2_c$ calculated for the $(\nu+\bar{\nu})$ data set.

Δm^2 (eV^2/c^4)	$\sin^2 2\theta$	$\Delta\chi^2_c$	$\Delta\chi^2_c+\chi^2_{min}$	$\chi^2_{Pearson}$
---	0.00	6.2	18.7	26.0
90	0.10	5.0	17.5	26.0
162	0.04	6.0	18.5	26.0
162	0.10	6.3	18.9	26.0
162	0.26	3.0	15.5	26.0
602	0.04	6.4	19.0	26.0
602	0.10	5.0	17.5	26.0

The 3 histograms resulting from this procedure are shown for sample points in Figs. VI.4,5, and 6 for the ν, $\bar{\nu}$, and $(\nu+\bar{\nu})$ data sets, respectively.[71,72,73] Tables VI.2-4 show the values of $\Delta\chi^2_c$ calculated for different points in S for the three data sets. Also shown in that table is the value of $(\Delta\chi^2_c + \chi^2_{min})$ for each of the Monte Carlos; this is the χ^2 which defines the 90 % C.L. on the grids in Appendix B.

The limit curves are given by the solid curves in Figs. VI.7, 8, and 9. These are obtained by first finding the limit curve for each Monte Carlo, and then, at each value of Δm^2, choosing the <u>least restrictive</u> limit. This allows for the uncertainty in our knowledge of the neutrino beam.

Figure VI.7: Shown are the 90 % C.L. limits on the oscillation $\nu_\mu \to \nu_x$ obtained using the Likelihood Ratio test (solid curve) and Pearson' χ^2 test (dotted curve).

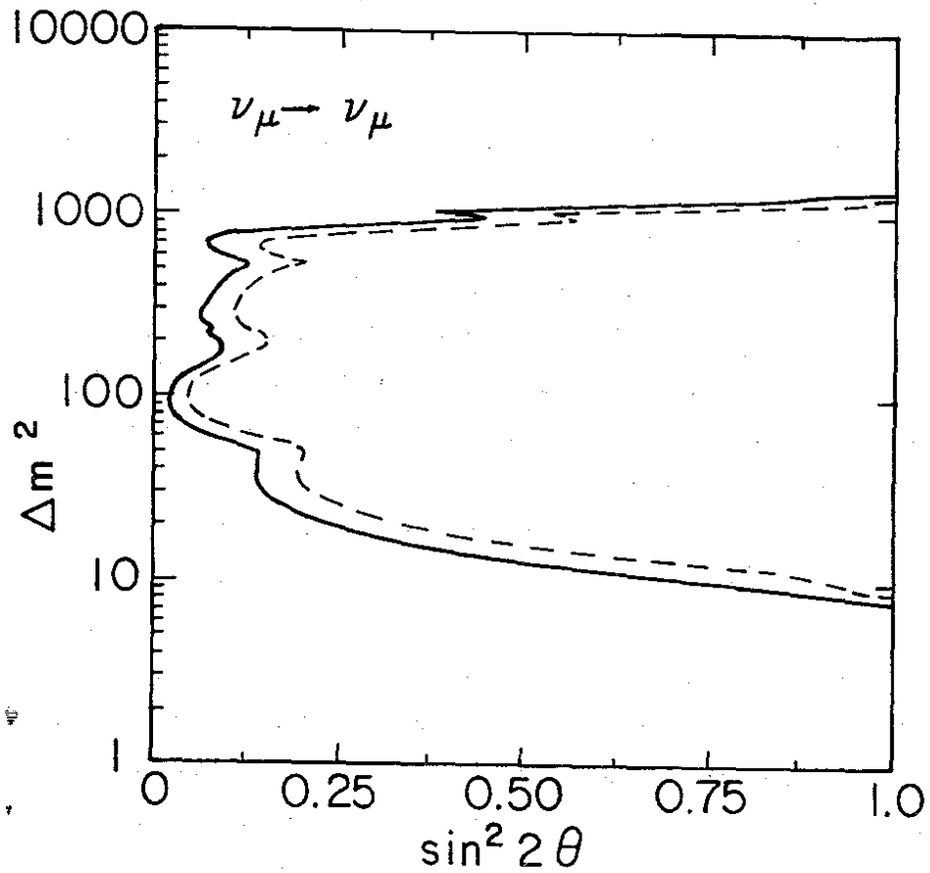

Figure VI.8: Shown are the 90 % C.L. limits on the oscillation $\bar{\nu}_\mu \to \bar{\nu}_x$ obtained using the Likelihood Ratio test (solid curve) and Pearson' χ^2 test (dotted curve).

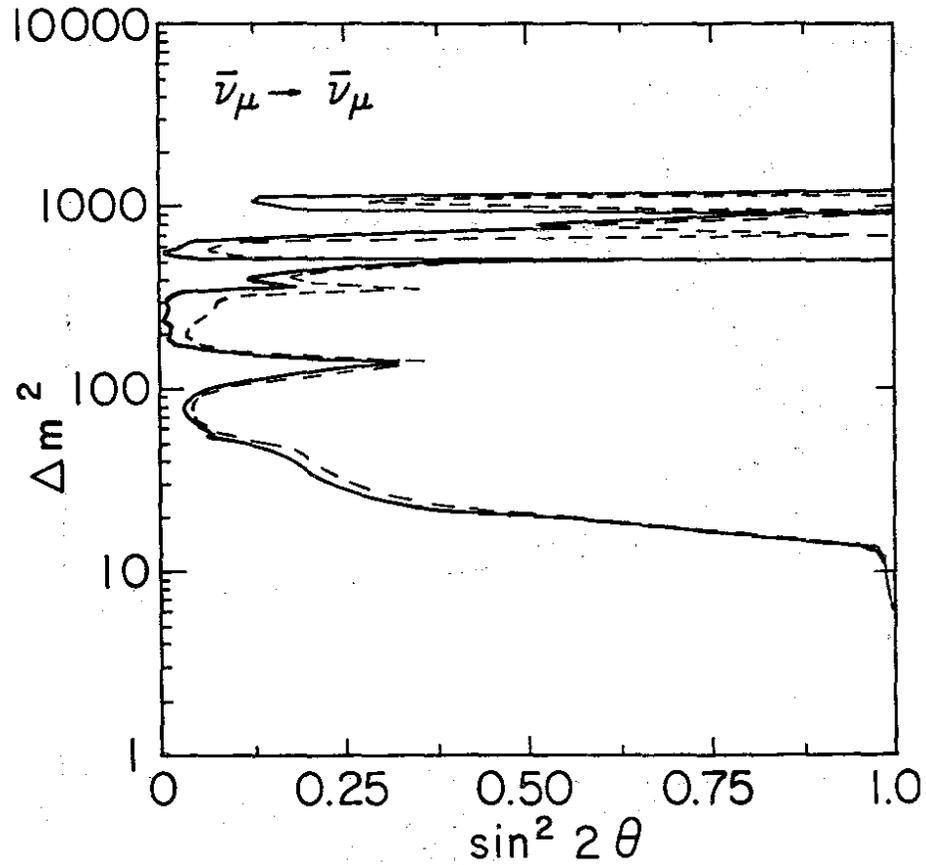

Figure VI.9: Shown are the 90 % C.L. limits on the oscillation $\nu_\mu \to \nu_x$ obtained using the Likelihood Ratio test (solid curve) and Pearson's χ^2 test (dotted curve). Here, CPT conservation has been assumed and the ν and $\bar{\nu}$ data points have been used simultaneously.

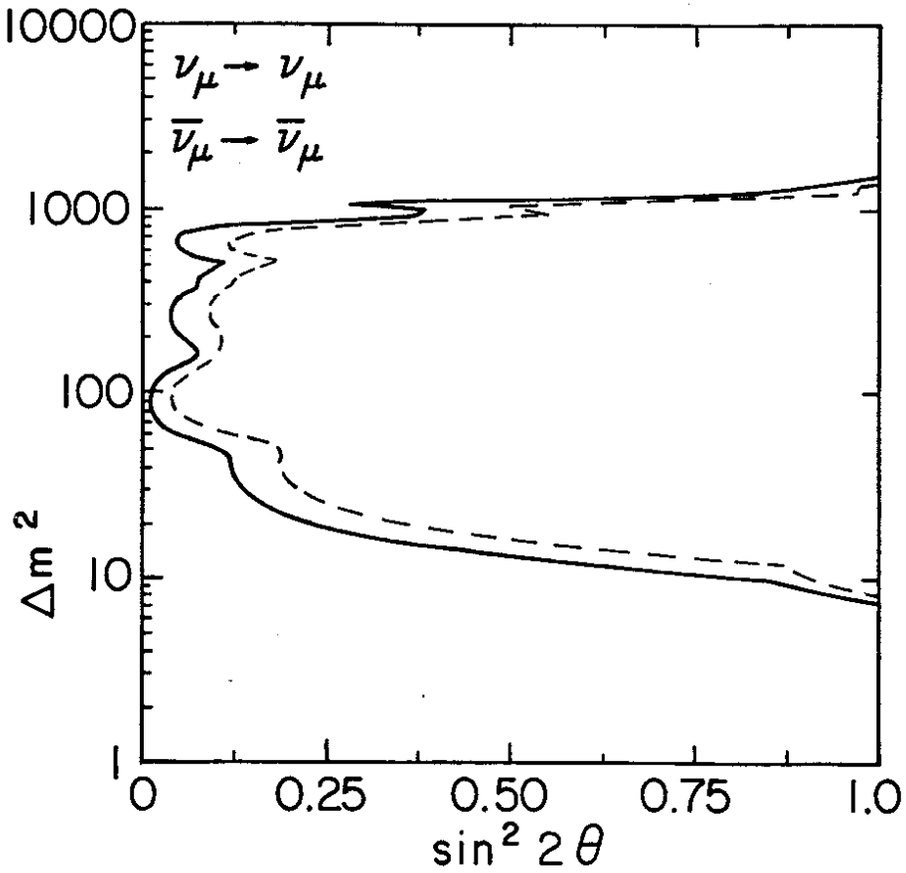

Section VI.1.3: Pearson's χ^2 Test

We also calculated 90 % C.L. limits using Pearson's χ^2 test.[74] This is a "distribution-free" test, as opposed to the Likelihood Ratio test, where we explicitly assumed that the data were described by a two-component mixing hypothesis.

Pearson's χ^2 test uses the χ^2 variable of equation (1) directly as a test statistic (not $(\chi^2-\chi^2_{min})$ as above). The assumption motivating this choice is that the 15 observations of the event ratio belong to 15 mutually exclusive and uncorrelated classes.[75] The prediction for the oscillation is a set of 15 "independent" numbers: R^{MC}_{11}, R^{MC}_{12}, to R^{MC}_{53}. If each of the 15 ratios is Gaussian-distributed, then the hypothesis will be excluded at the 90 % C.L. for $\chi^2 > 22.3$.[75] This is just the 90 % C.L. limit for a Gaussian distribution with 15 degrees of freedom.

Examining Tables VI.2-4, it may be seen that Pearson's χ^2 test has a larger χ^2 cut than the Likelihood Ratio test. This may be understood by considering the distribution-free Pearson's χ^2 test to be effectively a test of a particular two component oscillation hypothesis against all other imaginable hypotheses - N-component mixing ($2 \leq N \leq \infty$), mixing-decay combined hypotheses, etc. These "new"

hypotheses have many degrees of freedom; by including them in the test, the fraction of hypotheses with large χ^2 increases, thus the χ^2_{cut} must be increased. In other words, Pearson's χ^2 test implicitly assumes that the assumption underlying the Likelihood Ratio test is wrong; it assumes that the wrorld is not accurately described by 2 component mixings and so $(\chi^2-\chi^2_{min})$ is not distributed like a χ^2 variable.

Limits obtained using Pearson's χ^2-test are shown in Figs. VI.7-9. As expected, they are less restrictive than the Likelihood Ratio test limits.

Both test mentioned in this section are "correct" under the assumptions given. The criteria for choosing which to quote as the "answer" should then be to give that which is directly comparable to other inclusive neutrino oscillation searches. Unfortunately, there is no universal standard. Experiments searching for inclusive oscillations of $\bar{\nu}_e$ at reactors report both Likelihood Ratio test limits[76] and Pearson's χ^2-test limits.[77] The inclusive ν_μ oscillation experiment at CERN which reports the most restrictive limit at low Δm^2 [78] calculated limits using a one-dimensional parameter space ($\sin^2 2\theta$) at each value of Δm^2.

We have chosen to call the Likelihood Ratio test our

"best" answer. The analysis of this experiment has been done completely within the framework of 2 component mixings; thus the appropriate assumption for the statistical test seems to be the Likelihood Ratio test.

Section VI.2: Summary

Many searches for ν oscillations have been performed recently. Figure VI.8 gives the best current limits on inclusive ν_μ oscillations. The measurement by the CDHS[78] collaboration at CERN extends the CCFR limits described herein down to 0.2 eV^2. The CHARM collaboration[79] reports less restrictive limits than the CDHS results. The CCFR limits on inclusive $\bar{\nu}_\mu$ oscillations are the only reported for that channel (cf. Fig. VI.8).

Figure VI.10: Shown are the limits from the CCFR[72] and CDHS[78] collaborations on inclusive ν_μ oscillations. The CHARM[79] collaboration reports less restrictive results in the same range of Δm^2 as the CDHS measurement.

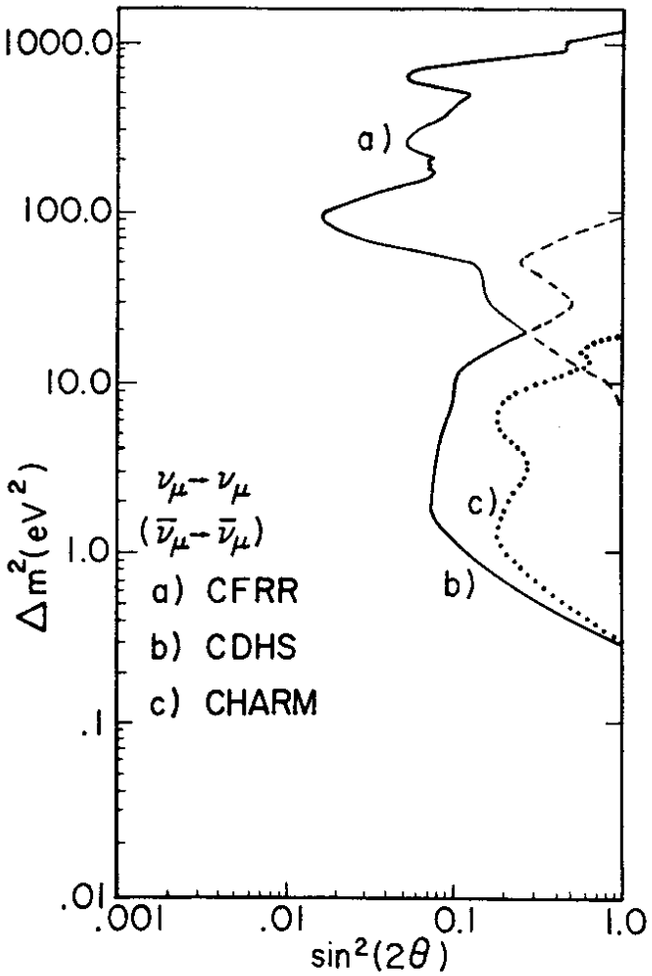

The other inclusive ν oscillation channel which has been studied extensively is $\bar{\nu}_e \to \nu_x$. A group working at the Gosgen reactor[76] has reported results using data taken at 2 locations, as well as an analysis which incorporates a calculation of the ν flux. These limits are shown in Fig. VI. 11. An Annecy-Grenoble collaboration[77] has reported a possible signal in inclusive $\bar{\nu}_e$ oscillations. The regions allowed by their data are shown in Fig. VI. 12. There are disagreements between the Gosgen and Annecy-Grenoble groups regarding the systematic uncertainties in the calculation of the ν flux. Both experiments are continuing to take data and the question of the existence of a signal in this channel may be more clearly answered within several years. Both groups rule out a region in the parameter space where an experiment at the Savannah River reactor indicated a signal.[80]

The current data on the exclusive ν_μ channels may be found in Figs. VI.13. More information is given in the reviews by Baltay[40], Bodek[44], and Shaevitz[43].

Figure VI.11: Shown are the 90 % C.L. limits on inclusive $\bar{\nu}_e$ oscillations obtained by the Caltech-SIN-TUM collaboration working at the Gosgen nuclear reactor.[76] The solid line is calculated using data from two detector locations, as well as a prediction of the neutrino flux. The dashed and dotted lines were calculated using data taken at 2 and 3 different detector locations, respectively (information about the reactor neutrino spectrum was not used).

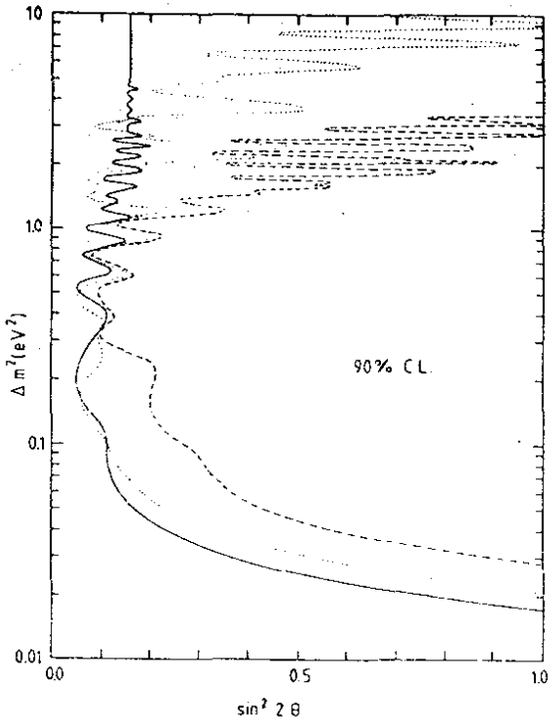

Figure VI.12: Shown are the limits on inclusive $\bar{\nu}_e$ oscillations from the Annecy-Grenoble collaboration working at the Bugey nuclear reactor.[77] The regions to the left of the dashed lines are excluded by an analysis of the relative shapes of the spectra obtained at their two locations. The regions to the right of the solid lines are allowed by an analysis of the relative normalizations at the the locations. The shaded region indicates the region which is not excluded at the 2σ level (95 % C.L.).

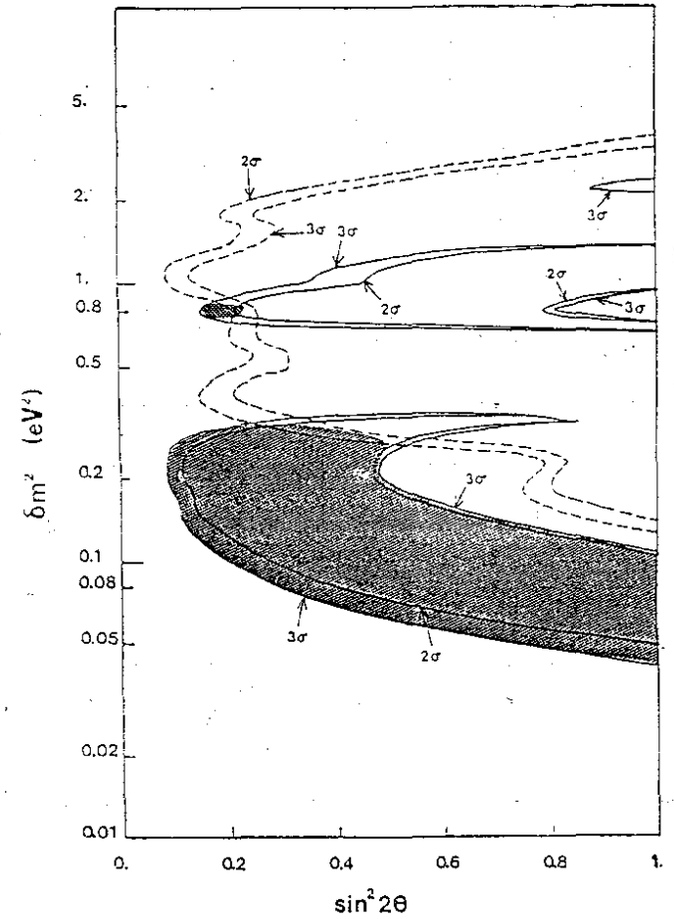

Figure VI.13: Shown are the current limits from exclusive searches for ν_μ oscillations.

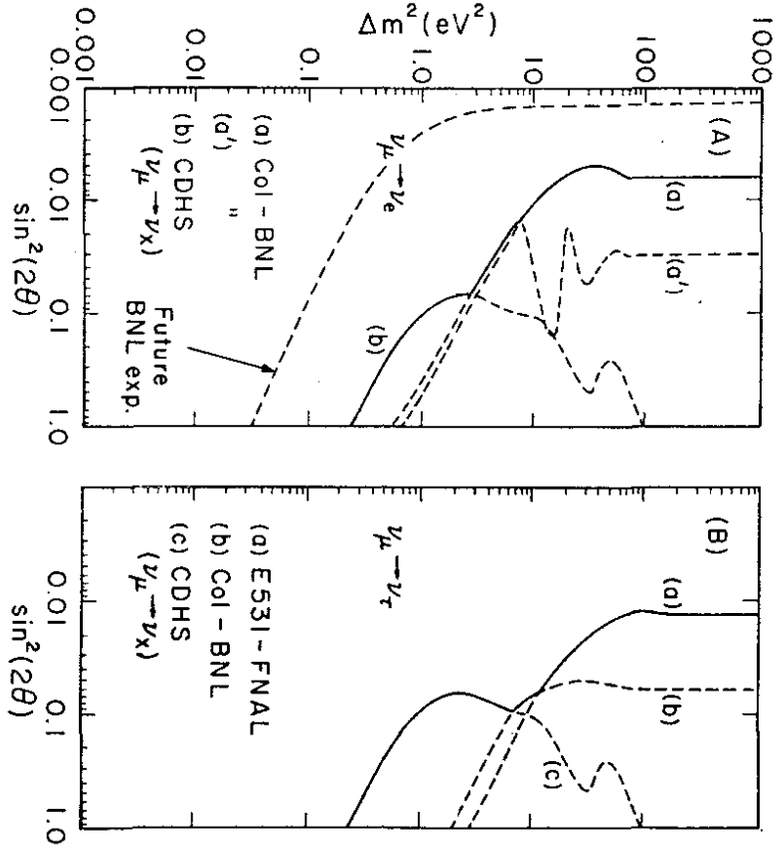

In conclusion, the experimental situation regarding ν masses and oscillations has improved greatly during the past several years. A large region is now excluded in the ν_μ inclusive channel, where no limits existed previously. There is a hint of an oscillation signal in the inclusive $\bar{\nu}_e$ channel, with the hope of an improvement in the data soon.

The sensitivity of direct ν mass measurements has improved, with the ν_μ and ν_τ mass limits being lowered by a factor of 2 and the measurement (soon to be tested independently) of a non-zero $\bar{\nu}_e$ mass. It now seems possible that within two years, a definitive answer may be found to the question of whether neutrinos are massive.

References

1. S. M. Bilenky and B. Pontecorvo, Phys. Rep. 41 (1978) 225.

2. P. H. Frampton and P. Vogel, Phys. Rep. 82 (1982) 339.

3. B. Kayser, Proc. of the Fourth Moriond Workshop on Massive Neutrinos, LaPlagne, France, January 1984.

4. S. P. Rosen, Los Alamos Preprint LA-UR-84-530 (1984).

5. L. Wolfenstein, Carnegie Mellon Preprint CMU-HEP84-18 (1984).

6. R. N. Mohapatra and G. Senjanovic, Phys. Rev. D23 (1981) 165; R. N. Mohapatra and G. Senjanovic, Phys. Rev. Lett. 44 (1980) 912.

7. E. Witten, Phys. Lett. 91B (1980) 81.

8. G. Senjanovic, Proc. of the BNL Neutrino Oscillation Workshop, Brookhaven National Laboratory, January 1981, p. 135.

9. V. A. Lubimov, et.al., Phys. Lett. 94B (1980) 266; V. A. Lubimov, to be published in Proceedings of the XXII International Conference on High Energy Physics, Leipzig, GDR, July 1984.

10. K.-E. Bergqvist, Nucl. Phys. B39 (1972) 317.

11. R. Abela, et.al., SIN Preprint PR-84-09 (July 1984), submitted to Phys. Lett. B.

12. C. Matteuzzi, et.al., Phys. Rev. Lett. 52 (1984) 1869.

13. W. Bacino, et.al., Phys. Rev. Lett. 42 (1979) 749. The new lower limit, which has been reported at conferences, has not yet been published.

14. T. Kirsten, H. Richter, and E. K. Jessberger, Z. Phys. C16 (1983) 189.

15. A. Forster, et.al., Phys. Lett. 138B (1984) 301.

16. M. S. Dixit, et.al., Phys. Rev. D27 (1983) 2216.

17. R. E. Shrock, Phys. Lett. 96B (1980) 159.

18. S. Yasumi, et.al., Phys. Lett. 122B (1983) 461.

19. A. De Rujula and M. Lusignoli, Nucl. Phys. B219 (1983) 277.

20. E. D. Commins and P. H. Bucksbaum, Weak Interactions of Leptons and Quarks (Cambridge University Press, Cambridge, 1983), p. 391.

21. I. G. Kaplan, V. N. Smutny, and G. V. Smelov, Sov. Phys. JETP 57 (1983) 483.

22. M. Shaevitz, Proceedings of the 1983 Symposium on Lepton-Photon Interactions, Cornell, 1983, D.G.Cassel and D. L. Kreinick, eds.

23. H. B. Anderhub, et.al., Phys. Lett. 114B (1982) 76.

24. M. L. Perl, Ann. Rev. Nucl. Part. Sci. 30 (1980) 299.

25. M. Doi, et.al., Phys. Lett. 102B (1981) 323.

26. B. Kayser and A. S. Goldhaber, Phys. Rev. D28 (1983) 2341.

27. S. M. Bilenky, N. P. Nedelcheva, and S. T. Petcov, JINR Preprint E2-84-201, submitted to Nucl. Phys. B.

28. R. Cowsik and J. McClelland, Phys. Rev. Lett. 29 (1972) 669.

29. G. Steigman, Ann. Rev. Nucl. Part. Sci. 29 (1979) 313.

10. D. N. Schramm and G. Steigman, Ap. J. 243 (1981) 1.

11. K. Freese and D. N. Schramm, Nucl. Phys. B233 (1984) 167.

12. V. C. Rubin, Science 220 (1983) 1339.

13. S. Weinberg, Gravitation and Cosmology, (John Wiley and Sons, New York, 1972) p. 441.

14. G. de Vaucouleurs and G. Bollinger, Ap.J. 233 (1979) 433.

15. D. N. Schramm and R. V. Wagoner, Ann. Rev. Nucl. Sci. 27 (1977) 37.

6. B. Kayser, Phys. Rev. D24 (1981) 110.

7. M. Kobayashi and T. Maskawa, Prog. Theor. Phys. 49 (1973) 652.

8. V. Barger, et. al., Phys. Rev. D22 (1980) 1636.

9. I. I. Bigi, Z. Phys. C12 (1982) 235.

0. C. Baltay, Proceedings of the 1981 International Conference on Neutrino Physics and Astrophysics, R. J. Cence, E. Ma, A. Roberts, eds. (Honolulu, Hawaii, 1981), p. 295.

1. R. Blair, et. al., Phys. Rev. Lett. 51 (1983) 3431.

2. JADE Collaboration, W. Bartel, et.al., Phys. Lett. 123B (1983) 353.

3. M. Shaevitz, Proceedings of the 1983 Symposium on Lepton-Photon Interactions, Cornell, 1983, D.G.Cassel and D. L. Kreinick, eds.

4. A. Bodek, Rochester Preprint UR-787, to be published in the Proc. of ICOBAN 84, Park City, Utah, January 1984.

5. J. R. Lee, Ph.D. thesis (California Institute of Technology), 1981.

6. R. Blair, Ph.D. thesis (California Institute of Technology), 1982.

7. D. MacFarlane, et.al., Fermilab-Pub-83/108-EXP (Dec. 1983), to be published in Zeit. Phys. C.

8. D. B. MacFarlane, Ph.D. thesis (California Institute of

Technology), Nevis Report No. 1297 (Nov. 1983).

49. M. V. Purohit, Ph.D. thesis (California Institute of Technology), Nevis Report No. 1298 (Nov. 1983).

50. R. E. Blair, et.al., Fermilab-Conf-83/76 (1983), submitted to Proc. of Europhysics Study on Electroweak Effects at High Energies, Italy, February 1983.

51. B. Barish, et.al., IEEE Transactions on Nuclear Science, Vol. NS-25 (1978) p.532.

52. RCA Corp., RCA Bldg., 30 Rockefeller Plaza, New York, NY.

53. Marvel Guard EC1A, Delta Packaging, 789 Golf Lane, Bensonville, IL 60106.

54. Polycast Technology Corp., 69 Southfield Ave., Stamford, Conn., 06902. This scintillator, developed by the CCFR collaboration, has subsequently been used by the Fermilab-MIT-Michigan State neutrino experiment; cf. M. A. Abolins, Proceedings of the 1982 DPF Summer Study on Elementary Particle Physics and Future Facilities, Snowmass, Colorado, R. Donaldson, R. Gustafson, and F. Paige, eds., 1982.

55. EG&G Model FX-279, ORTEC Corp., 100 Midland RD. Oak Ridge, TN.

56. P. G. Reutens, Proceedings of the Calorimeter Calibration Workshop, Fermilab, Hans Jostlein, ed., p. 172.

57. R. F. Holsinger, CERN Computer Centre Program Library T604.

58. D. A. Edwards and F. J. Sciulli, Fermilab TM-660 (May 1976); D. A. Edwards, et.al., Fermilab TM-661 (May 1976).

59. P. Auchincloss, et.al., Fermilab FN-382 (March 1983), submitted to Nucl. Instr. Meth.

60. C. Haber, Ph.D. thesis (Columbia University), Dec. 1984.

61. D. C. Carey, et.al., Decay TURTLE, SLAC-246 (March 1982).

62. H. W. Atherton, et.al., CERN 80-07 (1980); A. J. Malensek, Fermilab FN-341 (October 1981).

63. E. Fermi, Nuclear Physics (University of Chicago Press, Chicago, IL, 1950).

64. F. James and M. Roos, Computer Physics Commun. 10 (1975) 343.

65. M. H. Shaevitz, private communication.

66. A. J. Buras and K. I. F. Gaemers, Nucl. Phys. B132 (1978) 249.

67. W. T. Eadie, et.al., Statistical Methods in Experimental Physics (North-Holland, New York, 1971), p. 230.

68. A. G. Frodesen, et. al., Probability and Statistics in Particle Physics (Universitetsforlaget, Oslo, Norway, 1979), p. 388.

69. J. Orear, Cornell preprint CLNS 82/511 (July 1982).

70. W. T. Eadie, op.cit., p. 232.

71. I. E. Stockdale, et.al., Phys. Rev. Lett. 52 (1984) 1384.

72. I. E. Stockdale, et.al., University of Rochester pre-print no. UR-894, October 1984 (to be published in Z. Phys. C).

73. C. Haber, et.al., Nevis Report No. 1312, submitted to Proceedings of the XIX Recontre de Moriond, January 1984.

74. A. G. Frodesen, op.cit., p. 415.

75. A. G. Frodesen, op.cit., p. 416.

76. K. Gabathuler, et.al., Phys. Lett. 138B (1984) 449; J. L. Villeumier, et.al., Phys. Lett. 114B (1982) 298; H. Kwon, et.al., Phys. Rev. D24 (1981) 1097.

77. J. F. Cavaignac, et.al., LAPP-EXP-84-03 (May 1984), submitted to Phys. Lett.

78. F. Dydak, et.al., Phys. Lett. 134B (1984) 281.

79. F. Bergsma, et.al., Phys. Lett. 142B (1984) 103.

80. F. Reines, et.al., Phys. Lett. 45 (1981) 1307.

Appendix A

Muon Momentum Reconstruction Formalae

Section I: Initial Guess for p_μ

The initial value of p_μ (cf. Ch. IV, p. 117) in the Wonder Bldg. was calculated under the assumption of no dE/dx energy loss and no multiple scattering in the toroidal magnet. The magnetic field (B_x and B_y) was calculated midway between the extrapolation of the front and back tracks at the centre of the magnet and assumed to be constant throughout.

The exact expression which was used is:

$$p_\mu^0 = \sqrt{B_x^2 + B_y^2}\ \frac{z_{back}}{F_0 - F_1 + S}$$

where, $F_0 = \left(\frac{dr}{dz}\right)_0 / SF_0$

$$\left(\frac{dr}{dz}\right)_0 = \frac{x_0\ Slope_x + y_0\ Slope_y}{r_0}$$

$$SF_0 = \sqrt{1 + (Slope_x)^2 + (Slope_y)^2}$$

$$x_0 = x_{front} + \frac{z_{back}}{2}\ Slope_x$$

$$y_0 = y_{front} + \frac{z_{back}}{2}\ Slope_y$$

$$r_0^2 = x_0^2 + y_0^2$$

$$F_1 = \left(\frac{dr}{dz}\right)_1 / SF_1$$

$$\left(\frac{dr}{dz}\right)_1 = \frac{x_1\ Slope_x + y_1\ Slope_y}{r_1}$$

$$SF_1 = \sqrt{1 + (Slope_x)^2 + (Slope_y)^2}$$

$$x_1 = x_{front} + \frac{z_{back}}{2}\ Slope_x$$

$$y_1 = y_{front} + \frac{z_{back}}{2}\ Slope_y$$

$$r_1^2 = x_1^2 + y_1^2$$

$$S = \frac{1}{2}\ (\phi_1 - \phi_0)\ (G_1 - G_0)$$

$$\phi_0 = \tan^{-1}\left(\frac{y_0}{x_0}\right)$$

$$\phi_1 = \tan^{-1}\left(\frac{y_1}{x_1}\right)$$

$$G_0 = \frac{H_0}{SF_0}$$

$$G_1 = \frac{H_1}{SF_1}$$

$$H_0 = \frac{x_0\ Slope_x - y_0\ Slope_y}{r_0}$$

$$H_1 = \frac{x_1\ Slope_x - y_1\ Slope_y}{r_1}$$

Section II: Error Matrix

As noted in Chapter IV, the χ^2 function for the momentum fit is given by:

$$\chi^2 = \Delta^T \varepsilon^{-1} \Delta \qquad (1)$$

where,

$$\Delta = \begin{pmatrix} \Delta x \\ \Delta s_x \\ \Delta y \\ \Delta s_y \end{pmatrix} \qquad (2)$$

The error matrix, ε, is a 4 x 4 block diagonal matrix of the form:

$$\varepsilon = \begin{pmatrix} \varepsilon_x & 0 \\ 0 & \varepsilon_y \end{pmatrix} \qquad (3)$$

where ε_x and ε_y are 2 x 2 matrices containing the errors for

the x- and y-views, respectively. The error matrix is in block diagonal form because the two views are uncorrelated.

The inverse of the error matrix is also block diagonal:

$$\varepsilon^{-1} = \begin{pmatrix} \varepsilon_x^{-1} & 0 \\ 0 & \varepsilon_y^{-1} \end{pmatrix} \qquad (4)$$

The error matrices, ε_x and ε_y, are calculated from the error matrices of the least squares fits of the tracks and from the multiple scattering errors.

The inverse of the error matrix for the track in the front x-view is given by:

$$\varepsilon_{f,x}^{-1} = \begin{pmatrix} \sum_i Wt_i & \sum_i Wt_i \, z_{ch}^i \\ \sum_i Wt_i \, z_{ch}^i & \sum_i Wt_i \, (z_{ch}^i)^2 \end{pmatrix}$$

where the weight for each spark, Wt_i, is the error on the spark location (as determined from the measurement error and the multiple scattering) divided by the number of sparks on the wand. The matrices $\varepsilon_{f,y}$, $\varepsilon_{b,x}$, and $\varepsilon_{b,y}$ are given by similar expressions.

The diagonal error in θ due to multiple scattering is given by:[63]

$$\langle\theta^2\rangle \simeq \frac{.015}{p_\mu^2} \frac{L_{Fe}}{L_{rad}} \qquad (7a)$$

where θ is in radians, p_μ is in GeV/c, L_{Fe} is the distance in steel, and L_{rad} is the radiation length in steel (1.76 cm). The other errors are related to $\langle\theta^2\rangle$ by:

$$\langle\theta\phi\rangle = \frac{L_{Fe}}{2} \langle\theta^2\rangle$$

$$\langle\phi^2\rangle = \frac{L_{Fe}^2}{3} \langle\theta^2\rangle$$

Thus, the form of the x-error matrix is:

$$\varepsilon_x = \begin{pmatrix} \varepsilon_{11,f,x} + \varepsilon_{11,b,x} + \langle\phi^2\rangle & \varepsilon_{12,f,x} + \varepsilon_{12,b,x} + \langle\phi\theta\rangle \\ \varepsilon_{21,f,x} + \varepsilon_{21,b,x} + \langle\phi\theta\rangle & \varepsilon_{22,f,x} + \varepsilon_{22,b,x} + \langle\theta^2\rangle \end{pmatrix}$$

The y-view error matrix, ε_y, has a similar form.

Appendix B

Members of the CCFR Collaboration

A. Bodek, F. Borcherding[2], N. Giokaris[2],
K. Lang, I. E. Stockdale
Department of Physics and Astronomy
University of Rochester, Rochester, New York 14627

and

D. Garfinkle, F. S. Merritt, M. Oreglia, P. Reutens
Enrico Fermi Institute, University of Chicago,
Chicago, Illinois 60637

and

P. S. Auchincloss, R. Blair, C. Haber, M. Ruiz[3]
F. Sciulli, M. H. Shaevitz, W. H. Smith, R. Zhu[4]
Physics Department
Columbia University, New York, New York 10027

and

R. Coleman, H. E. Fisk, B. Jin[4], D. Levinthal[5]
W. Marsh, P. A. Rapidis, H. B. White, D. Yovanovitch
Fermi National Accelerator Laboratory,
Batavia, Illinois 60510

(1) present address: Fermi National Accelerator Laboratory,
Batavia, IL 60510, USA
(2) present address: Department of Physics,
University of Notre Dame
Notre Dame, IN 46556, USA
(3) present address: Department of Physics,
University of Florida,
Gainesville, FL 32611, USA
(4) present address: Institute for High Energy Physics,
Beijing, Peoples' Republic of China
(5) present address: Department of Physics,
Florida State University,
Tallahassee, FL 32306, USA